

**RAMAN AND EXAFS STUDIES OF LOW-NICKEL SUBSTITUTION  
IN  $\text{YBa}_2(\text{Cu}_{1-x}\text{Ni}_x)_3\text{O}_{7-\delta}$  SUPERCONDUCTORS**

**An Abstract of a Thesis  
Presented to the Faculty of the  
Department of Physics  
Western Illinois University**

**In Partial Fulfillment  
of the Requirements for the Degree  
Master of Science**

**by  
No Soung Myoung  
May 2002**

## ABSTRACT

A comparative study of the results of Raman spectroscopy and Extended X-ray Absorption Fine Structure (EXAFS) spectroscopy, along with in-field critical current density determinations, was performed to ascertain the structural changes associated with low levels of nickel doping in polycrystalline  $\text{YBa}_2\text{Cu}_3\text{O}_{7-\delta}$  (YBCO). Four samples were doped with molar-proportional percentages (0.32%, 0.64%, 0.96%, and 3.3%) of Ni (nickel) replacing the Cu (copper) in the starting materials, along with a control sample of pure YBCO. The Raman spectra were collected over multiple averaged scans with a GaAs PMT and a Triax 550 spectrometer equipped with a holographic Super-Notch Plus filter and were excited with 150 mW of 514.5 nm argon-ion laser radiation at the sample surface. The Raman studies indicated the increasing presence of NiO impurity in the sample as the doping level increased, but also clearly indicated that some of the Ni substitutes in the Cu sites of the Cu-O chains in the material, breaking their symmetry and allowing them to become Raman-active. This finding is especially significant in view of the fact that earlier studies in the literature have been inconclusive as to the exact site of the substituting Ni atoms. This effect is largest in the sample with the lowest dopant level (0.32%), which also demonstrated the optimal enhancement of the in-field transport critical current density for the lower field ranges. The EXAFS spectra were collected using the Advanced Photon Source (APS) at Argonne National laboratory, and exhibited little, if any detectable changes in the local atomic structure across the three lowest doped samples, but did exhibit a peak of increasing intensity with higher doping levels that indicated the increasing presence of NiO impurities, and delineating the reason for the drastic reduction in critical current densities for the larger nickel doping levels.

## APPROVAL PAGE

This thesis by No Soung Myoung is accepted in its present form by the Department of Physics of Western Illinois University as satisfying the thesis requirement for the degree Master of Science.

---

Chairperson, Examining Committee

---

Member, Examining Committee

---

Member, Examining Committee

---

Date

**RAMAN AND EXAFS STUDIES OF LOW-NICKEL SUBSTITUTION  
IN  $\text{YBa}_2(\text{Cu}_{1-x}\text{Ni}_x)_3\text{O}_{7-\delta}$  SUPERCONDUCTORS**

**A Thesis**

**Presented to the**

**Department of Physics**

**Western Illinois University**

**In Partial Fulfillment**

**of the Requirements for the Degree**

**Master of Science**

**by**

**No Soung Myoung**

**May 2002**

## ACKNOWLEDGMENTS

My first thanks go to my supervisor and thesis advisor, Dr. Mark S. Boley. He gave me invaluable and specific guidance on the research of superconductivity through a great variety of conversation in his office as well as on the way to the main library. His extraordinary support for the research and the advice for me stimulated me to make greater effort.

I also want to thank Mr. Doug Franklin for all his kindness. I really appreciated all my thesis corrections and his advice as a thesis committee member. I would like to thank Dr. Harold B. Hart as a graduate thesis committee member, who was the first professor I met in Macomb. It was gracious of you to accept me with all my apprehension. I want to say “ Thank You” to Mr. Michael C. Baxa who was my assistant and counselor for all experiments in the WIU physics department. I will remember his help for my thesis to the last.

I would also like to thank the undergraduate students, J.C. Gumbart, Jason Wilson, Tom Boyle, Jason Orris, and Matthew Tillman, as well as Naveen Jha from Nepal and Laurie Pichla who were graduate students. While I am not listing each of you individually, I hope you will recognize your contributions for my work in the United States.

And, finally, I would like to thank my parents, who always emphasize modesty, and to my younger brother, Nho Sik Myoung.

# TABLE OF CONTENTS

	Page
ACKNOWLEDGEMENTS .....	ii
TABLE OF CONTENTS .....	iii
LIST OF FIGURES .....	v
LIST OF TABLES .....	vii
CHAPTER 1. INTRODUCTION	
1-1.    MOTIVATION .....	1
1-2.    HISTORY OF CONVENTIONAL AND HIGH- $T_c$ SUPERCONDUCTIVITY	
1-2-1. HISTORY OF CONVENTIONAL SUPERCONDUCTIVITY .....	2
1-2-2. BCS THEORY .....	3
1-2-3. LONDON EQUATION .....	5
CHAPTER 2. THEORY AND PRESENT WORK IN HIGH- $T_c$ SUPERCONDUCTOR	
2-1. THEORY OF RAMAN SPECTROSCOPY .....	6
2-2. MEISSNER EFFECT .....	10
2-3. CRITICAL TEMPERATURE ( $T_c$ )	
AND CRITICAL CURRENT DENSITY ( $J_c$ ) .....	14
2-4. THEORY OF EXTENDED X-RAY ABSORPTION FINE STRUCTURE (EXAFS) .....	15
CHAPTER 3. SAMPLE PREPARATION AND EXPERIMENTS	
3-1. SAMPLE PREPARATION .....	22
3-2. THE RAMAN SCATTERING MEASUREMENT .....	24
3-3. THE CRITICAL TEMPERATURE ( $T_c$ )	

AND CRITICAL CURRENT DENSITY ( $J_c$ ) MEASUREMENT .....	30
3-4. EXAFS MEASUREMENT .....	36
CHAPTER 4. DISCUSSION OF RESULTS	
4-1. RAMAN SCATTERING ANALYSIS .....	43
4-2. DISCUSSION OF THE CRITICAL TEMPERATURE ( $T_c$ )	
DEPENDENCE ON NICKEL DOPING.....	56
4-3. DISCUSSION OF THE CRITICAL CURRENT DENSITY ( $J_c$ )	
DEPENDENCE ON NICKEL DOPING .....	65
4-4. DISCUSSION OF EXTENDED X-RAY ABSORPTION	
FINE STRUCTURE (EXAFS) .....	75
CHAPTER 5. CONCLUSIONS .....	80
REFERENCES .....	82
APPENDIX A .....	86

## LIST OF FIGURES

Figure	Page
<b>Chapter 2. Theory and Present Work in High-<math>T_c</math> Superconductor</b>	
2-1. Energy level diagram for Raman scattering is shown below.	7
2-2. The Meissner effects are shown with (a) changing temperature and (b) changing field.	11
2-3. Simplified magnetic phase diagrams showing Type-I and Type-II superconductors are depicted below (Note that $H_c$ is zero when the temperature $T$ equals the critical temperature $T_c$ ).	12
2-4. This is the temperature dependence of the critical current density $J_c(T)$ in accordance with Eq. 2-9.	16
2-5. This is the simple Stern model of EXAFS with outgoing and backscattered waves.	19
<b>Chapter 3. Sample Preparation and Experiments</b>	
3-1. This shows a schematic of the Raman scattering experimental setup in the WIU physics department optical spectroscopy research laboratory.	26
3-2. This is a diagram of the spectral data collection program written in our laboratory operating in the LabView environment.	28
3-3. This is a diagram of the slit controller in LabView.	30
3-4. This is a diagram of the temperature monitoring program in LabView.	31
3-5. This is a schematic of the four point probe to measure the critical temperature and the in-field critical current.	33
3-6. This is a schematic of the liquid nitrogen cryostat used for critical state measurements in the WIU physics department superconductivity research laboratory.	35
3-7. This is the schematic of the EXAFS equipment setup.	40
<b>Chapter 4. Discussion of Results</b>	
4-1. Primitive unit cell of stoichiometric $YBa_2Cu_3O_{7-\delta}$ . The stretching motion is indicated by the arrows on the O(4) atoms. A segment of the linear chain used in theoretical calculations is shown at the left.	44
4-2. This is the Raman spectrum for undoped $YBa_2Cu_3O_{7-\delta}$ ( $\delta = 0$ ).	45
4-3. This is the Raman spectrum for $YBa_2(Cu_{1-x}Ni_x)_3O_{7-\delta}$ ( $x = 0.0032$ , $\delta = 0$ ).	46
4-4. This is the Raman spectrum for $YBa_2(Cu_{1-x}Ni_x)_3O_{7-\delta}$ ( $x = 0.0064$ , $\delta = 0$ ).	47
4-5. This is the Raman spectrum for $YBa_2(Cu_{1-x}Ni_x)_3O_{7-\delta}$ ( $x = 0.0096$ , $\delta = 0$ ).	48
4-6. This is the Raman spectrum for $YBa_2(Cu_{1-x}Ni_x)_3O_{7-\delta}$ ( $x = 0.033$ , $\delta = 0$ ).	49
4-7. These are the Raman spectra for $YBa_2(Cu_{1-x}Ni_x)_3O_{7-\delta}$ at different concentrations $x$ (at. %).	54
4-8. This is the temperature dependence of resistivity for $YBa_2(Cu_{1-x}Ni_x)_3O_{7-\delta}$ ( $\delta = 0$ ), with all doping levels tested.	57



4-9. This shows the superconducting transition temperature, $T_c$ , as a function of the Ni concentration in Y-B-Cu-O( $Ni_x$ ) using the corrected Ni concentrations.	58
4-10. This is the resistivity versus temperature curve for undoped $YBa_2Cu_3O_{7-\delta}$ ( $\delta = 0$ ).	59
4-11. This is the resistivity versus temperature curve for $YBa_2(Cu_{1-x}Ni_x)_3O_{7-\delta}$ ( $x = 0.0032$ , $\delta=0$ ).	61
4-12. This is the resistivity versus temperature curve for $YBa_2(Cu_{1-x}Ni_x)_3O_{7-\delta}$ ( $x = 0.0064$ , $\delta=0$ ).	62
4-13. This is the resistivity versus temperature curve for $YBa_2(Cu_{1-x}Ni_x)_3O_{7-\delta}$ ( $x = 0.0096$ , $\delta=0$ ).	63
4-14. This is the resistivity versus temperature curve for $YBa_2(Cu_{1-x}Ni_x)_3O_{7-\delta}$ ( $x = 0.033$ , $\delta=0$ ).	64
4-15. This is the critical current density versus magnetic field for $YBa_2(Cu_{1-x}Ni_x)_3O_{7-\delta}$ ( $\delta=0$ ) at 77K for all doping levels tested and the control sample.	66
4-16. This is the critical current density versus magnetic field for $YBa_2(Cu_{1-x}Ni_x)_3O_{7-\delta}$ ( $\delta=0$ ) at 60K for all doping levels tested and the control sample.	67
4-17. This is the critical current density versus magnetic field for $YBa_2Cu_3O_{7-\delta}$ ( $\delta=0$ ).	68
4-18. This is the critical current density versus magnetic field for $YBa_2(Cu_{1-x}Ni_x)_3O_{7-\delta}$ ( $x = 0.0032$ , $\delta=0$ ).	69
4-19. This is the critical current density versus magnetic field for $YBa_2(Cu_{1-x}Ni_x)_3O_{7-\delta}$ ( $x = 0.0064$ , $\delta=0$ ).	70
4-20. This is the critical current density versus magnetic field for $YBa_2(Cu_{1-x}Ni_x)_3O_{7-\delta}$ ( $x = 0.0096$ , $\delta=0$ ).	71
4-21. This depicts the variation of magnetic field dependence of $J_c$ due to concentration $x$ .	74
4-22. This is the Fourier transform of a reference NiO Sample from a standard EXAFS experiment.	76
4-23. These are the Fourier Transforms for three low Ni-doped samples measured by EXAFS.	77

## LIST OF TABLES

Table	Page
<b>Chapter 3. Sample Preparation and Experiments</b>	
1. The stoichiometric amounts of each component are measured by an electric scale as below.	23
2. Specifications of the TRIAX –550 imaging spectrometer are below.	27
3. These are the fractional densities of the total density and absorption coefficients.	37
<b>Chapter 4. Discussion of Results</b>	
4. These are the experimental and calculated frequencies of Raman-active modes for YBCO below $T_c$ .	52
5. This shows critical current densities with their corresponding measurement temperatures and their values of the externally applied magnetic fields at the different levels of nickel doping used in our samples. [Here, $\delta = 0$ for $YBa_2(Cu_{1-x}Ni_x)_3O_{7-\delta}$ ]	73
6. These are the dominant peak distances from the Fourier transforms of the Ni-doped $YBa_2Cu_3O_{7-\delta}$ samples and the NiO reference sample.	78

# 1. Introduction

## 1-1. Motivation

Since the discovery of superconductivity above liquid nitrogen temperatures,  $\text{YBa}_2\text{Cu}_3\text{O}_{7-\delta}$  has been one of the most thoroughly investigated systems.<sup>1</sup> The fact that impurity phonons can be easily observed in the Raman spectra of materials serves as a natural motivation to study the optical properties of nominally pure materials in comparison to materials into which impurities have been selectively doped. In addition, it is primarily because of some of the magnetic effects occurring below  $T_c$  that many optical studies of impurities in  $\text{YBa}_2\text{Cu}_3\text{O}_{7-\delta}$  have focused on nickel doping.

One of the primary concerns for potential applications of high- $T_c$  superconductors is the enhancement of the relatively low critical transport current density ( $J_c$ ). Several experiments at WIU have focused on studying the effects of low-nickel doping on the  $J_c$  of  $\text{YBa}_2\text{Cu}_3\text{O}_{7-\delta}$  polycrystalline superconductors. Several earlier studies conducted elsewhere have predicted a wide range of values of the suppression of  $T_c$  with  $x$ , and these have also likely contributed to the uncertainty of the substitution site for Ni in Y-123. We have recently carried out Raman scattering measurements in our spectroscopy laboratory on several sets of low-doped samples along with a control sample, all of which were produced in our sample preparation laboratory. Furthermore, Extended X-ray Absorption Fine Structure (EXAFS) spectroscopy measurements have been conducted on the Ni-doped Y-123 samples by a WIU undergraduate student in our research group, Michael Baxa, during a summer (2000) internship at the advanced photon source at Argonne National Laboratory, near Chicago, Illinois.

In addition, we have analyzed the Raman-active electronic spectra and compared them with the previous literature to obtain further knowledge about the physical properties and how the phonons are affected by the crystalline and chemical structure, and the temperature. We also hope to learn how much of the Ni actually incorporates into the structure and to further pin-point its location, or to identify any NiO impurities and their location.

## **1-2. History of Conventional and High- $T_c$ Superconductivity**

### **1-2-1. History of Conventional Superconductivity**

Superconductivity was first discovered in 1911 by the Dutch physicist, Heike Kammerlingh Onnes, who initiated the field of low-temperature physics by liquefying helium below 4 K in his laboratory. Onnes investigated the electrical properties of metals at extremely low temperatures. It was well-known that the resistance of metals dropped when cooled below room temperature, but it was not known what limiting value the resistance would approach if the temperature were reduced to near 0 K. Some scientists, such as William Kelvin, had previously believed that electrons flowing through a conductor would come to a complete halt as the temperature approached absolute zero. However, Onnes found that below 4.5 K, the dc resistance of mercury dropped to zero.<sup>2</sup> In 1913, lead was found to be superconducting at 7.2 K. In 1933, Meissner and Ochsenfeld found that the magnetic field is completely expelled from the interior of the superconductor, in contradiction with the classical expectation.<sup>3</sup> But other scientists, like Onnes, now felt that a cold wire's resistance would dissipate. The theory of Landau and Ginzburg in 1950 developed the theoretical properties of superconductors. It described

superconductivity in terms of an ordering parameter and a highly ordered phase transition, and provided a derivation for the London equations as will be shown in one of the following sections (1-2-3). The transition temperature was observed to decrease as the average isotopic mass increases, as was predicted theoretically by Herbert Frohlich,<sup>4</sup> and then was later discovered experimentally by E. Maxwell.<sup>5</sup>

Three American physicists, John Bardeen, Leon Cooper, and Robert Schrieffer, won the Nobel prize in physics in 1972 for the development of a model that electrons in a superconductor condense into a quantum ground state and travel together collectively. This theory of superconductivity is now well-known as the BCS theory. In 1986, Georg Bednorz and Alex Müller were experimenting with a particular class of metal oxide ceramics called perovskites, such as  $\text{YBa}_2\text{Cu}_3\text{O}_{7-\delta}$ . They found indications of superconductivity at 35 K, a startling 12 K above the previously established record for a superconductor. In 1987, a perovskite ceramic material was found to superconduct at 90 K.<sup>6</sup> These materials are referred to as high temperature superconductors because they enter the superconducting state at much higher temperatures than the conventional superconductors discovered prior to 1986.

### **1-2-2. BCS Theory**

In 1957, Bardeen, Cooper, and Schrieffer explained the occurrence of superconductivity and predicted its properties in elemental superconductors. Two electrons near the Fermi level could couple to form an effective new particle, even under a very weak attractive force. This attraction leads to the formation of the Cooper pair.<sup>7</sup> BCS theory predicts the instability of the normal state of an otherwise free electron gas.

BCS theory also predicts that the electron gas is unstable to the formation of a coherent many-body ground state in the presence of an attractive interaction between electrons. This does not provide a description of the superconducting state, however, or even demonstrate that superconductivity exists at all. The interaction of two electrons due to lattice dynamics occurs by virtue of the Coulomb attraction to the ions in the lattice and is mediated via phonons.

A second electron can experience the disturbance created by a first and then reacts in a way to reduce the potential energy, thus causing an effective attraction which overcomes the Coulomb repulsion between the two electrons. As a result of the Pauli exclusion principle, the electrons cannot all inhabit the states of lowest kinetic energy because they are already occupied by other electrons. In conventional superconductors, the mechanism for pair formation is thus the electron-phonon interaction, but other mechanisms are also possible, for instance, polarons or excitons.<sup>8</sup>

In addition, the BCS theory predicts that, first of all, the energy gap  $E_g$  between the BCS ground state and the first excited state is proportional to the transition temperature. Second, it predicts that the energy gap  $E_g$  is the minimum energy required to create a single electron excitation from the superconducting ground state. And third, the London equations arise as a natural consequence of BCS theory, which allows for a state of perfect diamagnetism to exist below  $T_c$  with  $\chi = -\frac{1}{4\pi}$  (CGS), or  $\chi = -1$  (SI), where  $\chi$  is the magnetic susceptibility that the Meissner effect implies.

### 1-2-3. London Equation

The Meissner effect also implies that superconductivity will be destroyed by a critical magnetic field  $H_c$ , which is related thermodynamically to the free-energy difference between the normal and the superconducting states in the zero-field state. F. London and H. London, who proposed two equations to govern the microscopic electric and magnetic fields, described the basic electrodynamic properties of superconductivity in 1935. We can write the London equations (1-1) and (1-2) as

$$\vec{E} = \mu_0 \lambda_L^2 \frac{d\vec{J}}{dt} \quad (1-1)$$

$$\vec{B} = -\mu_0 \lambda_L^2 \vec{\nabla} \times \vec{J} \quad (1-2)$$

where  $\lambda_L \left( = \sqrt{\frac{m^* c^2}{4\pi n_s q^2}} \right)$  is the London penetration depth,  $n_s$  is the density of superconducting electrons which would have an upper bound of the total density of conduction electrons, and  $m^*$  is the effective mass of the electron. Since the superconducting transition is a continuous transition, the density of superconducting electrons will be directly related to the order parameter for the superconductor, and hence the London penetration depth will be temperature dependent.<sup>9</sup>

These two equations give a current density for the induced supercurrents which decreases exponentially with the distance into the bulk of the superconducting sample. Hence, the induced current density is mostly restricted to the surface of the sample.

## 2. Theory and Present Work in High- $T_c$ Superconductors

### 2-1. Theory of Raman Spectroscopy

The Indian physicist, C.V. Raman, discovered the Raman effect, which can yield important information about molecular quantum states and material phonon modes, in 1928. This is the scattering of light by molecules with a resulting frequency change, that is, the visible wavelength of a small fraction of the radiation scattered by certain molecules differs from that of the incident light. If the incident radiation is fairly intense and is monochromatic light of ultra-violet, visible, or infrared frequency  $\nu$ , it is found that the scattered light contains not only radiation of frequency  $\nu$  (Rayleigh scattering), but also weaker radiation of frequency  $\nu \pm \nu'$  (Raman scattering). The frequency difference  $\nu'$  between the incident and the scattered light in the Raman effect, as shown in Fig 2-1, is characteristic of vibrational transitions in the scattering molecule, or of the phonon mode energies associated with a particular material's structure.<sup>10</sup>

The energy difference between the initial and final vibrational levels, or the Raman shift in wave numbers ( $\text{cm}^{-1}$ ), is calculated through Eq. 2-1,

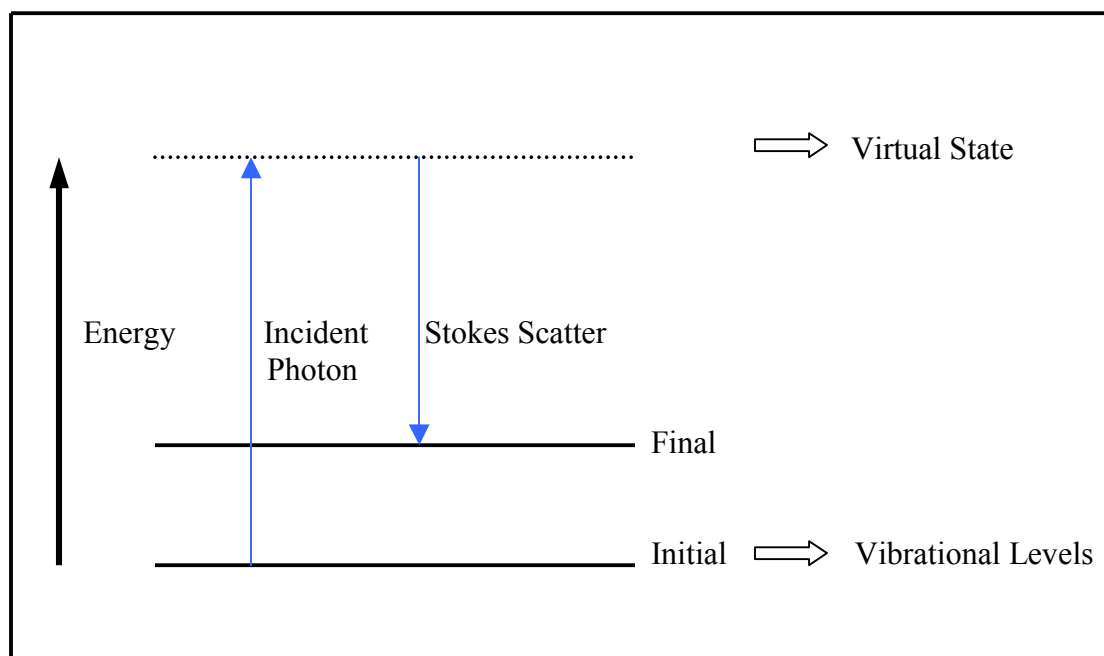
$$\nu = \frac{1}{\lambda_i} - \frac{1}{\lambda_s} \quad (2 - 1)$$

where  $\lambda_i$  is the incident photon wavelength of 514.5 nm in all cases, and  $\lambda_s$  is the Raman scattered photon wavelength. The vibrational energy is ultimately dissipated as heat. Because of the low intensity of Raman scattering, the heat dissipation does not cause a measurable temperature rise in most samples.

The important features of the Raman scattering intensity can be explained by the



**FIGURE 2-1.** Energy level diagram for Raman scattering is shown below.



classical electromagnetic field associated with the incident wave in Raman spectroscopy. An electric dipole moment,  $\mathbf{P}$ , is induced within a molecule when an electromagnetic wave having an electric field  $\mathbf{E}$  is impinging upon the molecule. This induced dipole moment  $\mathbf{P}$  is proportional to the field as shown in Eq. 2-2,

$$\mathbf{P} = \alpha \mathbf{E} \quad (2 - 2)$$

where  $\alpha$  is the polarizability of the molecule.<sup>11</sup> The induced dipole scatters light at the optical frequency of the incident light wave. Then, Raman scattering occurs because a molecular vibration could change the polarizability. In general, the molecular polarizability will be a function of the nuclear coordinates of the molecule. Hence, the change in the polarizability,  $\alpha'$ , is written by the polarizability derivative,

$$\alpha' = \frac{\partial \alpha}{\partial Q} \quad (2 - 3)$$

where  $Q$  is the normal coordinate of the vibration.

This equation implies that the relationship between the  $\mathbf{P}$  and the  $\mathbf{E}$  vectors can be placed into the matrix form,

$$\begin{pmatrix} P_x \\ P_y \\ P_z \end{pmatrix} = \begin{pmatrix} \alpha_{xx} & \alpha_{xy} & \alpha_{xz} \\ \alpha_{yx} & \alpha_{yy} & \alpha_{yz} \\ \alpha_{zx} & \alpha_{zy} & \alpha_{zz} \end{pmatrix} \begin{pmatrix} E_x \\ E_y \\ E_z \end{pmatrix} \quad (2 - 4)$$

This symmetric matrix represents  $\alpha_{xy} = \alpha_{yx}$ ,  $\alpha_{xz} = \alpha_{zx}$ , and  $\alpha_{yz} = \alpha_{zy}$ . The directional relationship between  $\mathbf{P}$  and  $\mathbf{E}$  is determined by non-zero polarizability components. From the point of view of classical electromagnetism, the electromagnetic field can be expressed in terms of the linear induced electric dipole.

$$\bar{P} = \bar{P}(\nu_0) + \bar{P}(\nu_0 - \nu_k) + \bar{P}(\nu_0 + \nu_k) \quad (2-5)$$

These three frequency components are present in this molecular dipole, and give rise to radiation from the dipole at the excitation frequency  $\nu_0$  (Rayleigh scattering) as well as to radiation frequency shifted by an amount  $\nu_k$  on either side of the excitation frequency (Raman scattering). As also shown in equation (2-5), the frequencies on the right hand side imply the presence of Stokes Raman scattering at frequency  $(\nu_0 - \nu_k)$ , and the presence of anti-Stokes Raman scattering at frequency  $(\nu_0 + \nu_k)$ . Only the former has been analyzed in our experiments, because normally the anti-Stokes radiation is of much lower intensity by an amount of the Boltzman thermal factor, and can only be observed under rare circumstances and usually at high temperatures.

In addition, the molecular polarizability, as a function of the nuclear coordinates of the molecule, can be presented in terms of a Taylor series expansion. The polarizability of the xy component can be described by:

$$\alpha_{xy} = (\alpha_{xy})_0 + \sum_k \left( \frac{\partial \alpha_{xy}}{\partial Q_k} \right)_0 Q_k + \frac{1}{2} \sum_{kl} \left( \frac{\partial^2 \alpha_{xy}}{\partial Q_k \partial Q_l} \right)_0 Q_k Q_l + \dots \quad (2-6)$$

where associated with vibration  $k, l, \dots$  are normal coordinates  $Q_k, Q_l, \dots$ , that describe the vibration with their derivative taken at their equilibrium position,  $Q_0$ . Hence, if the vibration produces a change of the molecular polarizability, i.e., if  $\left( \frac{\partial \alpha}{\partial Q} \right) \neq 0$ , then it will be active in the Raman spectrum. This implies that even if the particular crystalline lattice symmetry provides a number of possible normal modes of vibration (phonon modes), only a fraction of these will be Raman-active and exhibit corresponding peaks in the Raman scattering spectra of the material.

## 2-2. Meissner Effect

Superconductivity can be defined as a state of perfect diamagnetism. The perfect diamagnetism of the material implies that the superconducting material does not permit an externally applied magnetic field to penetrate into its interior. For instance, the Type-II superconductors which we measured,  $\text{YBa}(\text{Cu}_{1-x}\text{Ni}_x)_3\text{O}_{7-\delta}$ , are both perfect conductors of electricity as well as perfect diamagnets in their superconducting state. They totally exclude magnetic flux when the applied magnetic field is low, but only partially exclude it when the magnetic field becomes higher. In addition, if the field is applied after the sample has been cooled below its critical temperature, the magnetic flux is excluded from the superconductor.<sup>12</sup> Hence, a superconductor acts like a perfect diamagnet. Both Meissner effects are shown in Fig. 2-2. This phenomenon is called the Meissner effect and was discovered by Meissner and Oschenfeld in 1933. It was also found that  $\mathbf{H}_c$ , the critical magnetic field strength, is quite well approximated by a parabolic law as can be seen in Fig. 2-3 (a), and is given as a function of temperature,  $\mathbf{H}_c(T)$ , as follows :

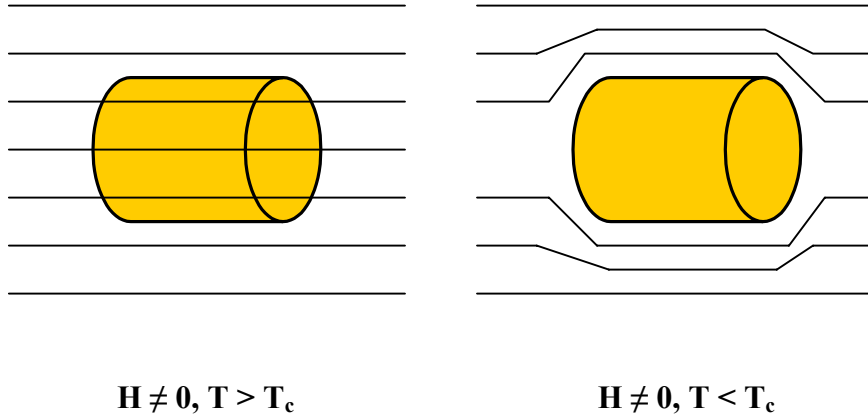
$$H_c(T) \cong H_c(0) \left[ 1 - \left( \frac{T}{T_c} \right)^2 \right] \quad (2 - 7)$$

where  $\mathbf{H}_c(0)$  is the critical magnetic field at 0 K. While the transition in zero field at  $T_c$  is of second order, the transition in the presence of a field is of first order since there is a discontinuous change in the thermodynamic state of the system and an associated latent heat.<sup>13</sup>

In Fig. 2-3(a), the critical magnetic field strength  $\mathbf{H}_c$  depends on the temperature, decreasing when the temperature is raised and falling to zero at the transition temperature

**FIGURE 2-2.** The Meissner effects are shown with (a) changing temperature and (b) changing field.

(a) Holding  $\mathbf{H}$  Constant while Decreasing  $T$



(b) Holding  $T$  Constant while Increasing  $\mathbf{H}$

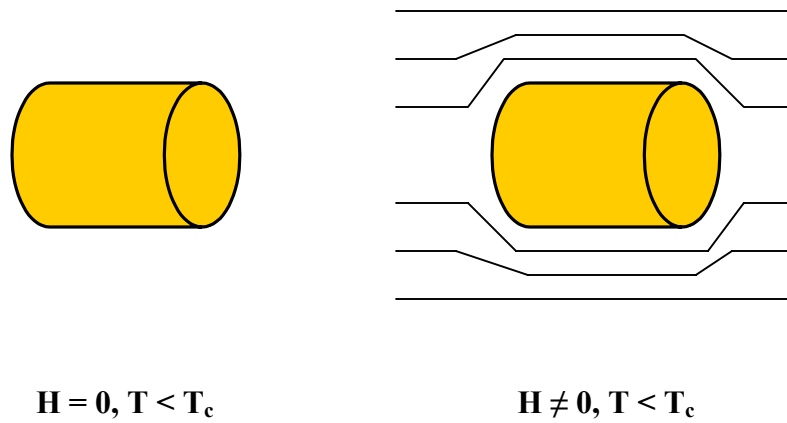
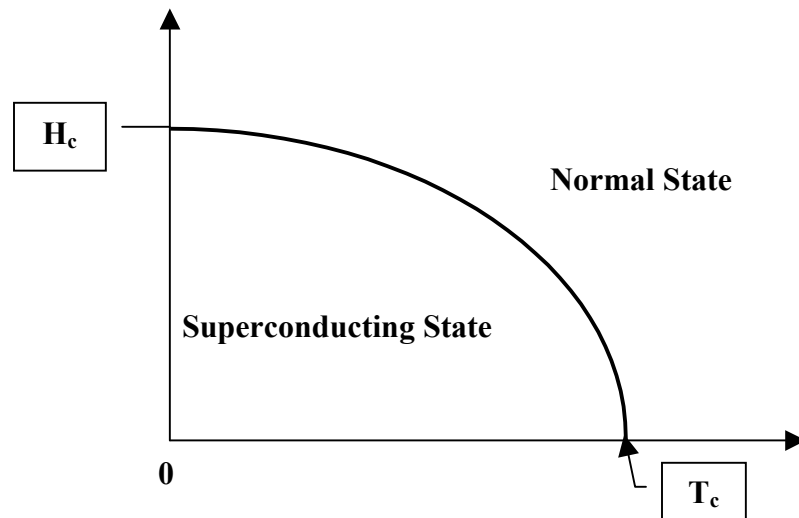
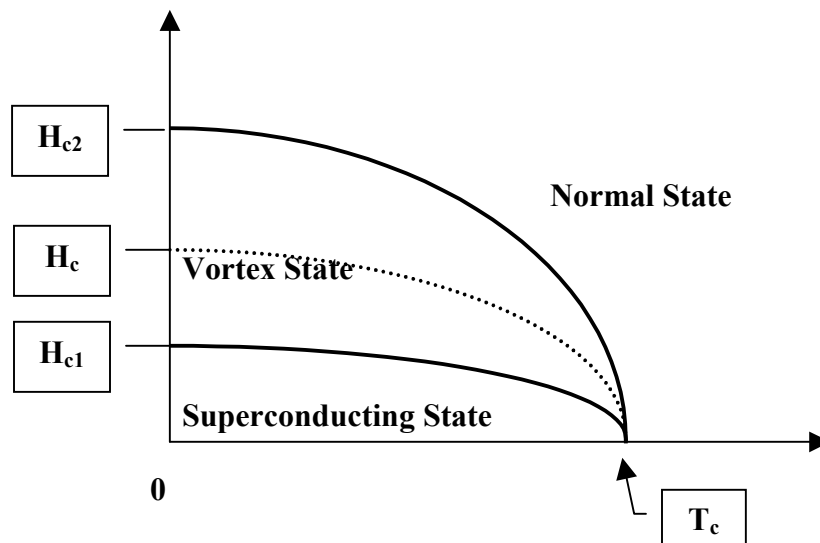


**FIGURE 2-3.** Simplified magnetic phase diagrams showing Type-I and Type-II superconductors are depicted below (Note that  $H_c$  is zero when the temperature  $T$  equals the critical temperature  $T_c$ ).

(a) Magnetic Phase Diagram showing the Superconducting State for Type-I.



(b) Magnetic Phase Diagram showing the Vortex State and the Superconducting State (Meissner state) for Type-II.



$T_c$ . It is known that the flux density  $\mathbf{B}$  outside the sample is always equal to  $\mu_0\mathbf{H}$ , where  $\mathbf{H}$  is the magnetic field strength, so we may equally well refer to the critical magnetic field strength,  $\mathbf{H}_c$ , as a critical magnetic flux density,  $\mathbf{B}_c$ , given by the equation

$$H_c = \frac{B_c}{\mu_0} \quad (2 - 8)$$

where  $\mu_0$  is the permeability of free space. Furthermore, a Type-I superconductor remains superconducting throughout its whole interior when a magnetic field of strength less than  $\mathbf{H}_c$  is applied.<sup>14</sup>

In Fig. 2-3(b), when a gradually increasing magnetic field is applied to a Type-II superconductor, it goes into the mixed state at a “lower critical field”,  $\mathbf{H}_{c1}$ , less than  $\mathbf{H}_c$ . A Type-II superconductor in the mixed state has, however, a lower free energy than if it were Type-I. Therefore, a magnetic field stronger than  $\mathbf{H}_c$  must be applied to drive a Type-II superconductor normal. The highest magnetic field strength up to which the mixed state can persist in a Type-II superconductor is known as the upper critical field,  $\mathbf{H}_{c2}$ .<sup>15</sup>

In our research, the critical current density ( $J_c$ ) for the  $\text{YBa}(\text{Cu}_{1-x}\text{Ni}_x)_3\text{O}_{7-\delta}$  was measured with most of the applied magnetic field ( $\mathbf{H}$ ) values in the range between  $\mathbf{H}_{c1}$  and  $\mathbf{H}_{c2}$  which implies that our sample was in the vortex (intermediate) state during the majority of the experiment to determine  $J_c(\mathbf{H})$ .

### **2-3. Critical Temperature ( $T_c$ ) and Critical Current Density ( $J_c$ )**

Superconducting metals and alloys have a characteristic transition temperature, at which they undergo the conversion from a normal conductor to a superconductor, which is called a critical temperature,  $T_c$ . Although the theoretical transition from the normal to the superconducting state can be very sharp, experimentally it sometimes occurs more or less gradually and sometimes quite abruptly. Below the transition temperature the resistivity of a sample is zero. The sharpness of the drop to zero resistivity can prove as a good relative measure of the purity of the sample and its level of oxygenation, and its structural integrity. On the other hand, narrow and broad superconducting resistivity transitions have both been seen to depend primarily on the level of sample oxygenation. However, it is also clear that when high temperature superconductors are doped with paramagnetic ions at the copper sites, that the transition temperature both shifts to lower values and also broadens.

When the critical current in a sample exceeds a value that is called the critical current density,  $J_c$ , the superconductivity is destroyed. This is called the Silsbee effect.<sup>16</sup> If too much current is applied to a superconducting sample, it will revert to the normal state even though it is yet below its transition temperature at zero current. Therefore, we can say that the critical current density is a function of the temperature, as well as of the externally applied magnetic field.

In addition, the value of critical current density increases from zero at  $T = T_c$  to a maximum value,  $J_c(0)$ , at  $T = 0$  K. As the samples are cooled down through and below the transition temperature,  $T_c$ , the critical current density gradually increases. The explicit



temperature dependence of  $J_c$  on  $T$  is given by the Ginzburg-Landau theory. This temperature dependence takes the form of the following equation,

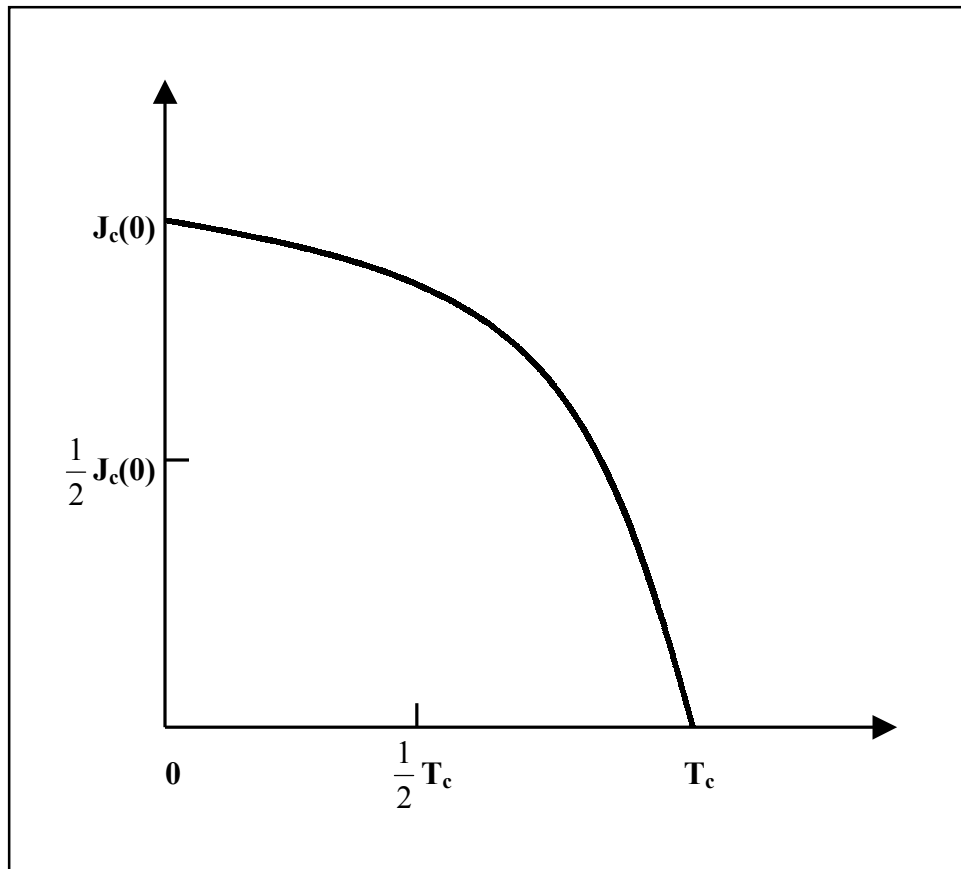
$$J_c = J_c(0) \left[ 1 - \left( \frac{T}{T_c} \right)^2 \right] \left[ 1 - \left( \frac{T}{T_c} \right)^4 \right]^{\frac{1}{2}} \quad (2-9)$$

and is plotted in Fig. 2-4.

## 2-4. Theory of Extended X-ray Absorption Fine Structure (EXAFS)

EXAFS refers to the sinusoidal variation of the X-ray absorption coefficient as a function of the X-ray photon energy, which is actually one region of x-ray absorption fine structure (XAFS) studies. XAFS spectroscopy is concerned with the probability that an x-ray will be absorbed by an atom. When an x-ray photon is absorbed, the photon's energy is transferred to a core electron that becomes an excited photoelectron. This excited photoelectron is then promoted from a ground state to a higher energy level.<sup>17</sup> The energy at which the probability of absorption is greatest is known as the absorption edge for that particular electron. For electrons in the  $n = 1$  shell (the most tightly bound shell), the edge is known as the K-edge, and for the  $n = 2$  shell, there are corresponding L-edges, as well as M-edges for the  $n = 3$  shell.<sup>18,19</sup> This absorption edge is also the binding energy of this electron, and therefore the absorption of the x-ray photon results in the ejection of the excited photoelectron from the atom.<sup>20,21</sup> In most XAFS measurements the most basic information learned is the absorption coefficient of the material. The derivation of the coefficient is actually straightforward starting with the fact that as a collimated x-ray with intensity  $I$  is transmitted through a material of thickness  $X$ , the loss in intensity is a function of the intensity and the change in thickness, or:

**FIGURE 2-4.** This is the temperature dependence of the critical current density  $J_c(T)$  in accordance with Eq. 2-9.



$$dI = -\mu I dx \quad (2-10)$$

$$\frac{I}{I_0} = e^{-\mu x} = T \quad (2-11)$$

where  $T$  is the transmission through the material.  $\mu$  serves as a constant of proportionality, and is defined as the linear absorption coefficient in units of  $\text{cm}^{-1}$ . However,  $\mu$  is dependent on the density of the material, as well. To make up for this, the absorption coefficient is often referred to as the mass absorption coefficient. For a given material with mass density  $\rho$ , the mass absorption coefficient is defined by  $\frac{\mu}{\rho}$  and has units of  $\frac{\text{cm}^2}{\text{g}}$ . In actuality, this constant is not 100 % independent of the physical state of

the material but for all practical purposes it is close enough. The constant  $\frac{\mu}{\rho}$  can be approximated with the summation:

$$\frac{\mu}{\rho} = \sum_j g_j \left( \frac{\mu}{\rho} \right)_j \quad (2-12)$$

where  $g_j$  represents the mass fraction of the element  $j$  that has a mass absorption coefficient  $\left( \frac{\mu}{\rho} \right)_j$ .<sup>22</sup> Regardless of its actual approximation, the mass absorption coefficient is considered to be the standard constant used in XAFS measurements.

Sayers et al.<sup>23</sup> stated that if one were to take a Fourier transform of the EXAFS with respect to the photoelectron wave number,  $k$ , the resulting plot would show peaks that in fact related to the distances of the nearest-neighbor coordination shells of atoms. Since EXAFS does not occur with isolated atoms, but rather for condensed clusters or groups, the basic physics for it goes beyond that of the previously described atomic

absorption. EXAFS focuses on how the ejected photoelectron interacts with the nearest-neighbor atomic shells. If one assumes that all of the x-ray photon's energy is transferred into one core electron, then the ejected photoelectron has kinetic energy that is the difference of the photon energy and the core electron's atomic binding energy. The EXAFS region does not begin usually until 15 eV or more beyond the edge, because then the photoelectron will have enough kinetic energy to be measurable from the inter-atomic interaction energy that is approximately 3 eV.<sup>24</sup> The ejected photoelectron can be, of course, treated as a wave using the basic de Broglie relationship:

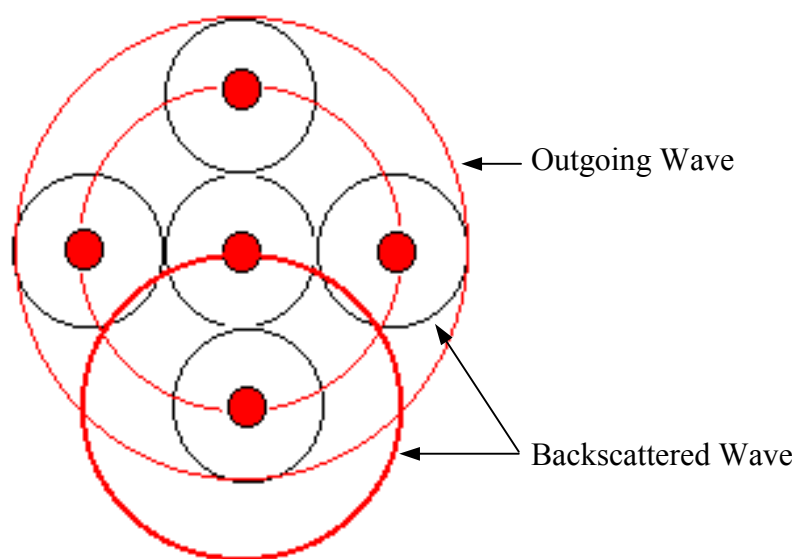
$$\lambda = \frac{h}{P} = \frac{hc}{E} \quad (2 - 13)$$

where  $h$  is Planck's constant,  $p$  is the momentum of the photoelectron, and  $E$  is the energy of the x-ray photon. The momentum  $p$  can also be expressed in the EXAFS region by:

$$\frac{P^2}{2m} = h\nu - E_0 \quad (2 - 14)$$

where  $\nu$  is the frequency of the incident x-ray, and  $E_0$  represents the electron's atomic binding energy. The absorbing atom would have coming out of it a spherical wave. The diagram in Fig. 2-5 is a recreation of a simple Stern model<sup>25</sup> that shows the outgoing electron wave from the absorbing atom interacting with neighboring atoms and the creation of backscattered waves as well. Backscattering occurs when the outgoing wave interacts with the surrounding atoms, and the outgoing wave is scattered in such a way that the surrounding atoms produce spherical waves of their own. The backscattered waves will interfere either constructively or destructively with the initial outgoing wave depending on the relative phase difference. The change in amplitude of the electron will

**FIGURE 2-5.** This is the simple Stern model of EXAFS with outgoing and backscattered waves.



cause a change in the probability of x-ray absorption. As the energy changes in the EXAFS measurement, obviously the wavelength will change inversely, which will in turn change the relative phases between the outgoing wave and the backscattered waves. Therefore, the amplitude changes, which changes the overall probability of absorption. In a plot of absorption versus energy, this process is reflected by the periodic oscillations in the EXAFS region. The peaks correspond to the outgoing wave being in phase with the backscattered waves, while the valleys reflect out of phase waves. The basic EXAFS equation is an approximation that describes  $\chi(k)$ , which is approximately the difference of the actual absorption and the absorption of the embedded probe atom that is normalized to the smooth atomic absorption,<sup>26</sup> e.g.,  $\chi(k)$  is the oscillation or interference in the absorption defined by:

$$\chi(k) = \sum \frac{S_0^2}{kR_j^2} |f_{eff}^j(k)| \sin[2kR_j + \phi^j(k) + 2\delta_c(k)] e^{-2\sigma_j^2 k^2} e^{-2R_j/\lambda(k)} \quad (2-15)$$

where the summation includes all possible scattering paths. The change in the passive electron overlap is factored in with an amplitude correction of  $S_0^2$ . As can be seen,  $\chi$  is a function of the photoelectron wave number  $k$ , which can be defined by the equation

$\lambda = \frac{2\pi}{k}$ . This equation, along with equations (2-13) and (2-14), gives us the equation

for the energy ( $E = h\nu$ ) of the incident X-ray photon as  $\hbar k = \sqrt{2m(E - E_0)}$ , where  $E_0$

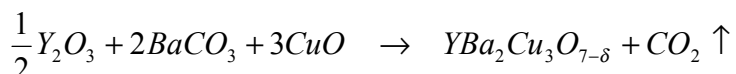
is the core electron's atomic binding energy.  $R$  represents half of the scattering path length, while  $|f_{eff}|$  accounts for the effective scattering amplitude. The phase shift in the electron wave is factored in by  $\phi$ , and  $\delta_c$  adjusts for the probe atomic phase shift. Finally, the error adjustment through the mean squared relative displacement (MSRD) is added

using  $\delta^2$ , while  $\lambda$  is the photoelectron's coherent wavelength.<sup>27</sup> One can note that  $\chi(k)$  is essentially a summation of sine functions, with different amplitudes for each sine function. Therefore, the Fourier transform with respect to  $k$  becomes more and more apparent. In an EXAFS experiment, once one finds  $\chi(k)$ , it is relatively straightforward to arrive at the distances of the nearest-neighborhood shells of atoms, and this is why EXAFS has become a popular method for investigating the structure of a material.

### 3. Sample Preparation and Experiment

#### 3-1. Sample Preparation

In order to produce a control sample of pure  $YBa_2Cu_3O_{7-x}$ , we weighed the stoichiometric amount of each component that was needed for  $\frac{1}{2}$  mole of  $Y_2O_3$ , 2 moles of  $BaCO_3$ , and 3 moles of  $CuO$ . The reaction formula for  $YBa_2Cu_3O_{7-\delta}$  is then given as,



This amounted to 1.12896 grams of  $Y_2O_3$ , 3.946663 grams of  $BaCO_3$ , and 2.386182 grams of  $CuO$ . The pure  $YBa_2Cu_3O_{7-\delta}$  was synthesized under the same conditions as the doped samples to ensure that the oxygen composition  $x$  remained the same and that the nickel concentration was the only parameter responsible for any structural changes. The other samples were doped with low molar-proportional percentages (0.32%, 0.48%, 0.64%, 0.96%, 3.3%) of nickel replacing the copper. The amounts of each sample are summarized as can be seen in Table 1.

We then ground the ingredients with the mortar and pestle until they were in the form of a uniform fine gray powder by passing through a 90  $\mu m$  filter. This mixture of the ingredients was then placed in an alumina crucible, and underwent a first heat treatment in the high-temperature furnace for 3 hours at 930  $^{\circ}C$ . This was followed by a slow cooldown to room temperature with the furnace power shut off. The homogeneous dispersion of gray particles became black in color following the high-temperature chemical reaction with decreasing amounts of unreacted greenish-black patches following the second and third heat treatments, which were identical to the first treatment but helped to ensure a more complete and thorough reaction of all components.



**TABLE 1.** The stoichiometric amounts of each component are measured by an electric scale as below.

	Y <sub>2</sub> O <sub>3</sub> (225.792g/mol)	BaCO <sub>3</sub> (197.33315g/mol)	CuO (79.5394g/mol)	NiO (74.7094g/mol)
0.00%	1.12896g	3.946663g	2.386182g	0
0.32%	1.12896g	3.946663g	2.383796g	0.002241g
0.48%	1.12896g	3.946663g	2.376168g	0.007165g
0.64%	1.12896g	3.946663g	2.360960g	0.014284g
0.96%	1.12896g	3.946663g	2.338295g	0.021289g
3.30%	1.12896g	3.946663g	2.261131g	0.070086g

Intermediate re-grindings of the sample helped to ensure maximal surface exposure to sufficient oxygen. Then, the YBCO samples doped with molar-proportional percentages of nickel, including the control sample, were measured out in amounts of 0.35 grams each and a steel ram and die with a 0.25 inch diameter was then used to fabricate the pellets. Pressure was then applied via the hydraulic press up to 4000 psi. When we removed the pellets from the die, they were usually quite brittle; therefore, great care was required in the removal. We fabricated five pellets for each compound, and then placed them into a crucible for sintering. The final pelletized samples of the polycrystalline superconductors were then obtained by sintering for 4 hours at 950 degrees Celsius in air. The full oxygenation of the pellets was then ensured by a follow-up annealing in an oxygen-rich atmosphere for 18 hours at 400 degrees Celsius, immediately following the sintering process. For both of these processes, the quartz tube furnace was programmed for a heating and cooling rate of 120 °C per hour.

### **3-2. The Raman Scattering Measurement**

As mentioned in Chapter 2-1, the energy levels and transitions related to the Raman effect can be recorded via conventional Raman spectroscopy using visible lasers. Raman scattering has been extensively used to study the vibrational, electronic, and magnetic properties of high-temperature superconductors.<sup>28</sup> Many theoretical and experimental studies of high temperature superconducting materials have been carried out in weakly doped materials.<sup>29-31</sup> We have studied the Raman scattering for pure and nickel substituted Y-123, that is,  $\text{YBa}_2(\text{Cu}_{1-x}\text{Ni}_x)_3\text{O}_{7-\delta}$ , which has an O-deficient perovskite structure whose superconducting properties depend critically on both  $x$  and  $\delta$ , the latter of

which approached zero in our case. In our experiments, as can be seen in the schematic of Fig. 3-1, the Raman scattering measurements were taken in a backscattering subtracted configuration utilizing the 514.5 nm line of an Argon-Ion Laser with an incident power of approximately 150 mW at the surface of our annealed superconducting pellets, which were mounted on the cold finger of a closed-cycle Leybold helium refrigeration system. The temperature stability during an experimental run was  $\pm 0.5^\circ\text{C}$  and the temperature was monitored by the use of a Carbon-Glass Resistor. The scattered beam was analyzed by a TRIAX-550 (550 mm focal length) imaging spectrometer possessing a 0.025 nm specified resolution and equipped with a 1200 grooves/mm selective single diffraction grating, an air-cooled GaAs PMT (Photo-Multiplier Tube), and a holographic super-notch plus filter. The purpose of the super-notch plus filter was to shield out the unwanted background laser radiation, thus protecting the sensitive PMT, as well as increasing the signal-to-noise ratio for the data. The remaining specifications of the TRIAX –550 imaging spectrometer are provided in Table 2. Spectral data were taken in the superconducting phase of the material at a temperature of 20 K with an automated data collection system, utilizing a Spectra Max data acquisition device interfaced to a Gateway computer operating under a Lab-View software environment. Data thus collected were then analyzed and plotted according to their intensity as a function of their frequency shift in  $\text{cm}^{-1}$  from the incident laser line.

For the LabView Program used in the Raman Scattering Measurement, Fig. 3-2 depicts the spectral data collection program of LabView<sup>32</sup>, which contains the information about the control system of the laser wavelength, the spectrometer scanning

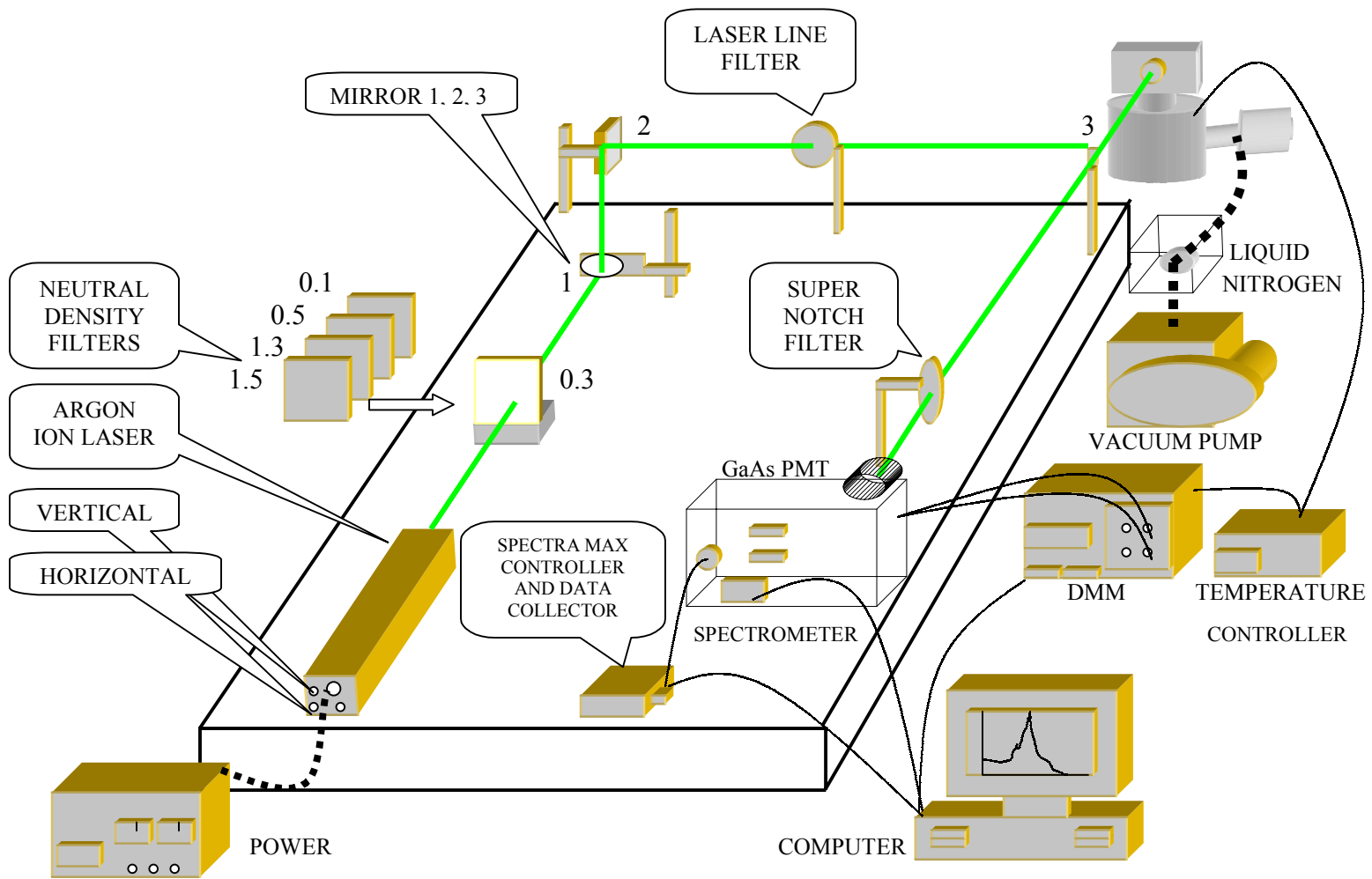
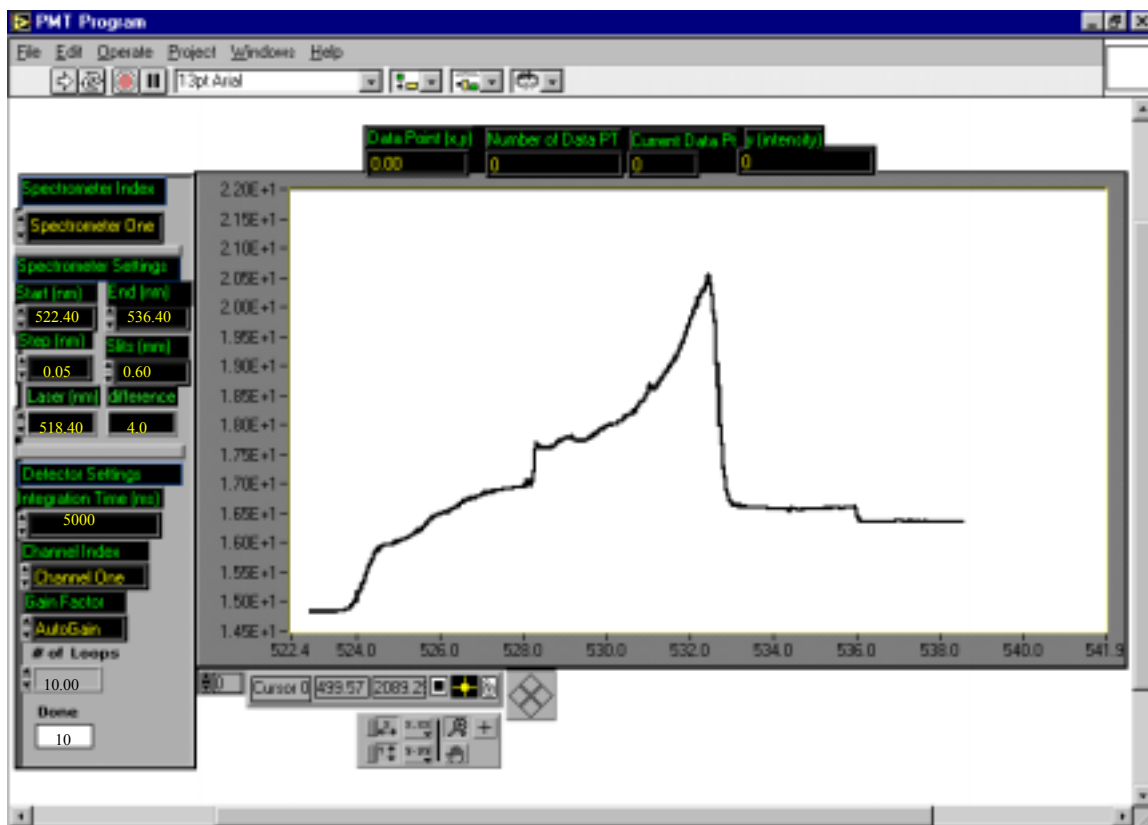


**FIGURE 3-1.** This shows a schematic of the Raman scattering experimental setup in the WIU physics department optical spectroscopy research laboratory.

**TABLE 2.** Specifications of the TRIAX –550 imaging spectrometer are below.

Focal Length	550mm
Spectral Range	0-1500nm mechanical range (1200g/mm grating) 0-40 $\mu$ m spectral range with appropriate gratings
Aperture	F/6.4
Dispersion	1.55nm/mm
Resolution	0.025nm(single channel)
Flat Field	30 x 15mm
Grating Turret	Triple automated on-axis grating turret
Accuracy	+/- 0.3nm
Repeatability	+/- 0.05nm
Slits	High precision motorized Optional motorised side entrance and exit slits
Dimensions	400 x 565 x 190mm
Control	Motorised with built in RS232/IEEE488 interfaces Windows or DOS software

**FIGURE 3-2.** This is a diagram of the spectral data collection program written in our laboratory operating in the LabView environment.

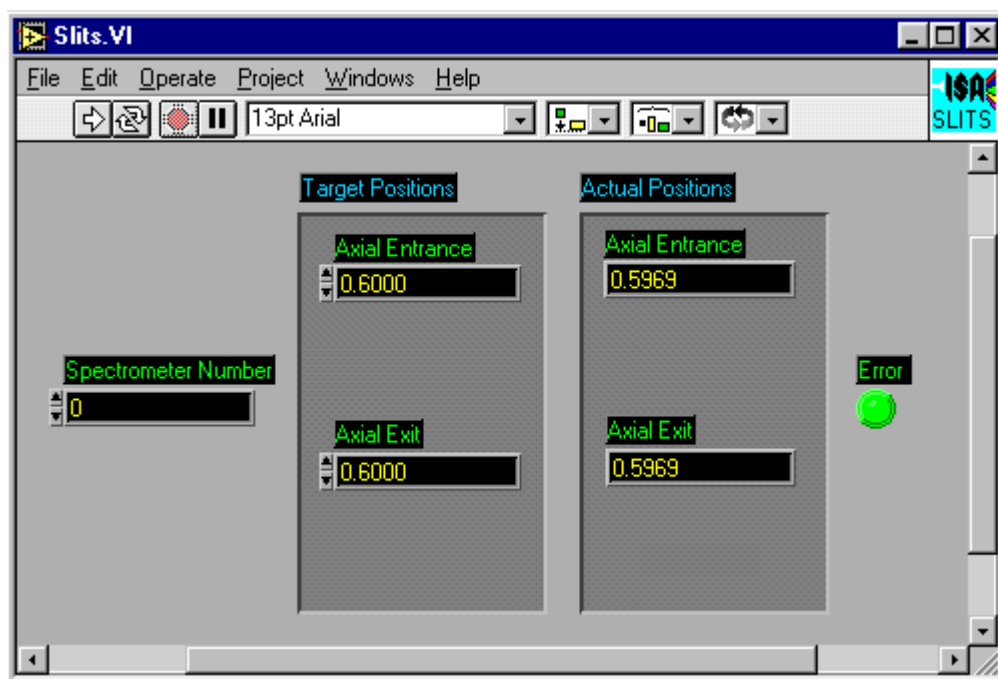


wavelength, and the detector settings. And Fig. 3-3 shows a diagram of the slit controller program that determines the widths of the axial entrance and exit slits of the spectrometer. In order to observe the sample temperature in the cold finger, a temperature monitoring program, as can be seen in Fig. 3-4, was constructed by Tom Boyle (an undergraduate student) and Laurie Pichla (a graduate student) in the WIU physics department. This environment is useful for obtaining and plotting the data from the spectrometer. LabView is a virtual instrument (VI) program, which utilizes a fully featured programming language G. It is a graphical language quite unique in the method by which code is constructed and saved. It plays a role in a diagrammatic view of how the data flows through the program. G is the "native" language of LabView, which is the code produced under the LabView system. The basic schematic as can be seen in Appendix A is that the passage of data through nodes within the program determines the order of execution of the functions of the program. LabView VI's have inputs, process data, and produce outputs. By chaining together VI's that have common inputs and outputs it is possible to arrange the functions in the order by which the programmer wants the data to be manipulated. Often a single input is used as a common "thread" running through several VI's and the program to force the order of operations.

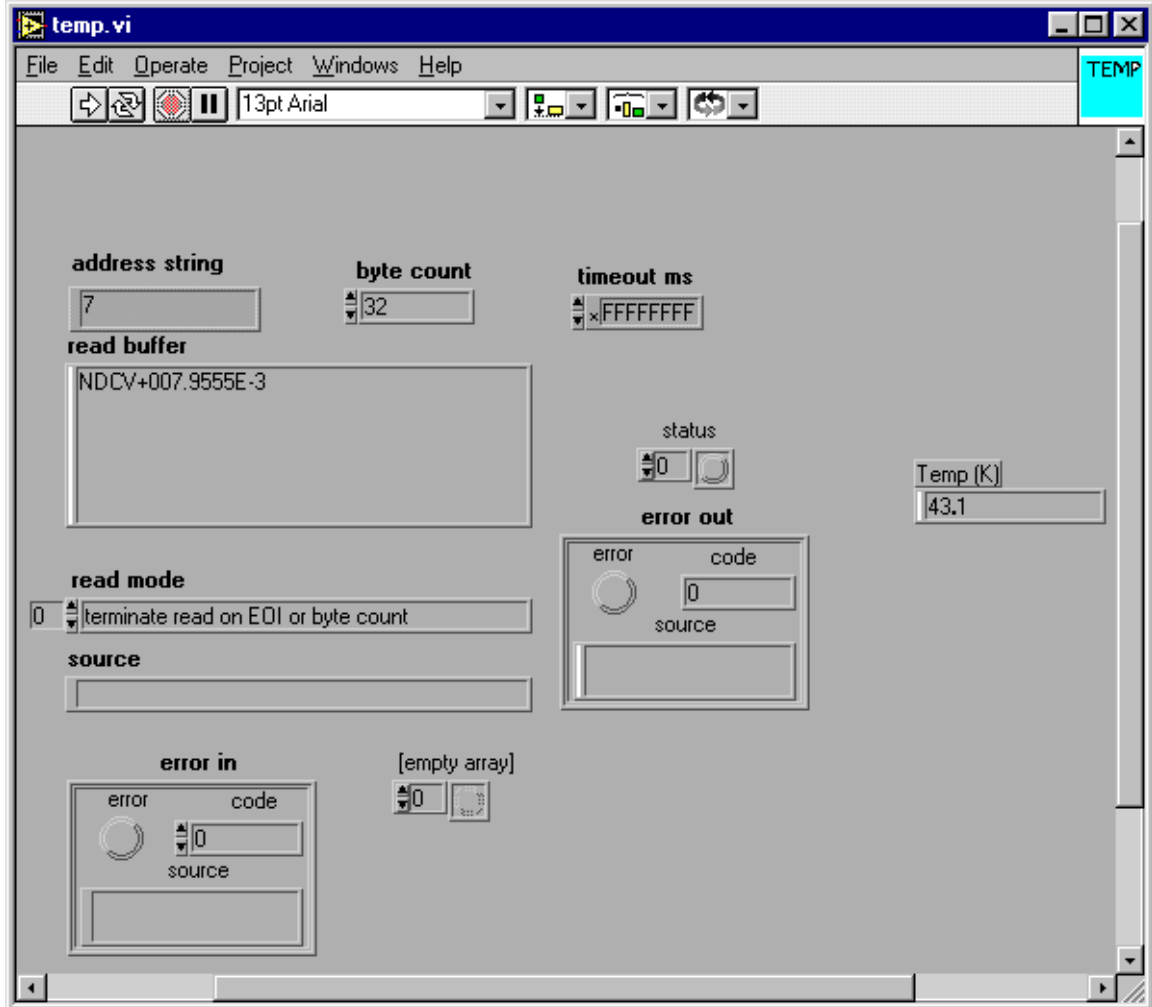
### **3-3. The Critical Temperature ( $T_c$ ) and Critical Current Density ( $J_c$ ) Measurement**

For the measurements of the critical state parameters, we used the same samples as were prepared for the Raman scattering measurements. The dimensions of the sample pellets were 0.635 cm in diameter (1/4") and of 0.15 cm thickness, yielding a cross-sectional area for current flow of  $0.033 \text{ cm}^2$ . In order to measure the electrical resistivity

**FIGURE 3-3.** This is a diagram of the slit controller program in LabView.





**FIGURE 3-4.** This is a diagram of the temperature monitoring program in LabView.

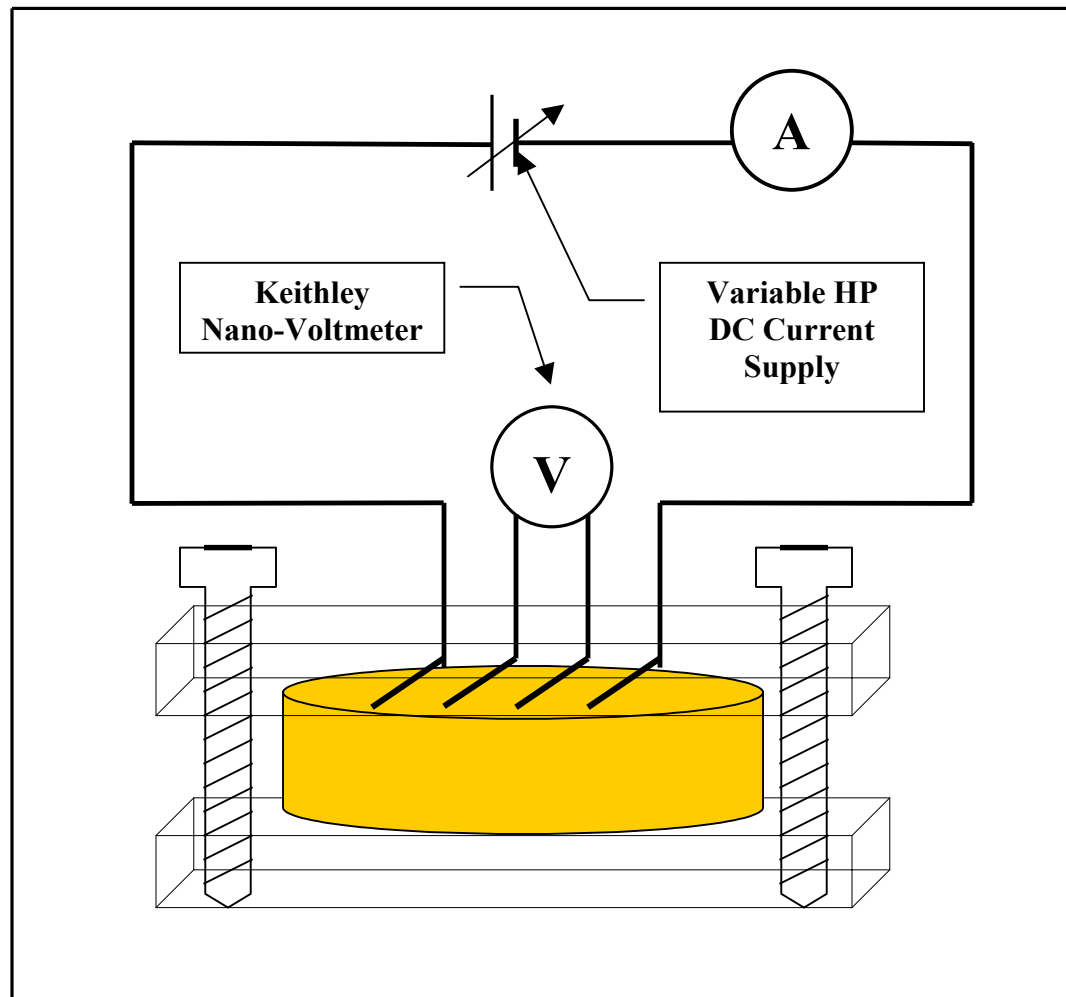
of the sample, four leads are electronically linked to the sample surface via mechanical pressure contacts. This four point probe, using mechanical pressure contacts, was designed in the WIU Physics Department Superconductivity Research Laboratory, and is a very versatile device for the investigation of electrical phenomena in superconducting materials. A schematic of the four point probe is shown in Fig. 3-5. The four point probe device has been designed without any ferromagnetic parts to eliminate any potential interference. Typically, the resistance of the points of contact (the so-called contact resistance) is eliminated from the sample voltage measurement, since the voltage leads lie between the outside current supply leads. Our HP power supply has a digital readout of the current in amperes, as well as the supply voltage in mV necessary to maintain that level of current. The voltage drop across the inside voltage leads is measured by the Keithley digital nano-voltmeter. Then the device is placed inside a low temperature cryostat, between the poles of a large magnet, that allows for slow uniform cooling without contact of the sample with the liquid nitrogen. A constant 3 mA current is provided through the cross-section of the sample pellet, and the sample voltage is continuously monitored as the sample temperature is gradually lowered. Then *Ohm's*

*Law*,  $R = \frac{V}{I}$ , is used to calculate the sample resistance R in *Ohms*. Then the sample

resistivity,  $\rho = \frac{RA}{L}$ , where A is the cross-sectional area of the sample and L is the

length between the voltage leads, is calculated and plotted as a function of the sample temperature. The resistance of the portion of the sample between the voltage probes is the ratio of the voltage registered on the voltmeter to the value of the output current of the power supply. The temperature dependence of resistivity for the pure Y-123 and the

**FIGURE 3-5.** This is a schematic of the four point probe to measure the critical temperature and the in-field critical current.



nickel-substituted  $\text{YBa}_2(\text{Cu}_{1-x}\text{Ni}_x)_3\text{O}_{7-\delta}$  are all plotted by the computer from room temperature to the liquid nitrogen temperature of 77 K.

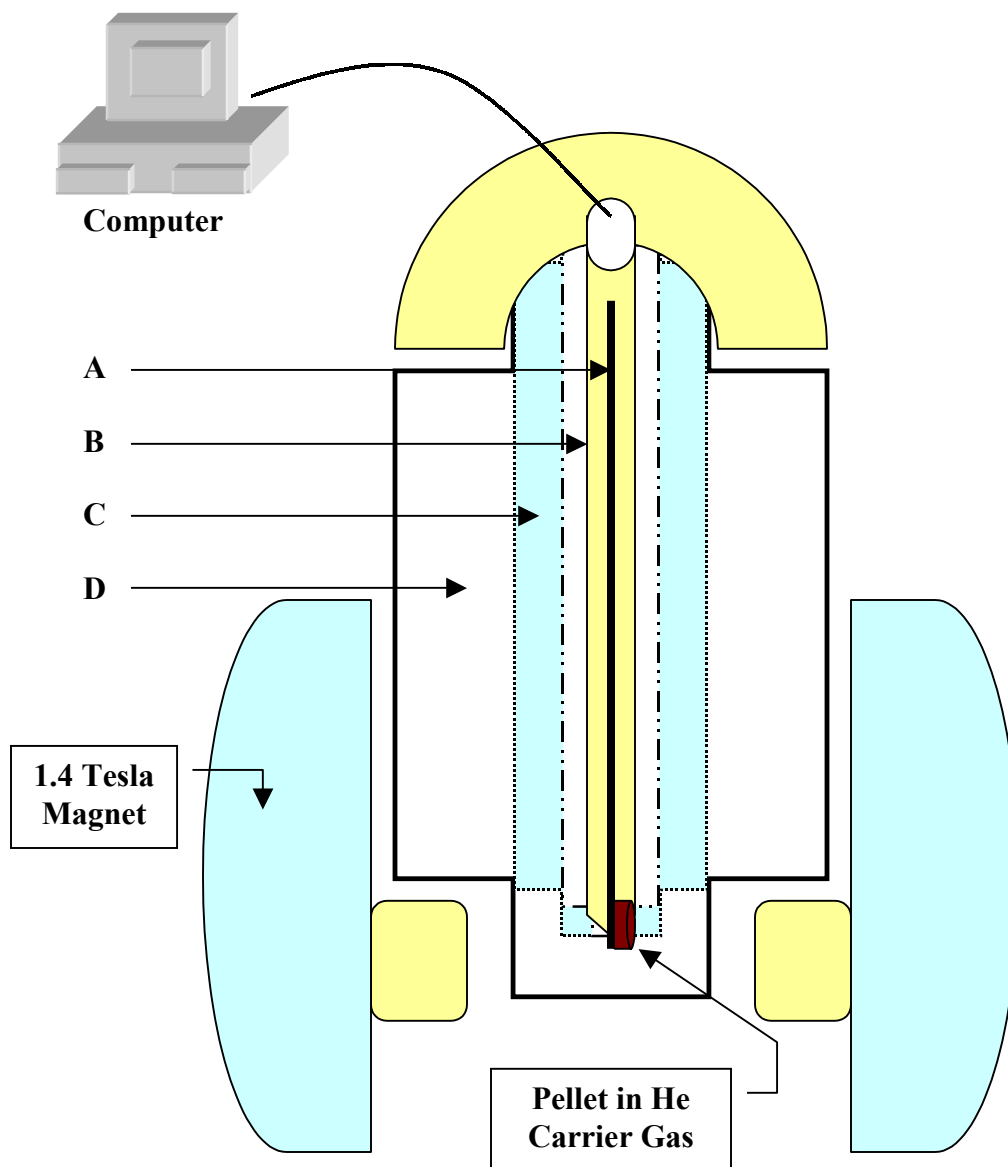
Then the critical current density, as a function of the applied magnetic field of the superconducting materials, can also be measured using the same four point probe as described above. The critical current density,  $J_c$ , is an important parameter for the characterization of high- $T_c$  superconductors, especially in determining their technological applications. The critical current,  $I_c$ , of a superconductor can be defined as the maximum current that the superconductor can carry at a particular value of temperature and applied magnetic field.<sup>33</sup> At each value of applied magnetic field, the current is automatically ramped by the HP-DC current supply under computerized control by a  $C^{++}$  program<sup>34</sup>, until a transition to the non-superconducting state occurs. The measured  $I_c$  versus the magnetic field over the range of 0 to 12000 Gauss can then be recorded and plotted. Before plotting, the critical current density,  $J_c$ , is calculated by applying the formula,

$J_c = \frac{I_c}{A}$ , where  $A$  is the cross-sectional area ( $A = 0.033 \text{ cm}^2$ ) of the pellet through which

the applied current passed.

In order to measure the critical current associated with the presence of an externally applied magnetic field, a liquid nitrogen cryostat equipped with a 1.4 Tesla magnet has been used. A schematic diagram of the cryostat is shown in Fig. 3-6. The cryostat consists of an inner cylindrical sample chamber A surrounded by three chambers. Chamber A contains the four point probe with the sample, and both chamber A and B can be back-filled with helium gas to accelerate the warming or cooling processes. Chamber C is filled with liquid nitrogen to indirectly cool down the chamber A, thus allowing chamber B to play the role of insulating the chamber A, while chamber D is a

**FIGURE 3-6.** This is a schematic of the liquid nitrogen cryostat used for critical state measurements in the WIU physics department superconductivity research laboratory.



- A : Sample Temperature (He Carrier Gas Vacuum)
- B : Temperature Between Sample and Nitrogen (Vacuum / He Carrier Gas)
- C : Liquid N<sub>2</sub>
- D : Vacuum

large vacuum jacket to insulate the liquid nitrogen in chamber C from the exterior. By continuously supplying liquid nitrogen into chamber C, the sample temperature of 77 K can be easily achieved. Then the temperature of 60 K as attained during part of our data collection process can be reached by using a large vacuum pump to produce a partial vacuum over a finite closed reservoir of the liquid nitrogen surrounding the sample cryostat, as chamber C is closed off and vacuum sealed.

### 3-4. EXAFS Measurement

The samples for EXAFS measurements should have a thickness on the order of 10  $\mu\text{m}$  in order for the transmission to be between 33 % and 66 %, since the  $\text{YBa}_2\text{Cu}_3\text{O}_{7-\delta}$  was so optically dense, by using the equation  $T = \frac{I}{I_0} = e^{-\mu x}$ , where  $T$  is the transmission through the material,  $I$  is the intensity,  $\mu$  is a constant of proportionality, and  $x$  is the thickness of the material. This equation was used to find the linear absorption coefficient for  $\text{YBa}_2\text{Cu}_3\text{O}_{7-\delta}$ . Unfortunately, the mass absorption coefficient for YBCO could not be found in the literature. However, it was possible to use the additive nature of the linear absorption coefficient. All that was necessary was to find the linear absorption coefficient for the Y, Ba, Cu, and O.

In an undoped molecule of  $\text{YBa}_2\text{Cu}_3\text{O}_{7-\delta}$  there were 13 atoms present (assuming  $\delta = 0$ ). Multiplying the mass density of  $\text{YBa}_2\text{Cu}_3\text{O}_{7-\delta}$  by the fractional amount of each element in the  $\text{YBa}_2\text{Cu}_3\text{O}_{7-\delta}$  would yield the mass density of each element in the molecule. The mass absorption coefficients for the elements were found in reference tables for energies around the Ni-edge (8.333 keV). Table 3 shows these values along

**TABLE 3.** These are the fractional densities of the total density and absorption coefficients.

	Y (1/13)	Ba (2/13)	Cu (3/13)	O (7/13)	YBa <sub>2</sub> Cu <sub>3</sub> O <sub>7-δ</sub>
Proportional Constant					
[ $\mu$ (cm <sup>-1</sup> )]	38	217	64.6	23	343
Mass Density					
[ $\rho$ (g/cm <sup>3</sup> )]	.423	.846	1.27	2.96	5.5
Mass Absorption					
Coefficient	89.72	256.5	50.85	7.747	---
[ $\mu/\rho$ (cm <sup>2</sup> /g)]					

with the densities calculated, as well as the reference mass absorption coefficients. All the elements' values were found for 9 keV except for Cu, because it goes through its edge at 8.979 keV. Once past the edges, its absorption increases dramatically. Incidentally, the EXAFS measurements had to be cut short due to the Cu-edge. Rather than measuring for another 1000 eV past the edge, measurements went out to only about 8.9 keV.

For the thickness of the Ni-doped  $\text{YBa}_2\text{Cu}_3\text{O}_{7-\delta}$  samples, transmission was changed by 20% at the Ni-edge. The 0.32% sample was chosen for the calculation as it contained the most dilute amount of Ni. Two values of the Ni linear absorption coefficient calculated were one pre-edge ( $0.261 \text{ cm}^{-1}$ ) and one post-edge ( $1.5 \text{ cm}^{-1}$ ). The following system of equations in Eq. (3-1) and (3-2) was produced using  $T$  and  $x$  as the respective transmission and sample thickness.

$$T = e^{-43x} \quad (3-1)$$

$$0.8T = e^{-330x} \quad (3-2)$$

It was not noticed until later that an error had been made in writing these equations. Using the incorrect coefficients had resulted in an ideal thickness of  $7.8 \text{ }\mu\text{m}$ , while the correct linear coefficients of  $343.261 \text{ cm}^{-1}$  and  $344.5 \text{ cm}^{-1}$  (pre-edge and post-edge, respectively) yield a thickness of  $1.8 \text{ mm}$ , a much thicker sample. As large as this error was, it fortunately turned out to be a moot point for two main reasons. First of all, this algebraic process had been to find at what thickness did a *change* in the transmission occur at the Ni-edge, which then ignored what the actual transmission was before and after the edge. By the transmission equation and the correct coefficients, it turns out that the ideal thickness of  $1.8 \text{ mm}$  would have resulted in a change in transmission from  $1.47\text{E-}27$  to  $1.17\text{E-}27$ . Even though this is a 20 % change in the transmission, there



would not have been enough signal to make an adequate measurement. The second reason why this error is not as severe as it should have been, and for that matter why it was not even noticed until this report was being written, is because the EXAFS measurements were performed using fluorescence rather than transmission. When the x-rays strike a material, some of the photons are transmitted while some are absorbed by exciting a core electron. The transition back to the ground state results in fluorescence. However, in fluorescence measurements, the thickness of the sample is irrelevant.

The equipment setup for the EXAFS measurement was far from elaborate, which is another reason why EXAFS is an attractive method of study. For EXAFS measurements, a high intensity beam is necessary for a good signal to noise ratio, and generally this implies a synchrotron radiation source at a large facility. A representative setup is shown in Fig. 3-7. The detectors were Lytle ion detectors using Argon gas to fill the chamber. From the X-ray source, the incident X-ray beam is directed towards a curved-double crystal monochromator using a (111) diamond set at a  $45^\circ$  angle to the incident angle, in order to reduce the intensity, while also providing the opportunity for a fluorescence measurement. The beam intensity must be measured prior to entering the sample, so an incident detector ( $I_0$ ) is in-line before the sample. After the sample, another detector ( $I_1$ ) is used to determine the transmission intensity. In this case, a fluorescence detector to the side of the sample can be used for fluorescence studies.

First, the powder was smeared onto the Kapton™ tape, and the excess powder was shaken off and discarded. However, this did not produce a uniform spread across the sample holder. In addition to the sporadic holes, there was also a problem with the adhesive not holding onto the powder very well, which resulted in a thicker sample

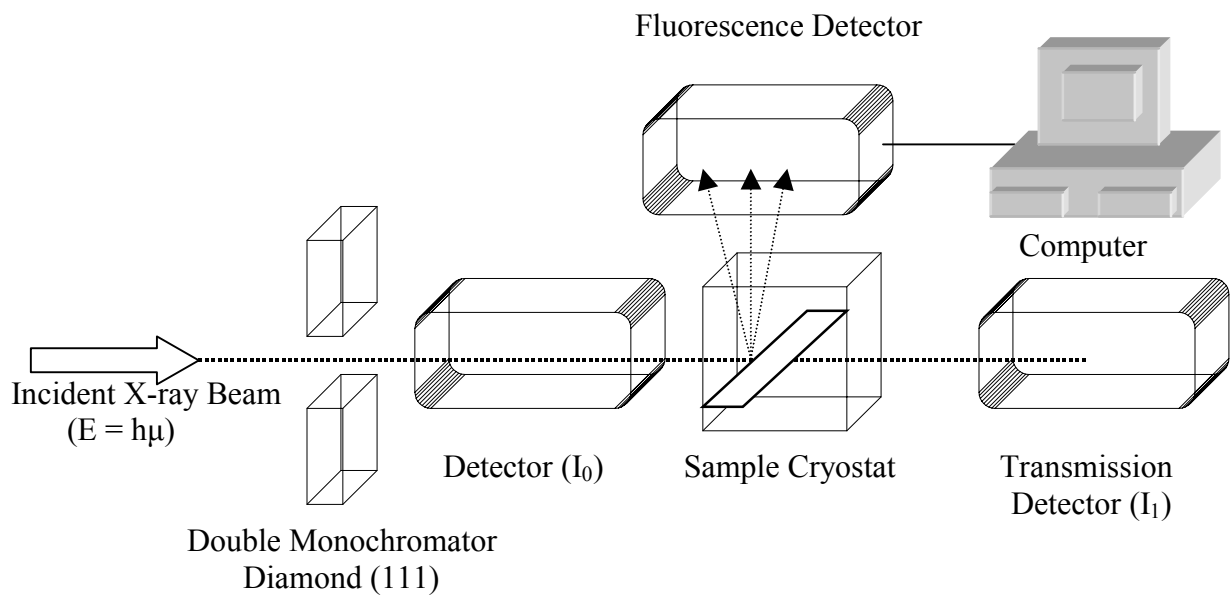


**FIGURE 3-7.** This is the schematic of the EXAFS equipment setup.

towards the bottom of the plate. By this point, it was realized that the combination of the higher than desired density and the extremely dilute presence of the metal being measured made it all but impossible to measure EXAFS via transmission. It was then decided to use fluorescence, which quickly resolved the problem in preparing the samples. The samples were prepared by placing a piece of Kapton™ tape over one side of the plate and then pouring enough powder into the holder in order to be even with the plate. The other piece of Kapton™ tape was carefully placed over the sample, and the tape was manually pressed to attempt a uniform thickness of the powder while also maximizing the amount of powder captured by the adhesive. The 0.32% sample was thicker than the other two samples. However, this difference could now be neglected since the measurements were going to be performed with fluorescence.

As the energy increased past the Ni-edge, it was approaching the Cu-edge, which resulted in the pre-edge of the Cu to begin to appear, hence the sudden curve at the end of the plot. To counter this, each graph was truncated, resulting in a plot over an energy range of 8.2-8.8 keV. More explanation is also contained in the B.S. Honors Thesis of Michael C. Baxa, who also completed his B.S. Honors degree in physics from WIU in May 2002.

The degrees chosen for the polynomial were a 1<sup>st</sup> degree polynomial for the pre-edge, and a 3<sup>rd</sup> degree for the post-edge region. A section of the pre-edge is selected, and a line is then fitted to the region. Then, a cubic polynomial is fitted to a selected post-edge region. Afterwards, WinXAS 97v1.3 extrapolates the fitted line to extend across the entire graph, and then takes the difference between the two plots. Then, WinXAS 97v1.3

normalizes the resulting plot to the cubic polynomial fit.<sup>35</sup> The theory behind this process goes back to the fact that  $\chi$ , the interference function as a function of  $E$ , is defined by:

$$\chi(E) = \frac{\mu(E) - \mu_0(E)}{\mu_0(E)} = \frac{\mu(E)}{\mu_0(E)} - 1 \quad (3-3)$$

where  $\mu(E)$  is the absorption measured experimentally, and  $\mu_0(E)$  is the absorption that would be expected from an isolated atom, and is based on the experimental positioning of the edge.<sup>36</sup> Graphically,  $\mu_0(E)$  would appear as a straight line of slope zero, after normalization, with a discontinuity at the absorption edge of the material. In other words,  $\mu_0(E)$  past the edge graphically represents the equilibrium of the absorption oscillations, because it represents zero interactions physically. The  $\chi$  function of interest is that of  $\chi$  as a function of the wave number,  $k$ . Using  $\hbar k = \sqrt{2m(E - E_0)}$  or approximately,  $k = \sqrt{265.25(E - E_0^{\text{exp}})}$  for  $k$  in  $\text{\AA}^{-1}$  and  $E$  in keV, the plots for each sample are converted from absorption vs. energy to  $\chi(k)$  vs.  $k$ . WinXAS 97v1.3 determines the threshold or absorption-edge energies,  $E_0$ . For further information on this analysis, the interested reader should consult the B.S. Honors Thesis by Michael C. Baxa, May 2002, WIU Physics Department.

## 4. Discussion of the Results

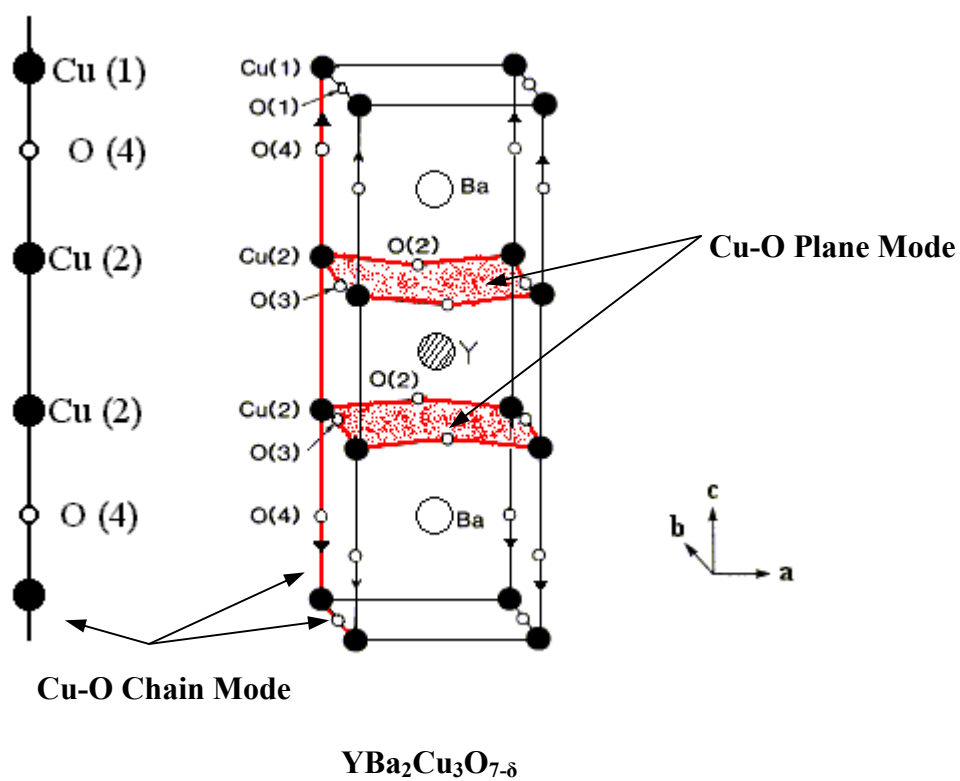
### 4-1. Raman Scattering Analysis

In general, the selective introduction of impurities through stoichiometric chemical dopants is preferable to other techniques such as radiation damage<sup>37</sup>, which introduces a wide variety of scattering centers throughout the cross section of the sample. However, Ni has been thought to substitute preferentially into the Cu(2) plane site<sup>38</sup> in  $\text{YBa}_2\text{Cu}_3\text{O}_{7-\delta}$  while there has been some evidence of Ni doping into the Cu(1) chain sites<sup>39</sup> previously as well. In this present study, we have attempted to investigate both of these possibilities at the lower levels of doping.

The sketch of the orthorhombic  $\text{YBa}_2\text{Cu}_3\text{O}_{7-\delta}$  unit cell is illustrated in Fig. 4-1. The numbers in parentheses beside the atomic symbols show the valence states of the atoms at those sites. Along the **b** direction are the O(1) atoms that form the Cu(1)-O(1) chains. There are no equivalent oxygen atoms along the **a** direction and hence no Cu(1)-O(1) chains in this direction. Also, a segment of the linear chain used in theoretical calculations is shown at the left; this is the chain formed by Cu(2) atoms and O(4) atoms, and lies along the **c** direction.

The Raman spectra for nominally pure Y-123 and for  $\text{YBa}_2(\text{Cu}_{1-x}\text{Ni}_x)_3\text{O}_{7-\delta}$  with low Ni concentrations of  $x = 0.0032$ ,  $x = 0.0064$ ,  $x = 0.0096$ , and a higher Ni concentration of  $x = 0.033$  are shown in Fig. 4-2(0.00%), Fig. 4-3(0.32%), Fig. 4-4(0.64%), Fig. 4-5(0.96%), and Fig. 4-6(3.3%), respectively. The first phonon spectra, of the pure Y-123 with orthorhombic structure, demonstrates a strong feature at  $458 \text{ cm}^{-1}$  which can be easily identified from the literature<sup>40</sup> as the phonon corresponding to the in-phase oxygen mode vibration, temperature corrected from the room temperature value of

**FIGURE 4-1.** Primitive unit cell of stoichiometric  $\text{YBa}_2\text{Cu}_3\text{O}_{7-\delta}$ . The stretching motion is indicated by the arrows on the O(4) atoms. A segment of the linear chain used in theoretical calculations is shown at the left.<sup>41</sup> (Altendorf *et al*)



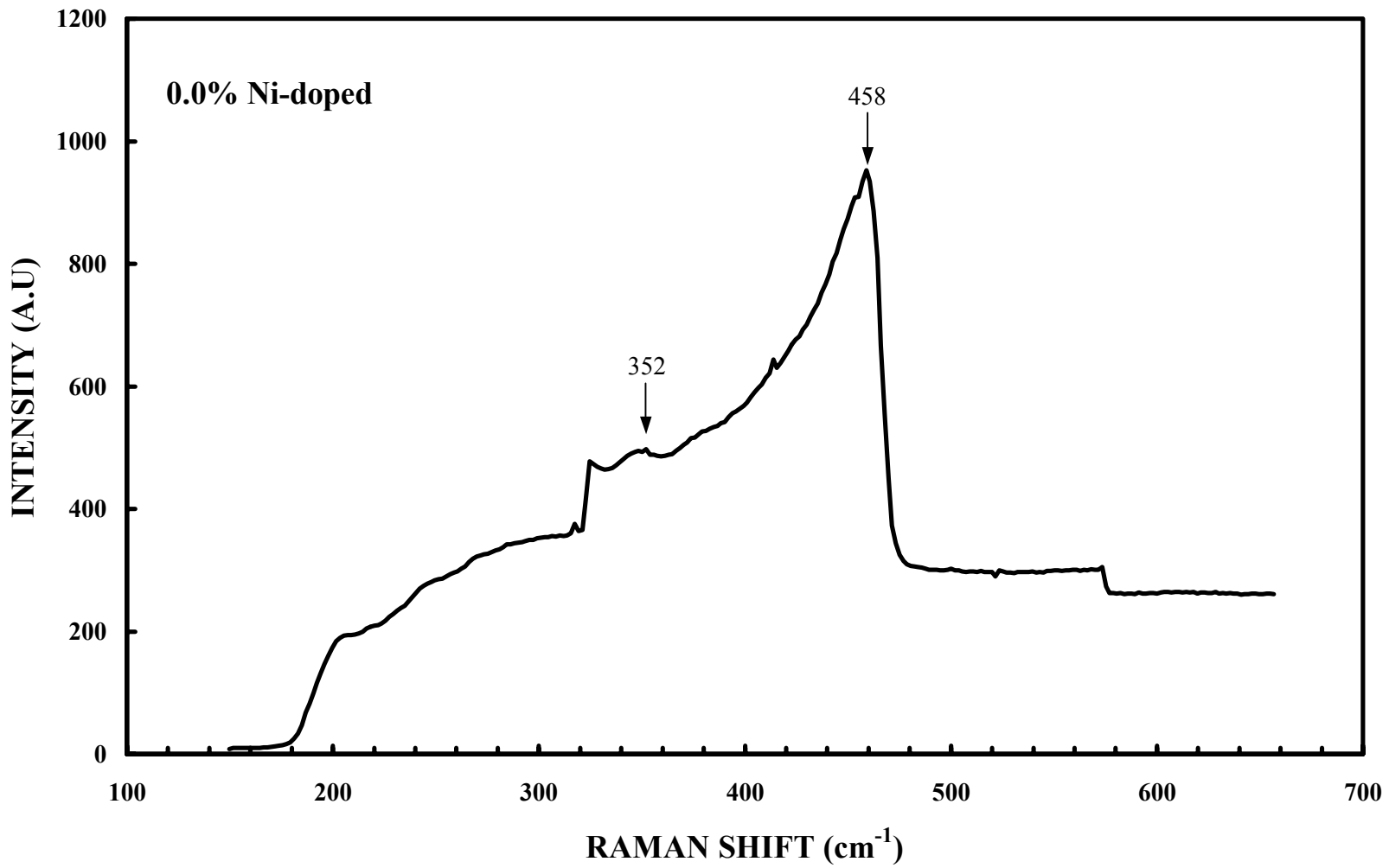
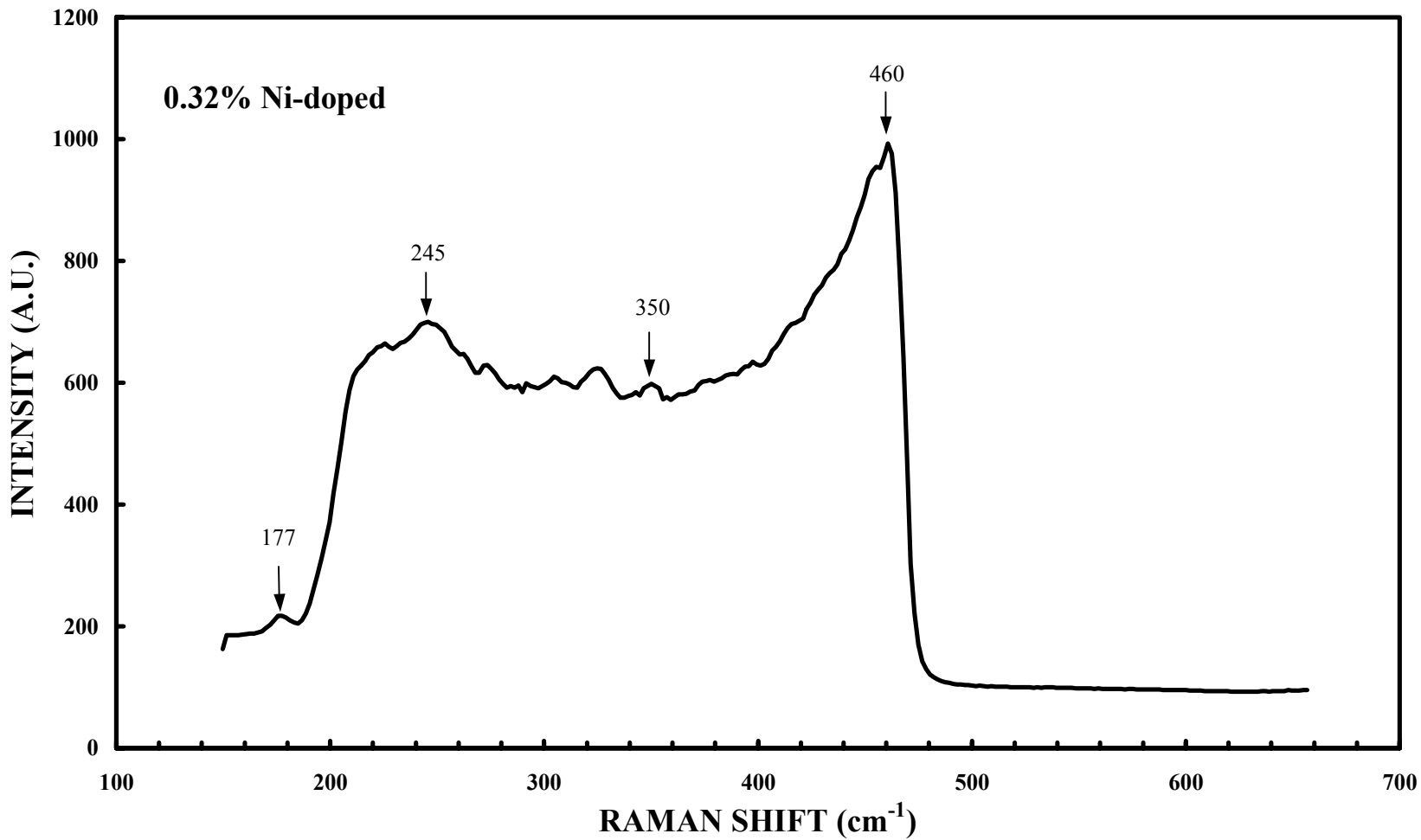
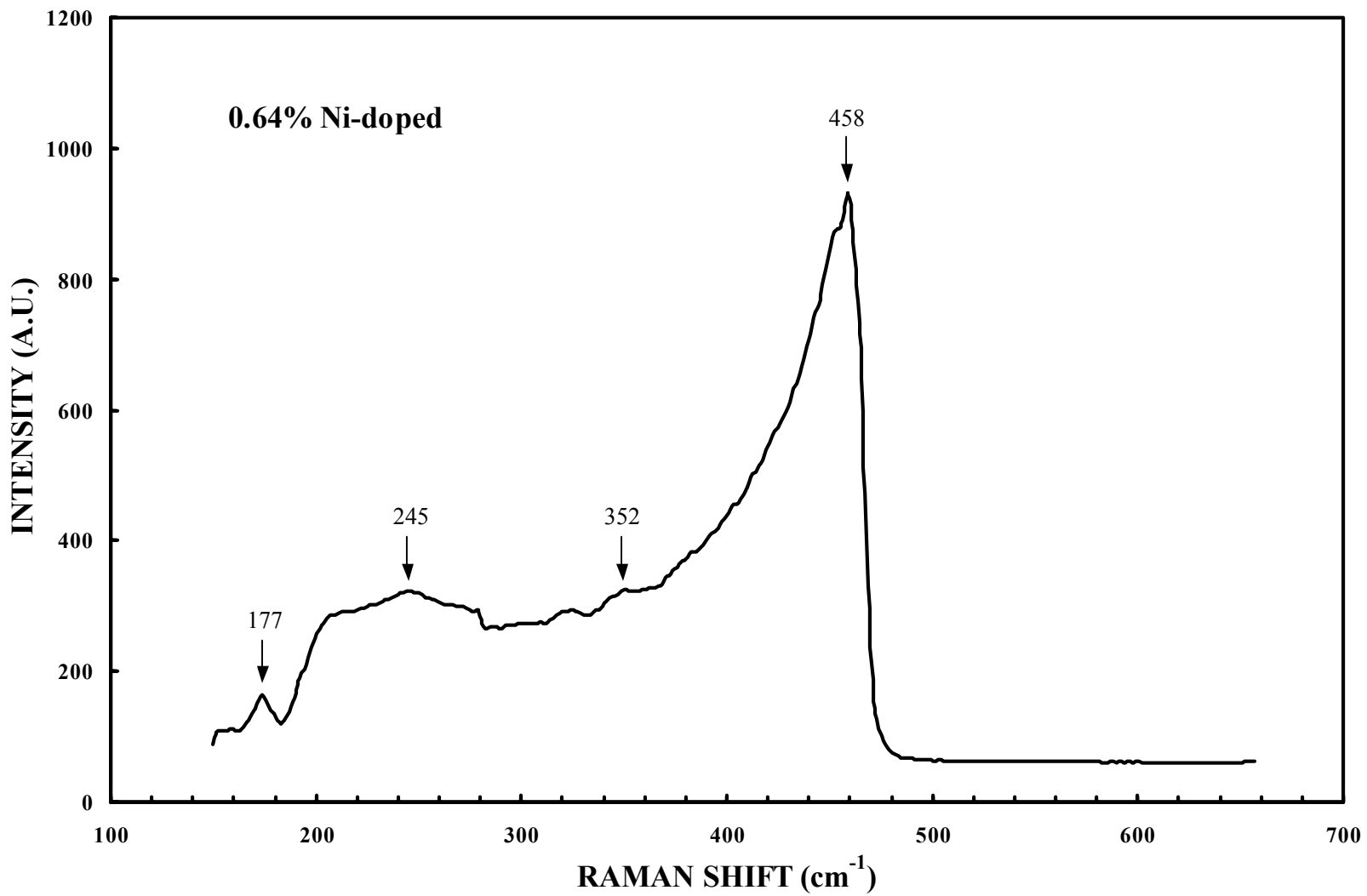


FIGURE 4-2. This is the Raman spectrum for undoped  $\text{YBa}_2\text{Cu}_3\text{O}_{7-\delta}$  ( $\delta = 0$ ).



**FIGURE 4-3.** This is the Raman spectrum for  $\text{YBa}_2(\text{Cu}_{1-x}\text{Ni}_x)_3\text{O}_{7-\delta}$  ( $x = 0.0032$ ,  $\delta = 0$ ).





**FIGURE 4-4.** This is the Raman spectrum for YBa<sub>2</sub>(Cu<sub>1-x</sub>Ni<sub>x</sub>)<sub>3</sub>O<sub>7-δ</sub> (x = 0.0064, δ = 0).

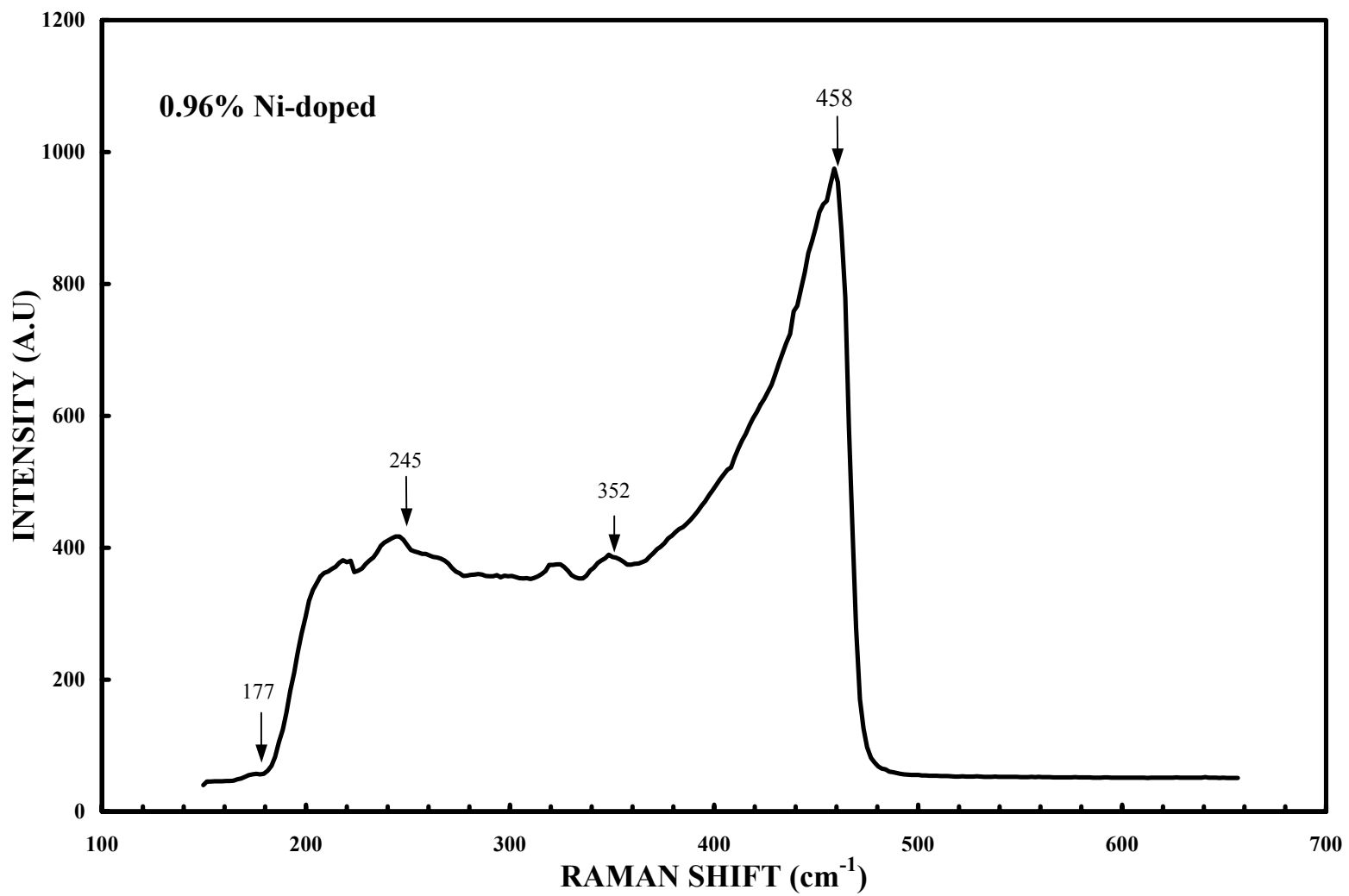


**FIGURE 4-5.** This is the Raman spectrum for YBa<sub>2</sub>(Cu<sub>1-x</sub>Ni<sub>x</sub>)<sub>3</sub>O<sub>7-δ</sub> (x = 0.0096, δ = 0).

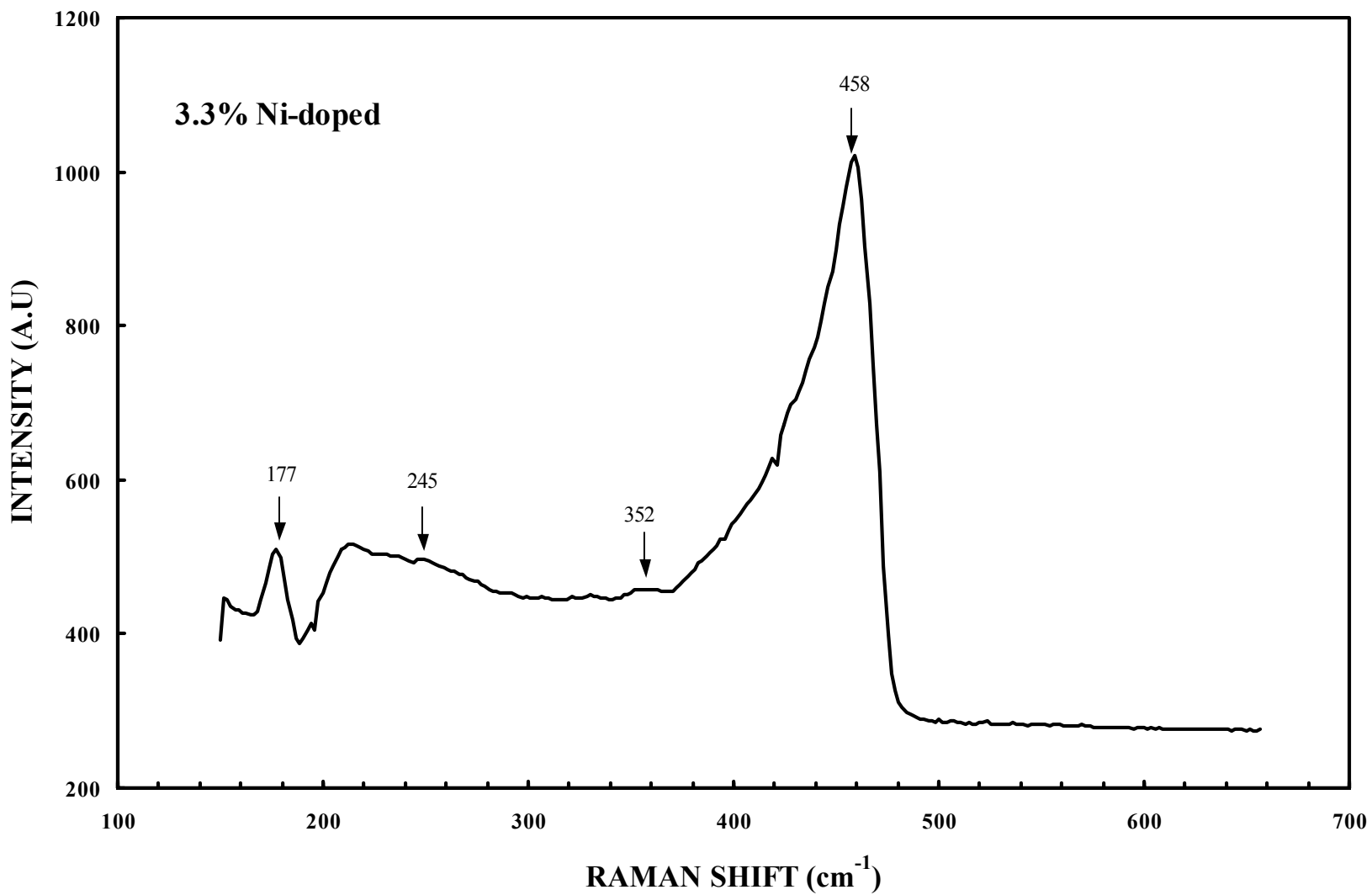


**FIGURE 4-6.** This is the Raman spectrum for YBa<sub>2</sub>(Cu<sub>1-x</sub>Ni<sub>x</sub>)<sub>2</sub>O<sub>7-δ</sub> (x = 0.033, δ = 0).

440  $\text{cm}^{-1}$ . The out-of-phase oxygen mode at 352  $\text{cm}^{-1}$  can also be clearly identified, again temperature corrected from the room temperature value<sup>42</sup> of 340  $\text{cm}^{-1}$ . Both of these peaks correspond to a distribution of oxygen vibration modes which are the O(2) and O(3) in the planes<sup>43</sup> as can be seen in Fig 4-1. Unfortunately, the vibrations involving the Cu-O chains in pure Y-123 cannot be observed by Raman scattering techniques since they have odd parity and are therefore only infrared-active.<sup>44</sup> However, under certain conditions which can destroy the symmetry of the Cu-O chains in the sample, they can again be made Raman-active, as previously shown in the literature for the case of oxygen deficiency<sup>45</sup> in the samples, and more specifically in the Cu-O chains themselves.

Fig. 4-3 shows the Raman spectra of  $\text{YBa}_2(\text{Cu}_{1-x}\text{Ni}_x)_3\text{O}_{7-\delta}$  with nickel doping ( $x = 0.0032$ ), which was the dopant level producing optimal critical state enhancement, at a temperature of 20 K, and with  $\delta$  approaching zero, as can be seen from the sharpness of the  $T_c$  and  $J_c$  transitions. Certainly, one can see the explicit contributions of nickel doping as compared to the pure Y-123 spectra. The Raman peaks at 460  $\text{cm}^{-1}$  and 350  $\text{cm}^{-1}$  are again the oxygen in-phase and out-of-phase modes associated with the  $\text{CuO}_2$  planes in the pure Y-123. Liu *et al*<sup>46</sup> and others experimentally observed these lines as well at 330 and 440  $\text{cm}^{-1}$ , when collecting spectra at room temperature. The theoretical and experimental work on the phonon frequencies and the eigenmodes have been published by a number of groups.<sup>47-49</sup> Specifically, at this first and lowest dopant level, the phonon at 350  $\text{cm}^{-1}$  now seems to decrease in intensity, comparatively, and enhanced new peaks, not seen in the pure Y-123 material, now appear with even the lowest level of Ni doping. Obviously, the peak at 245  $\text{cm}^{-1}$  can be identified as a vibrational mode associated with the Cu-O chain

vibration as clearly shown in Figs 4-3 and 4-4, but not seen in the pure Y-123 material. The reason for its appearance in the spectra of the doped samples stems from the breakdown of the chain symmetry via nickel substitution for the copper at locations randomly selected by the nickel atoms in the Cu-O chains. This peak assignment is also borne out in the literature.<sup>50</sup>

We also observed the appearance of a new peak at  $177\text{ cm}^{-1}$  at  $x = 0.0032$  that appeared for all values of  $x$ , the nickel dopant level. According to the theoretical and experimental analysis of the frequencies of Raman-active vibrational modes for YBCO as can be seen in Table 4, this peak is clearly not identified as any peak associated with YBCO. Yet it does correspond to the calculated peak for a Ni-O impurity, from Raman spectra tabulated in the literature for metal oxides<sup>51</sup>, lending credence to our belief that not all of the nickel incorporates into the structure, especially at the higher dopant levels. Rather, much of it shows up as a separate compound of Ni-O, most likely distributed throughout the sample at the grain boundaries. Furthermore, the peak at  $177\text{ cm}^{-1}$  is enhanced in its relative size as the amount of Ni increases. From our own calculations based on the literature,<sup>52,53</sup> this peak represents a Ni-O impurity mode of oscillation.

Because there were only negligible shifts in the vibrational modes at the higher  $x$ -values from the lower  $x$ -values, we can conclude that little Ni probably incorporated into the structure at the Cu sites. This becomes even more apparent at  $x = 0.033$ , as shown in Fig. 4-6, where this new Ni-O peak is strongly rising above the background, and likely large amounts of the doped nickel are located at the grain boundaries as a Ni-O impurity. With nickel breaking the symmetry at the chain sites, the chain modes of oscillation do indeed appear in all of the doped samples. Additionally, in most cases in the literature,

**TABLE 4.** These are the experimental and calculated frequencies of Raman-active modes for YBCO below  $T_c$ .

Assignment	A <sub>g</sub>			B <sub>2g</sub>			B <sub>3g</sub>		
	Exp.*	TEC**	LDC***	Exp.	TEC	LDC	Exp.	TEC	LDC
Ba	112	116	116	70	70	73	83	72	92
Cu	154	157	157	142	142	142	140	133	137
O out of phase	340	364	355	579	568	564	526	524	544
O in Phase	440	411	378	--	365	429	303	335	412
Bridging Oxygen	500	495	508	210	185	356	--	257	496

\* Experimental Data : D.R. McCarty, J.Z. Liu, R.N. Shelton and H.B. RaDousky, Phys. Rev. B **41**, 8792(1990).

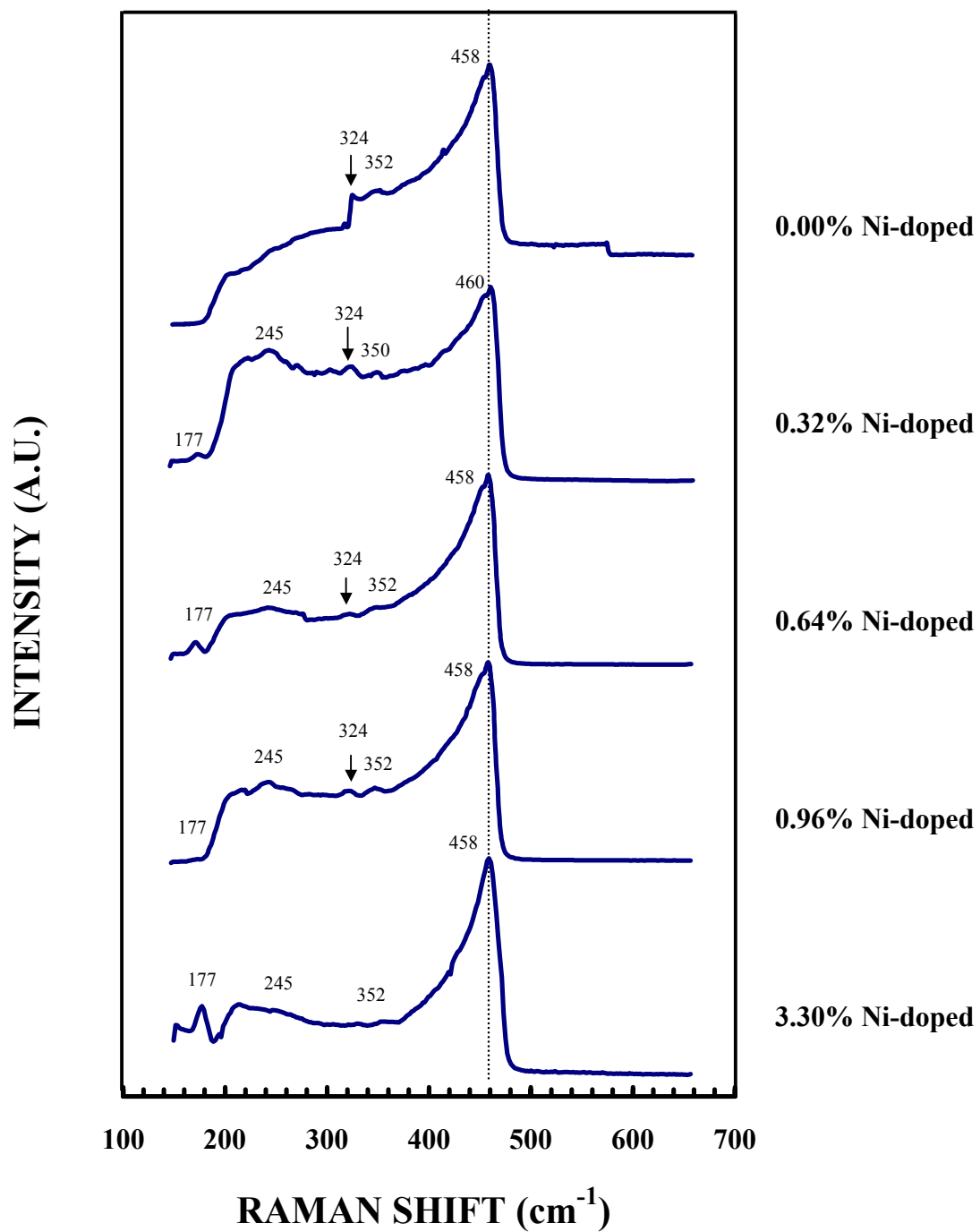
\*\* The results of total-energy calculation (TEC) : R.E. Cohen, W.E. Pickett and H. Krakauer, Phys. Rev. Lett. **64**, 25751 (1990).

\*\*\* The Lattice-Dynamical Calculations (LDC) : W. Kress, U. Schroder, J. prade, A.D. Kulkarni and F.W. de Wette, Phys. Rev. B **38**, 2906(1988).

there has been controversy about Raman features with frequencies less than  $200\text{ cm}^{-1}$ , primarily due to the difficulty of obtaining signals in such close proximity to the laser line frequency. However, in our case, this spectral peak clearly appears only after Ni doping has taken place, lending credence to our belief that this is indeed a Ni-O phonon mode. It can be clearly noted that the  $x = 0.0032$  Ni substituted sample has a Cu-O chain mode of oscillation that is larger in relative size than any of the other spectra. This would indicate that when nickel is first doped into the YBCO structure, that it at first preferentially substitutes into the chain sites, but that additional nickel doping simply results in increasing the amounts of Ni-O compound forming at the grain boundaries, and thus overshadowing the Cu-O chain substitutions that would have resulted in an enhancement of the superconducting in-field critical state current density, due to the ferromagnetic ordering of these chains. However, large amounts of Ni-O forming at the grain boundaries obviously cause a rapid degradation of the superconducting properties as the nickel doping level increases.

By comparison of all of the Raman spectra as shown in Fig. 4-7, the phonon peaks at  $460\text{ cm}^{-1}$  and at  $350\text{ cm}^{-1}$  for  $x = 0.0032$  are observed to occur within  $\pm 2\text{ cm}^{-1}$  of their position in all of the other samples, both in the doped samples and in the control sample, whose plane modes are observed at  $458\text{ cm}^{-1}$  and  $352\text{ cm}^{-1}$ . We can therefore assume that the substitution of nickel in  $\text{YBa}_2\text{Cu}_3\text{O}_{7-\delta}$  has little or no effect on the plane modes of oscillation according to the Raman spectra obtained in our experiments, and thus that the nickel substitutes for copper preferentially in the chain sites rather than in the plane sites.

**FIGURE 4-7.** These are the Raman spectra for  $\text{YBa}_2(\text{Cu}_{1-x}\text{Ni}_x)_3\text{O}_{7-\delta}$  at different concentrations  $x$  (at. %).





In the analysis of all of the Raman spectra obtained in our experiment, it is difficult to determine the location of the phonon peaks with a high degree of precision because the spectroscopic data may have distorted shoulder peaks and hidden peaks, as well as a fairly large noise threshold. Therefore, in all of the spectra, the labeled phonon peaks have been analyzed using the Lorentzian peak-fitting function to produce a precision-fit to the spectral data. Equation 4-1 shows the general Lorentzian functional form that was applied to the analyses of all of our Raman spectral data collected.

$$I(\nu) = \frac{H}{4\left(\frac{\omega - \omega_0}{W}\right)^2 + 1} \quad (4-1)$$

In this formula,  $I(\nu)$  refers to the intensity,  $H$  to the height,  $\omega$  to any position we would associate with the formation of the peak including its surrounding region,  $\omega_0$  the position of the peak center which is labeled in our graphs and determined from the curve fit, and  $W$  the Full Width at Half Maximum (FWHM) of the peak. By varying the parameters of this expression, we can utilize an Excel spreadsheet to apply the Raman spectra curve-fitting routine in all of the plots of  $\omega$  versus intensity. In the vicinity of all labeled phonon peaks, we have successfully used the Lorentzian function to uniquely determine the central positions of all labeled peaks.

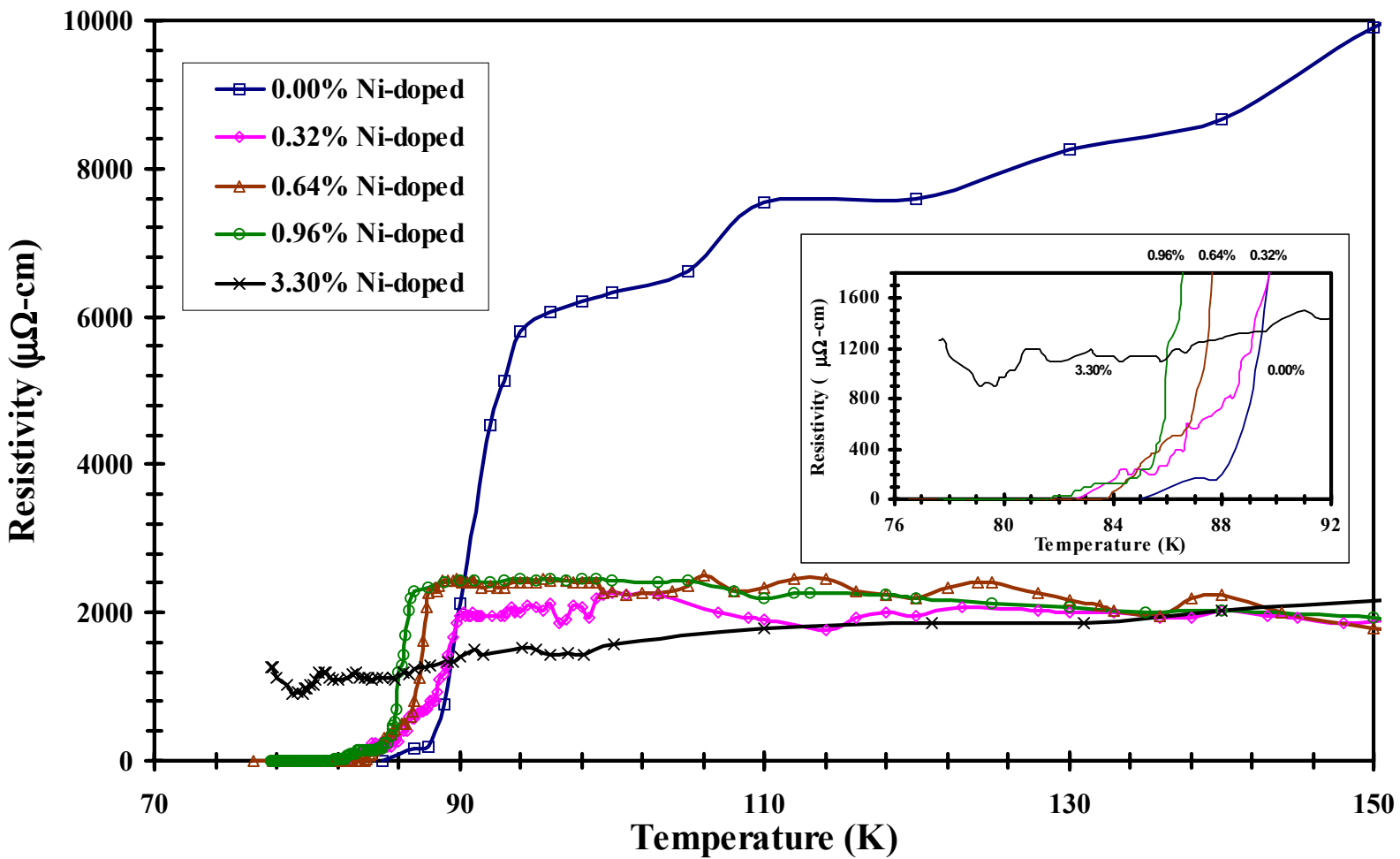
In addition, by comparison of the doped samples to the control sample in Fig. 4-7, we can recognize the broadening of the phonon mode at  $324 \text{ cm}^{-1}$  as the dopant level increases and its eventual disappearance as the nickel doping level reaches the highest level of  $x = 0.033$ . This clearly indicates that the presence of Ni-doping has significantly deteriorated this phonon vibrational mode, due to the grain boundary contamination of NiO.

## 4-2. Discussion of the Critical Temperature ( $T_c$ ) Dependence on Nickel Doping

We measured the resistivity of the control sample,  $\text{YBa}_2\text{Cu}_3\text{O}_{7-\delta}$ , and of the nickel substituted  $\text{YBa}_2(\text{Cu}_{1-x}\text{Ni}_x)_3\text{O}_{7-\delta}$  samples, as a function of temperature to determine their critical temperatures,  $T_c$ . We used a carbon-glass resistor at the sample position to measure the sample temperature, and we used a conventional four probe technique to measure the sample resistivity. In order to better understand the different  $J_c$  values measured in all of the nickel-doped samples, the critical temperature,  $T_c$ , needed to be determined with certainty for each of the samples. The critical temperature as determined from the resistivity midpoint is at a comparable temperature to that obtained from a magnetic susceptibility midpoint temperature determination.<sup>54</sup> We also measured the critical temperature of the pure (control) sample,  $\text{YBa}_2\text{Cu}_3\text{O}_{7-\delta}$ , to ensure its quality as the control sample for the experiment.

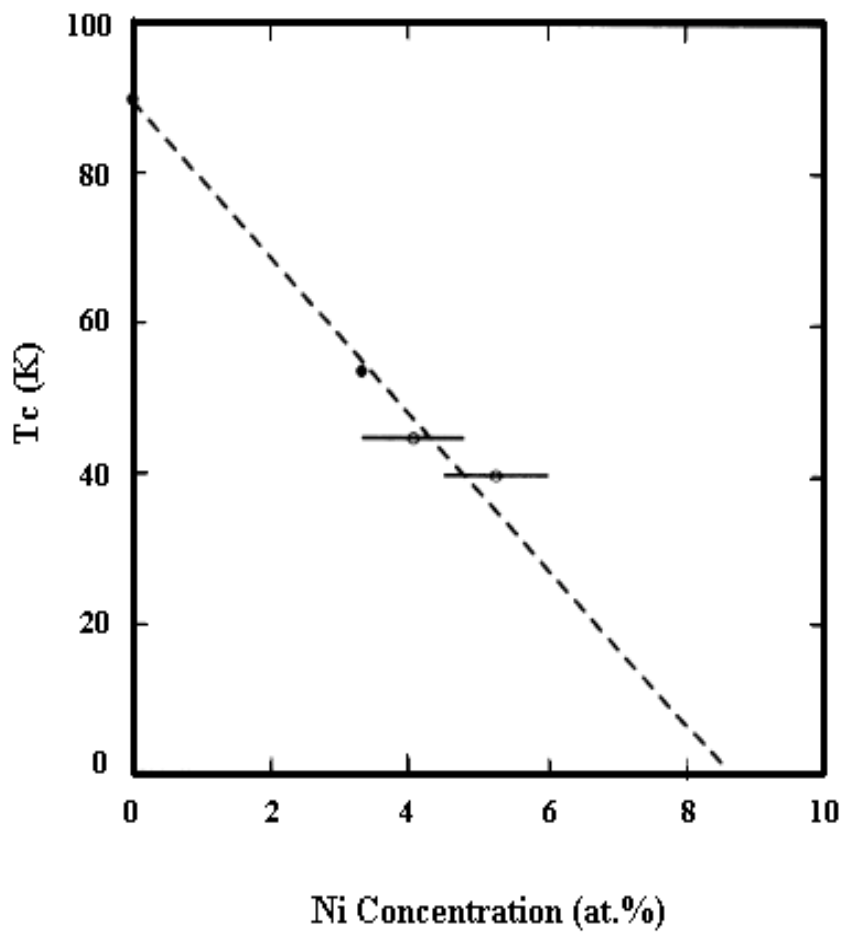
Figure 4-8 depicts the temperature dependence of the resistivity for all of the samples. The transition width is observed to be around 4 K for all of the doped samples and less than 2 K for the undoped control sample. More specifically, the transition width is 2.0 K (91 K – 89 K), for  $x = 0.0$ , 4.0 K (88 K – 84 K) for  $x = 0.0032$ , 4.2 K (88 K – 83.8 K) for  $x = 0.0064$ , and 4.3 K (86 K – 81.7 K) for  $x = 0.0096$ . These results show that the critical temperature is depressed by the nickel doping of the samples. This result is also in agreement with the literature<sup>55,56</sup> as can be seen in Fig. 4-9. The resistivity in the high temperature ( $90 \text{ K} \leq T \leq 150 \text{ K}$ ) region is linear. This linearity has been linked to the two-dimensional character of the electron transport.<sup>57</sup>

Fig. 4-10 shows the temperature dependence of the resistivity for the control sample. The critical temperature was 91 K with the transition width less than 2.0 K. The



**FIGURE 4-8.** This is the temperature dependence of resistivity for  $\text{YBa}_2(\text{Cu}_{1-x}\text{Ni}_x)_3\text{O}_{7-\delta}$  ( $\delta = 0$ ), with all doping levels tested.

**FIGURE 4-9.** This shows the superconducting transition temperature,  $T_c$ , as a function of the Ni concentration in Y-B-Cu-O( $Ni_x$ ) using the corrected Ni concentrations.<sup>58</sup> [By F. Bridges *et al.*]



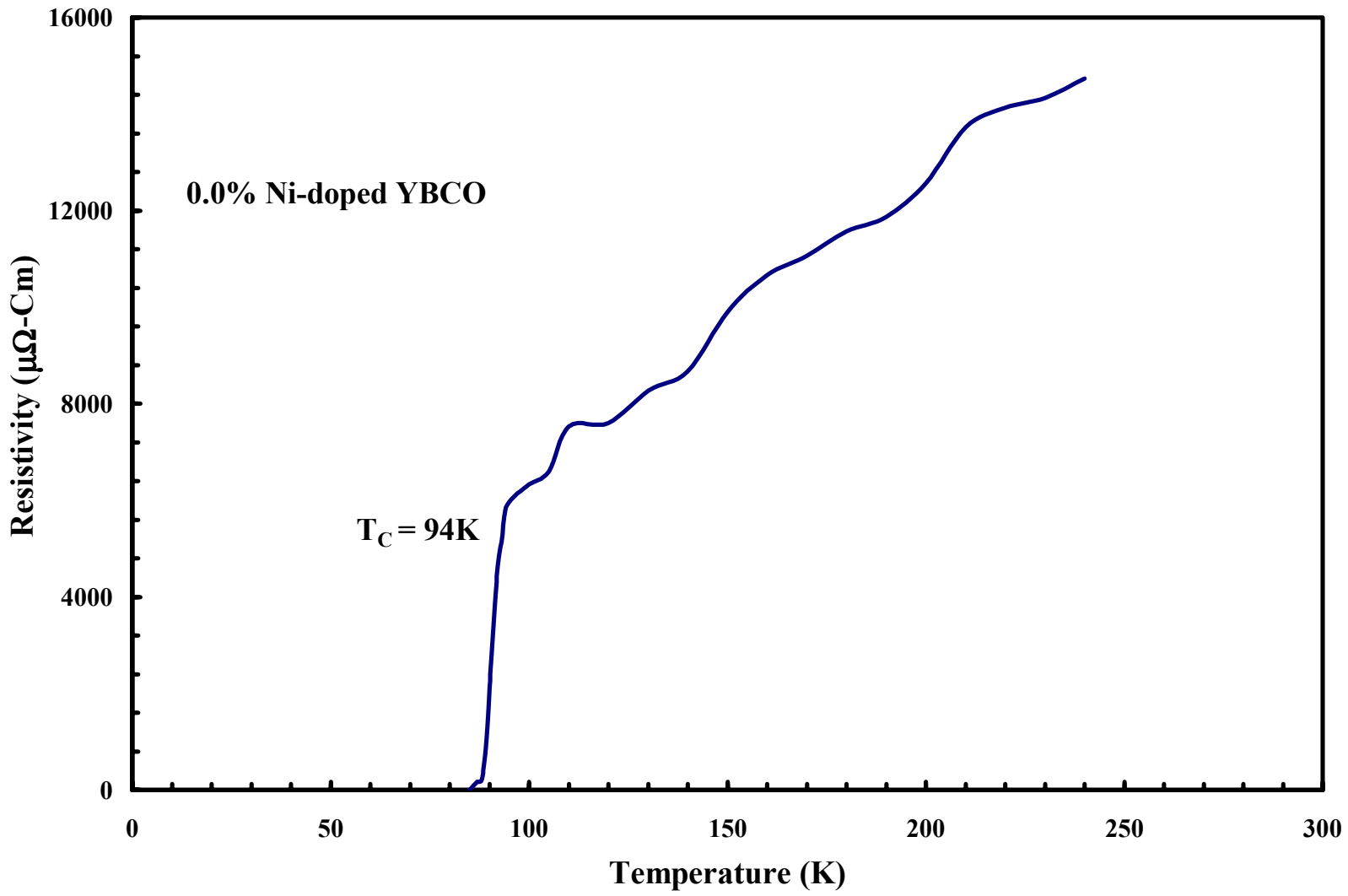


**FIGURE 4-10.** This is the resistivity versus temperature curve for undoped  $\text{YBa}_2\text{Cu}_3\text{O}_{7-\delta}$  ( $\delta = 0$ ).

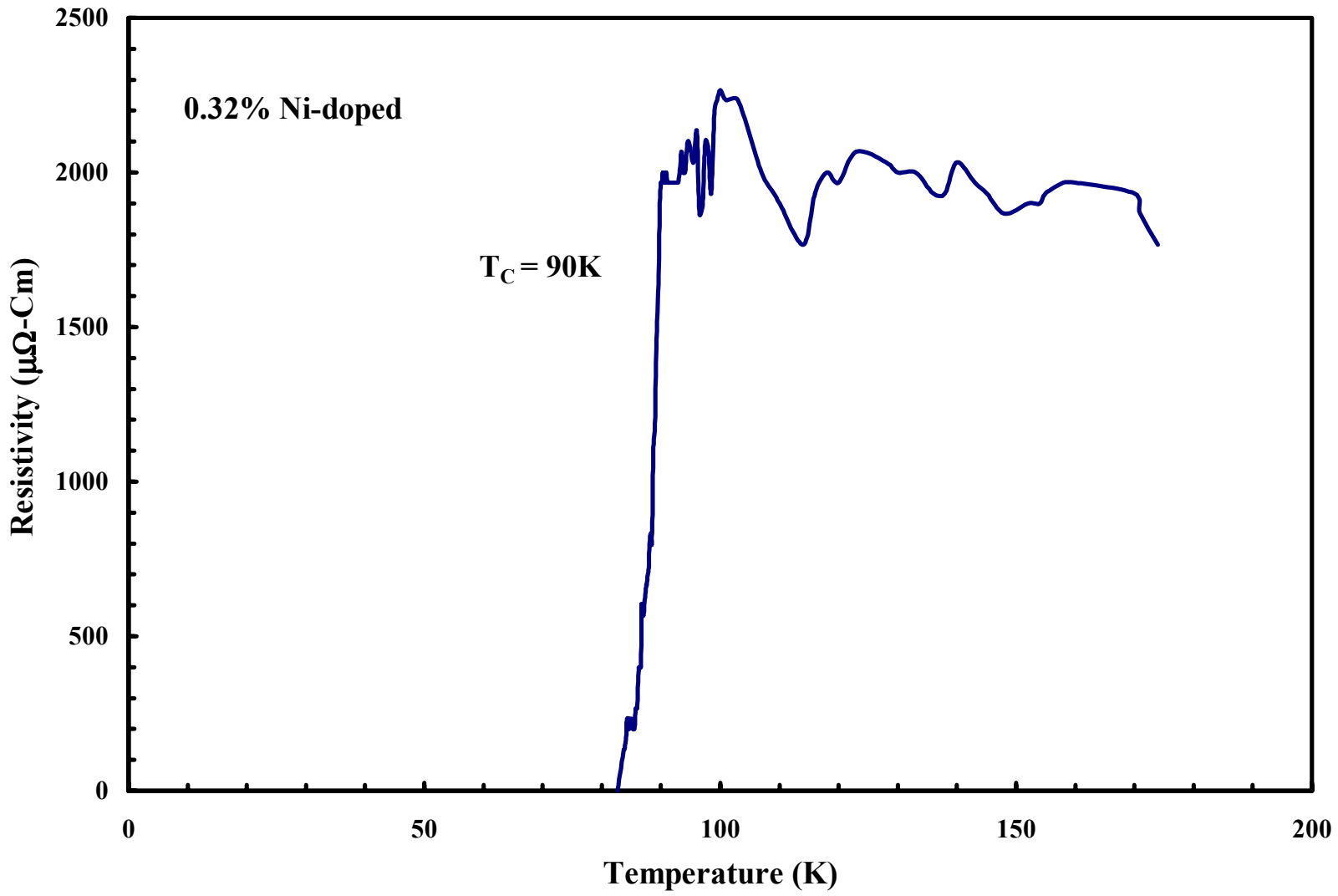
smoothness of the normal state resistivity, indicative of high sample quality and purity, should be noted.

Fig. 4-11 represents the temperature dependence of resistivity for the nickel doped sample with  $x = 0.0032$  ( $\text{YBa}_2[\text{Cu}_{0.9968}\text{Ni}_{0.0032}]_3\text{O}_7$ ), whose critical temperature was 90 K with a transition width less than 4.0 K. The normal state of this sample is ohmic. The jaggedness of the sample's normal state resistivity is already indicative of reduced sample quality due to impurity phases and of voltage fluctuations due to increasing grain boundary contamination of NiO.

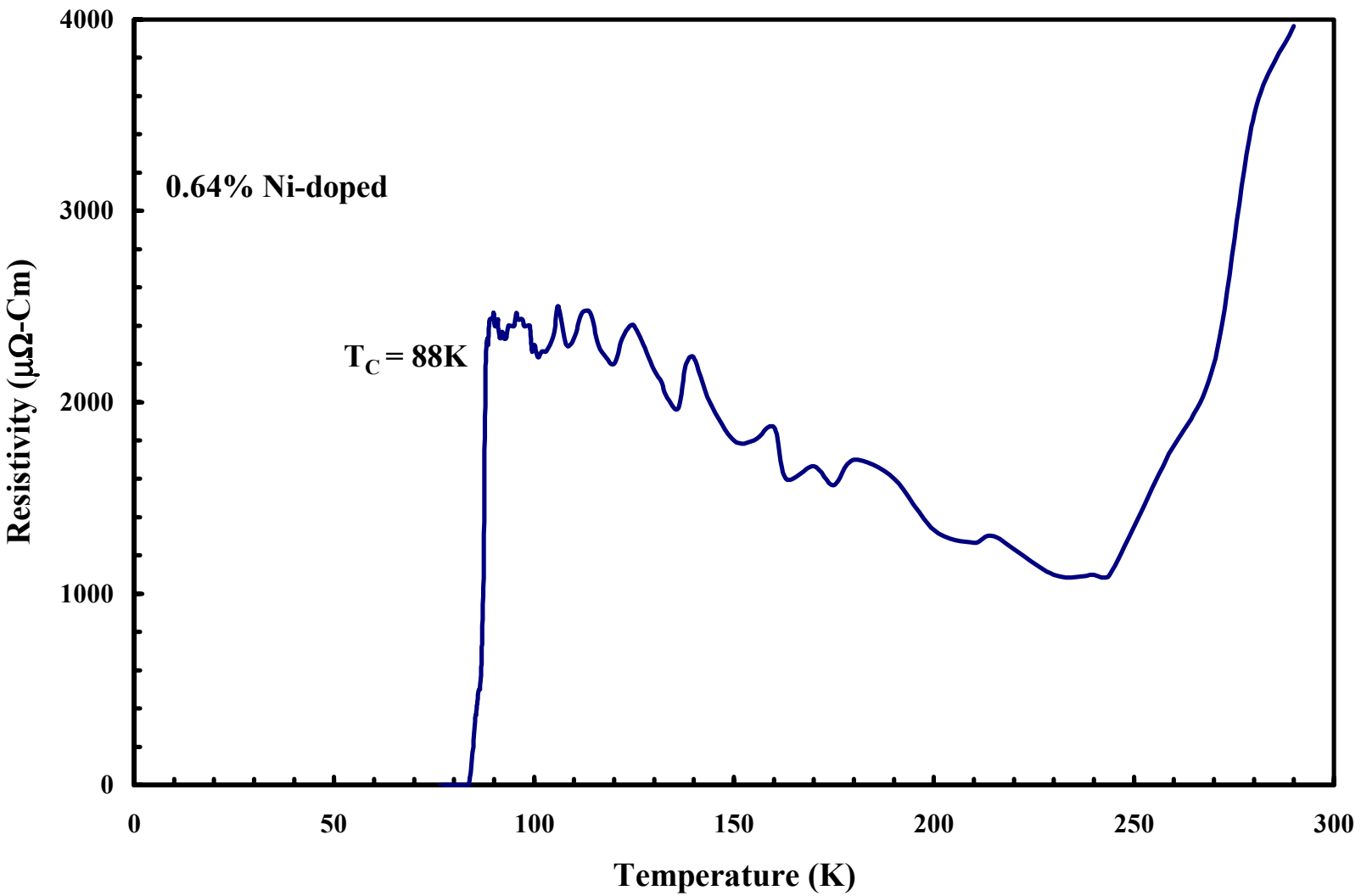
Fig. 4-12 exhibits the temperature dependence of resistivity for the nickel doped sample with  $x = 0.0064$  ( $\text{YBa}_2[\text{Cu}_{0.9936}\text{Ni}_{0.0064}]_3\text{O}_7$ ). The critical temperature was 88 K with the transition width less than 4.2 K.

Fig. 4-13 exhibits the temperature dependence of resistivity for the nickel doped sample with  $x = 0.0096$  ( $\text{YBa}_2[\text{Cu}_{0.9904}\text{Ni}_{0.0096}]_3\text{O}_7$ ). The transition width, with an onset critical temperature of 86 K, was less than 4.3 K.

In Fig. 4-14, the critical temperature onset was not as readily apparent as for the other samples. Although the sample showed a partial transition around 82 K, the resistivity below 80 K held almost steady at a low value due to the extent of the contamination of NiO at the grain boundaries at this highest dopant level.



**FIGURE 4-11.** This is the resistivity versus temperature curve for  $\text{YBa}_2(\text{Cu}_{1-x}\text{Ni}_x)_3\text{O}_{7-\delta}$  ( $x = 0.0032, \delta = 0$ ).



**FIGURE 4-12.** This is the resistivity versus temperature curve for YBa<sub>2</sub>(Cu<sub>1-x</sub>Ni<sub>x</sub>)<sub>3</sub>O<sub>7-δ</sub> (x = 0.0064, δ=0).



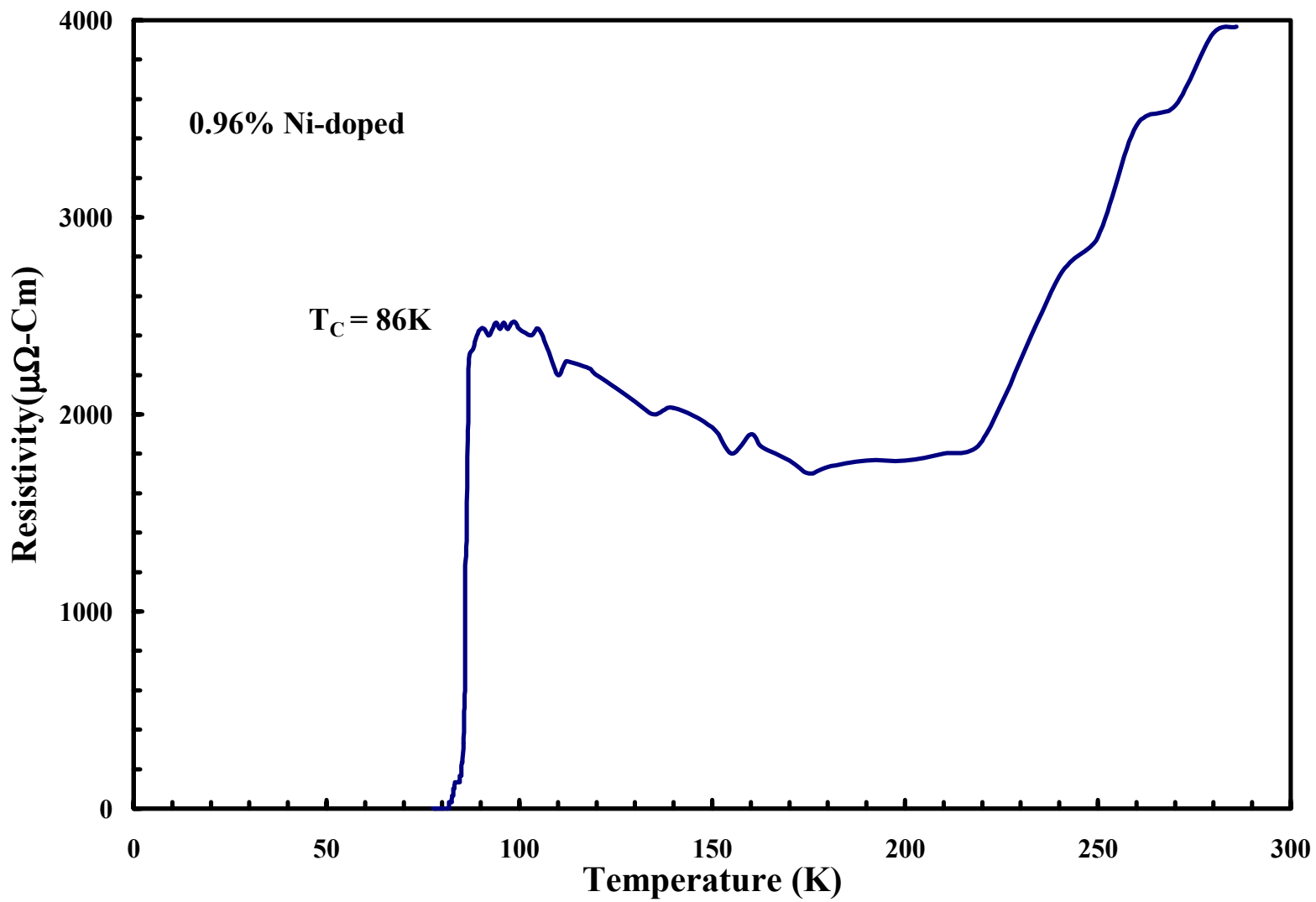


**FIGURE 4-13.** This is the resistivity versus temperature curve for YBa<sub>2</sub>(Cu<sub>1-x</sub>Ni<sub>x</sub>)<sub>3</sub>O<sub>7-δ</sub> (x = 0.0096, δ=0).

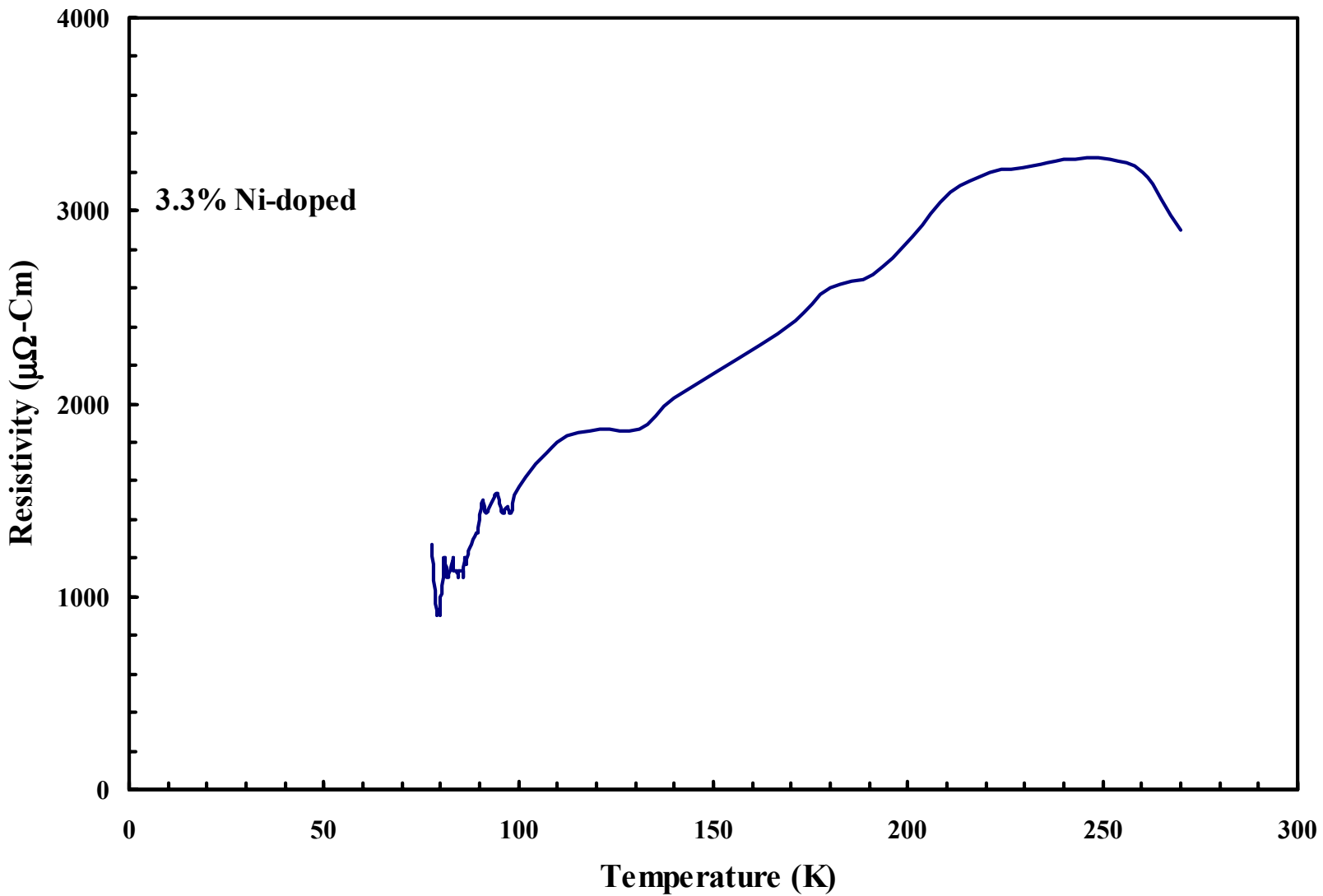
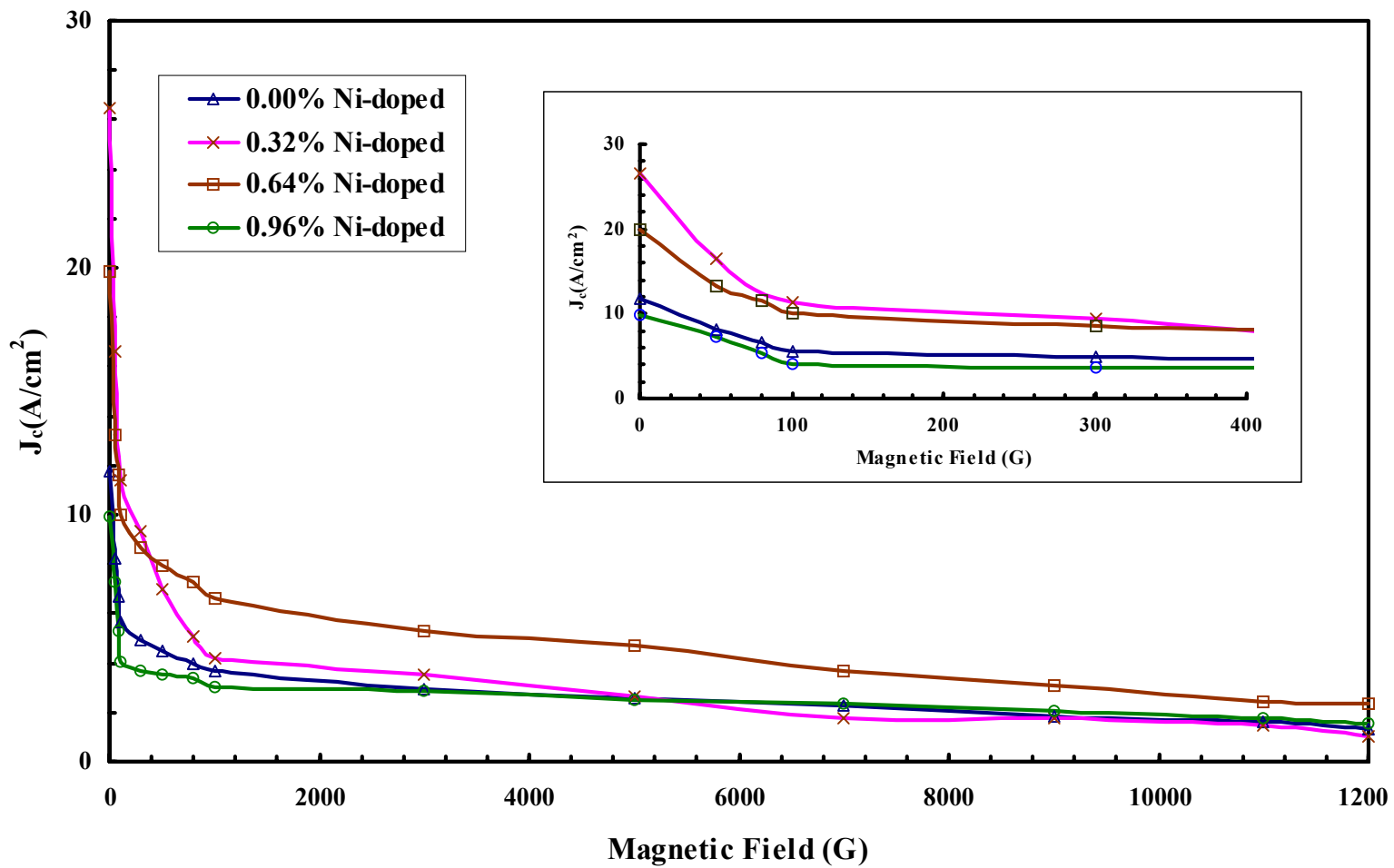


**FIGURE 4-14.** This is the resistivity versus temperature curve for  $\text{YBa}_2(\text{Cu}_{1-x}\text{Ni}_x)_3\text{O}_{7-\delta}$  ( $x = 0.033, \delta = 0$ ).

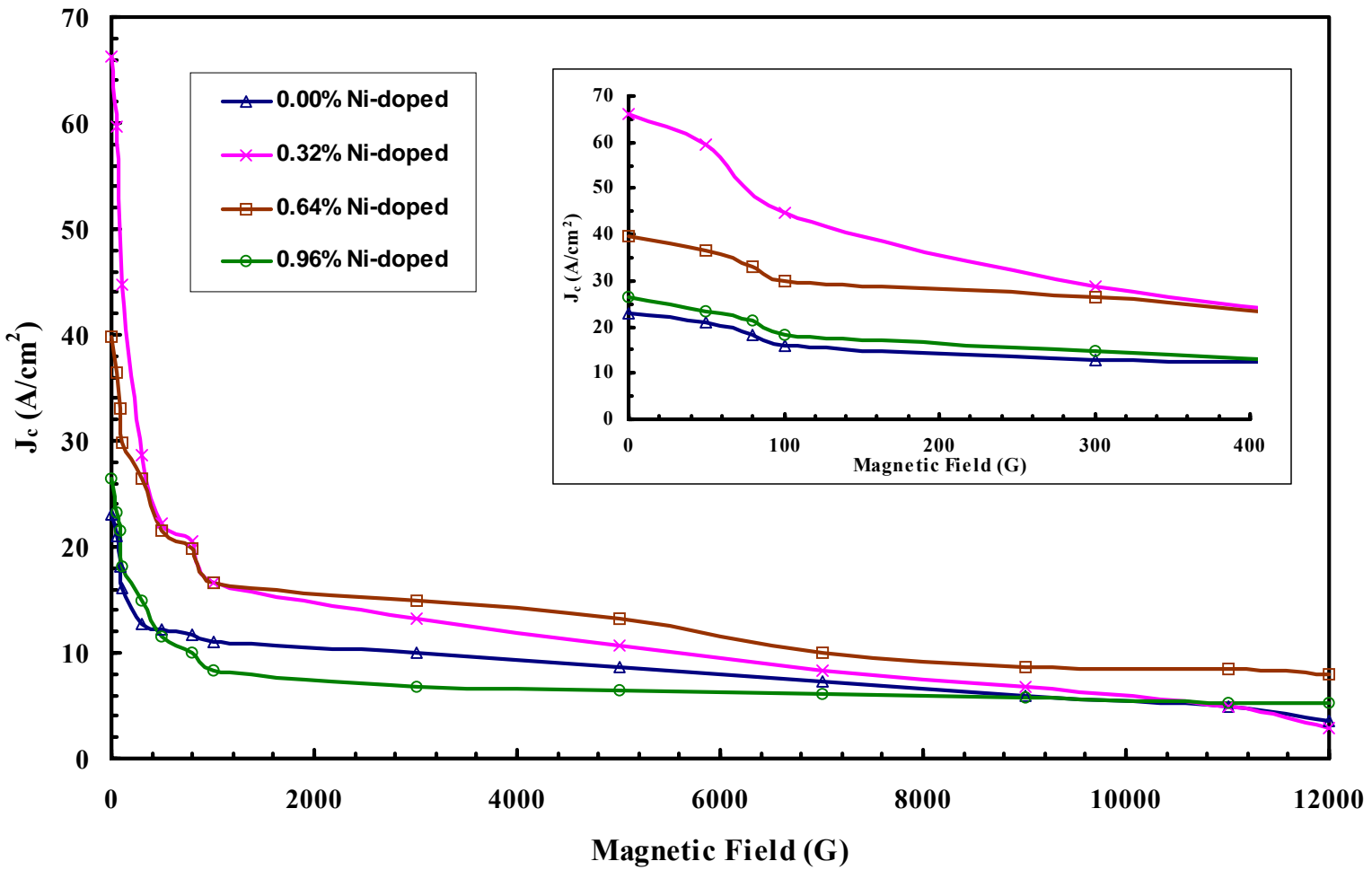
### 4-3. Discussion of the Critical Current Density ( $J_c$ ) Dependence on Nickel Doping

Next, we turn to the discussion of the results of our critical current measurements for  $\text{YBa}_2(\text{Cu}_{1-x}\text{Ni}_x)_3\text{O}_{7-\delta}$ . The values of  $J_c$  can be determined directly by the four point probe method as discussed in the earlier section. A large enhancement of  $J_c$  has been observed at the  $x = 0.0032$  level at 77 K in the lower range of magnetic field values as can be seen in the inset of Fig. 4-15 after comparison to the undoped sample ( $x = 0$ ). However, the critical current density of the 0.32 % doped sample deteriorated below the control sample for higher magnetic field values. On the contrary, the sample with  $x = 0.0064$  predominates in the higher magnetic field values at 77 K. This figure also shows that the higher doped sample ( $x = 0.0096$ ) has a lower  $J_c$  than the control sample at both lower and higher magnetic fields. At 60 K, the prominent enhancement of  $J_c$  was also observed in the lower range of magnetic field values at the  $x = 0.32$  % Ni dopant level. In this case, all samples in the low magnetic field values show an enhancement when compared to the control sample, as can be seen in Fig. 4-16. On the other hand, the sample at  $x = 0.0064$  was superior to the others in the higher magnetic field. The higher doped sample ( $x = 0.0096$ ) deteriorated in the higher magnetic fields in the same manner as at 77 K, and had lower critical current values than even the undoped sample.

As the samples are cooled down through the transition temperature  $T_c$ , the critical current value, theoretically, would be expected to gradually increase to its maximum value when the sample reached 0 K. Figs. 4-17, 18, 19, and 20 are measured at the sample temperatures of 77 K and 60 K. According to our results, the critical current density at 60 K is clearly higher than that at 77 K for all of the Ni-doped samples. As can

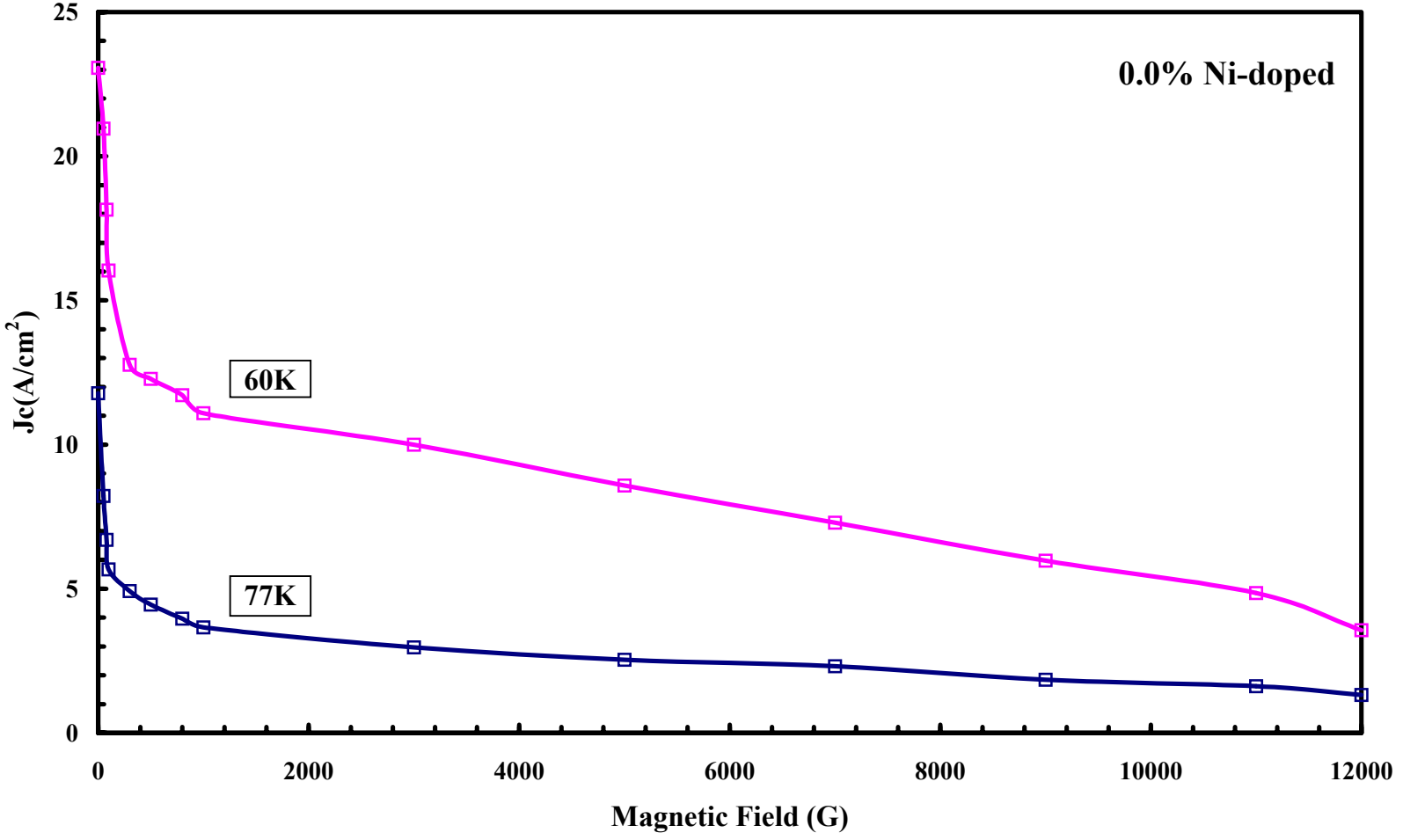


**FIGURE 4-15.** This is the critical current density versus magnetic field for YBa<sub>2</sub>(Cu<sub>1-x</sub>Ni<sub>x</sub>)<sub>3</sub>O<sub>7-δ</sub> ( $\delta=0$ ) at 77K for all doping levels tested and the control sample.

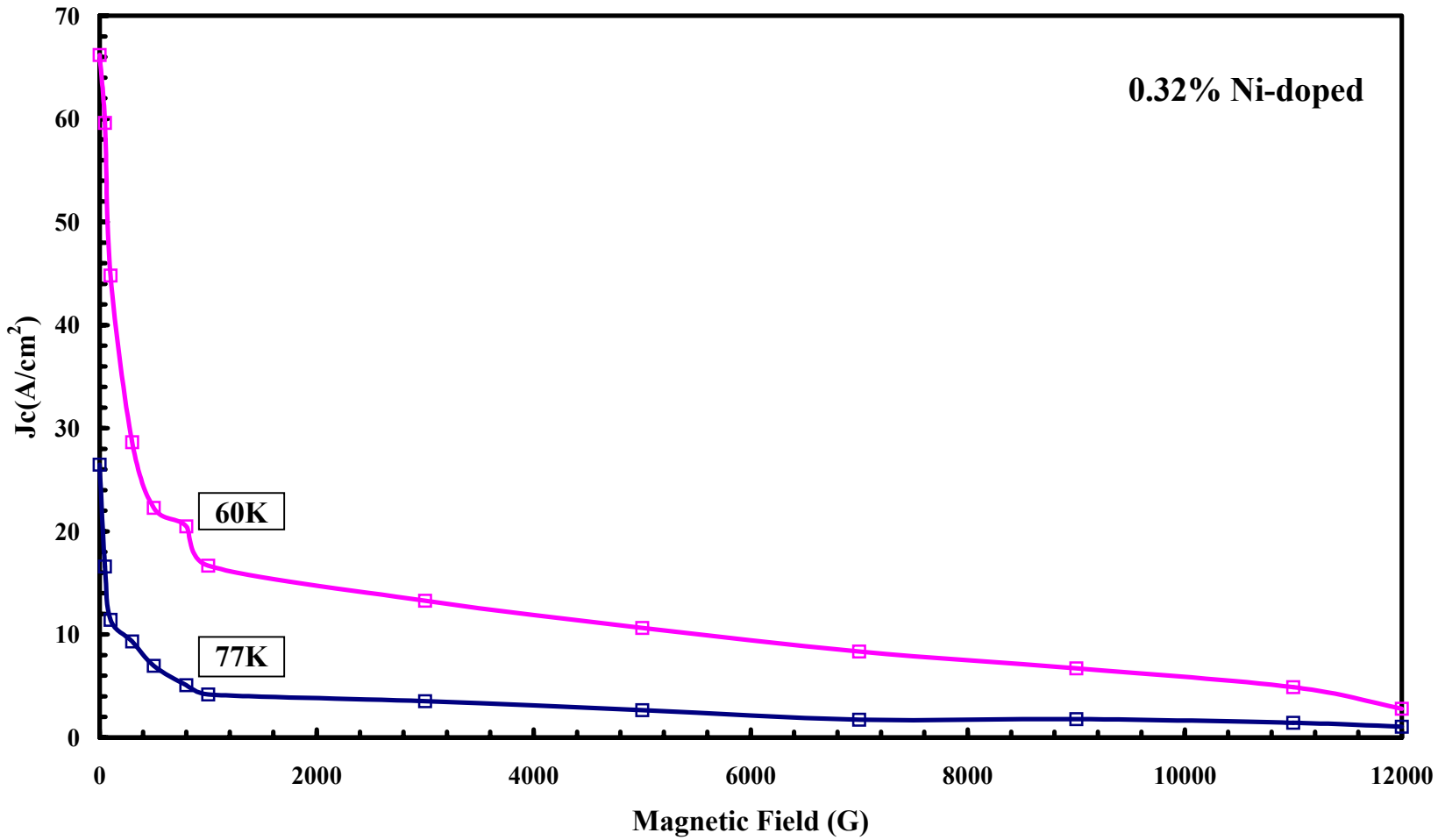


**FIGURE 4-16.** This is the critical current density versus magnetic field for  $YBa_2(Cu_{1-x}Ni_x)_3O_{7-\delta}$  ( $\delta=0$ ) at 60K for all doping levels tested and the control sample.

**FIGURE 4-17.** This is the critical current density versus magnetic field for  $\text{YBa}_2\text{Cu}_3\text{O}_{7-\delta}$  ( $\delta=0$ ).



**FIGURE 4-18.** This is the critical current density versus magnetic field for  $\text{YBa}_2(\text{Cu}_{1-x}\text{Ni}_x)_3\text{O}_{7-\delta}$  ( $x = 0.0032$ ,  $\delta=0$ ).



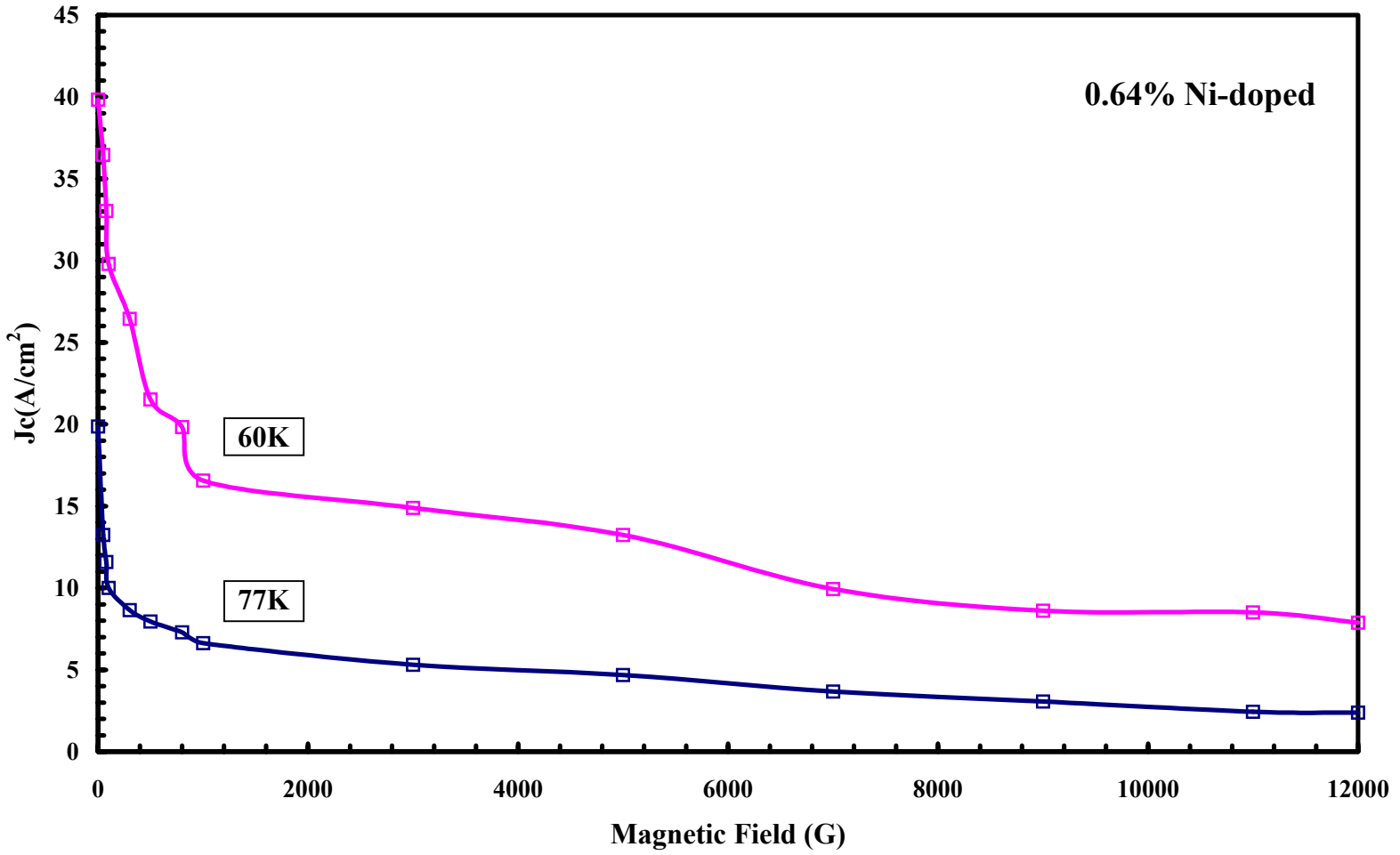


**FIGURE 4-19.** This is the critical current density versus magnetic field for  $\text{YBa}_2(\text{Cu}_{1-x}\text{Ni}_x)_3\text{O}_{7-\delta}$  ( $x = 0.0064$ ,  $\delta=0$ ).



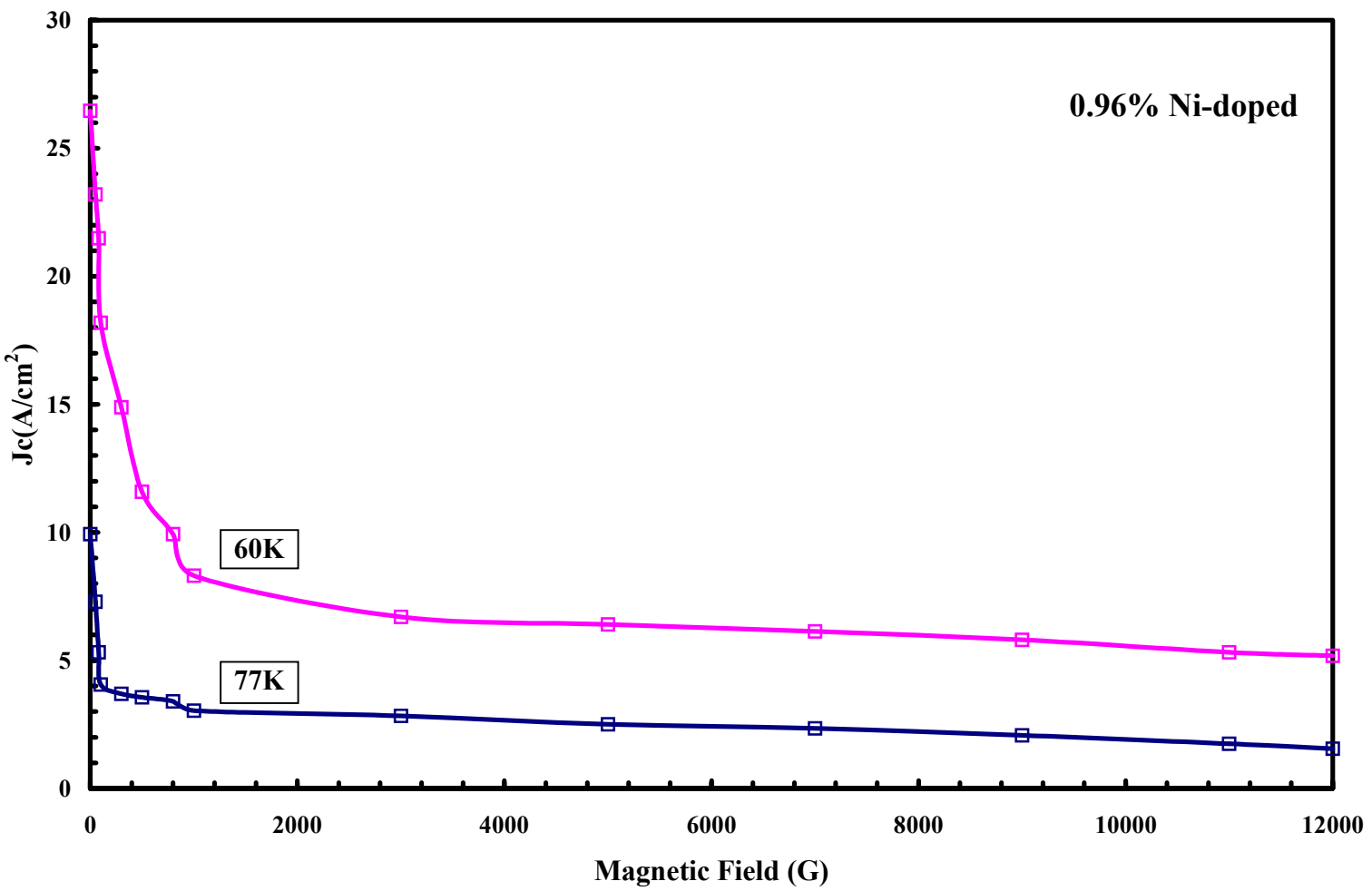


**FIGURE 4-20.** This is the critical current density versus magnetic field for  $\text{YBa}_2(\text{Cu}_{1-x}\text{Ni}_x)_3\text{O}_{7-\delta}$  ( $x = 0.0096$ ,  $\delta=0$ ).

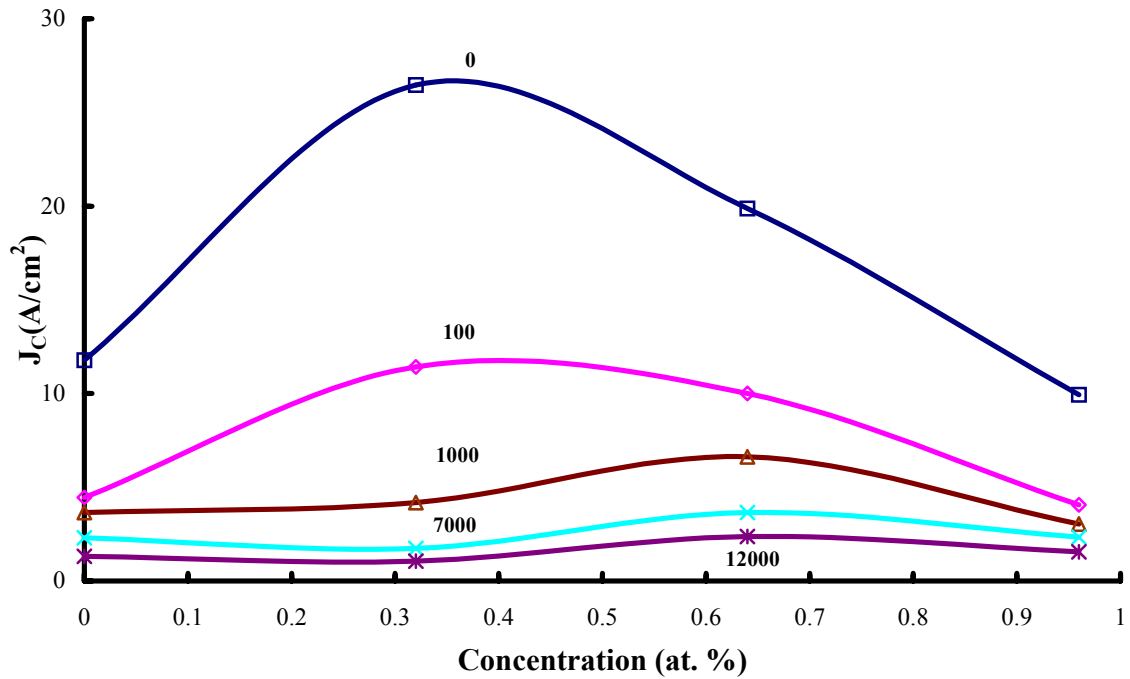
also be seen in Fig. 4-18, the critical current density exhibits the highest values at 60 K in the  $x = 0.0032$  sample, when it is compared to the other dopant levels.

We collected the data for five magnetic field values located at the points of most dramatic change in each plot, and organized this data. Table 5 shows critical current density ( $J_c$ ) values and corresponding values of the applied magnetic fields due to nickel doping ( $x = 0.0\%$ ,  $x = 0.32\%$ ,  $x = 0.64\%$ , and  $x = 0.96\%$ ) at both the temperatures of 77 K and 60 K. Also, Fig. 4-21 illustrates the magnetic field dependence of  $J_c$  due to concentration  $x$  based on the results tabulated in Table 5. We can readily recognize that the critical current density drastically decreases due to the applied magnetic field, and that it also decreases with the nickel concentration  $x$  after surpassing the lowest level of concentration. And we can expect from these results that still higher levels of nickel doping in the  $\text{YBa}_2\text{Cu}_3\text{O}_{7-\delta}$  system would only serve to further deteriorate the critical current density values.

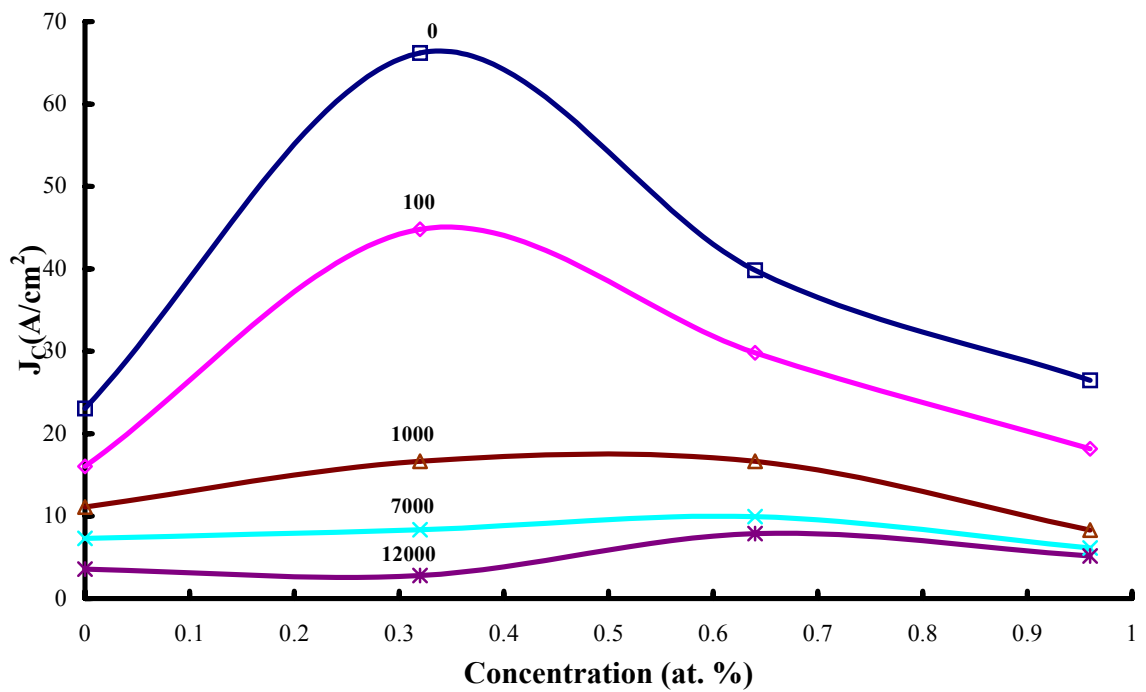
**TABLE 5.** This shows critical current densities with their corresponding measurement temperatures and their values of the externally applied magnetic fields at the different levels of nickel doping used in our samples.  
[Here,  $\delta = 0$  for  $\text{YBa}_2(\text{Cu}_{1-x}\text{Ni}_x)_3\text{O}_{7-\delta}$  ]

Concentration X	$J_c$ at 77 K					$J_c$ at 60 K				
	Magnetic Fields <b>B</b> (Gauss)					Magnetic Fields <b>B</b> (Gauss)				
	0	100	1000	7000	12000	0	100	1000	7000	12000
x = 0.0000	11.78	4.46	3.66	2.31	1.32	23.07	16.04	11.09	7.29	3.56
x = 0.0032	26.47	11.42	4.19	1.75	1.06	66.20	44.81	16.67	8.35	2.81
x = 0.0064	19.87	10.00	6.63	3.66	2.38	39.83	29.80	16.57	9.93	7.89
x = 0.0096	9.93	4.06	3.04	2.34	1.55	26.47	18.18	8.32	6.14	5.18

**FIGURE 4-21.** This depicts the variation of the magnetic field dependence of  $J_c$  due to concentration  $x$ .



(a) The in-field decrease of  $J_c$  is shown at 77 K.



(b) The in-field decrease of  $J_c$  is shown at 60 K.

#### 4-4. Discussion of Extended X-ray Absorption Fine Structure (EXAFS)

The purpose of the raw reference sample was to see if the Ni was substituted into the  $\text{YBa}_2\text{Cu}_3\text{O}_{7-\delta}$ , or if it remained as a NiO impurity. If the situation is the latter, then the distance peaks in all four Fourier transforms should be the same within a degree of error. The pre-edge background has to be subtracted since we are only interested in the data above the edge. The EXAFS data are then normalized to a data point close to the edge ( $\mu_0$ ) in k-space, which defines the beginning to the EXAFS with  $k = 0$ . The small peaks that precede the first large dominant peak in the experimental results are simply artificial results from noise in the experiment, since it is not possible to have atoms at such a small distance in this material. The distances for the peaks were found using WinXAS 97v1.3, in order to locate the minima and maxima of the plots and then to match them to the graphs. There are five peaks of the NiO reference sample as depicted in Fig. 4-22, with the distances grouped together for comparison. The EXAFS spectra for the three samples are displayed in Fig. 4-23. According to the results as shown in Table 6 for dominant peak distances in the samples, the Ni does indeed appear as an impurity in the form of NiO in the Ni-doped  $\text{YBa}_2\text{Cu}_3\text{O}_{7-\delta}$  samples, but only to a certain extent. A definite correlation with some NiO peak distances can be observed, but some peaks are also noticeably absent in our samples. The heights of the peaks in each graph are included as well in parentheses. Clearly the second atomic shell in our experimental samples would appear to be in correlation with the second atomic shell of a pure NiO sample, based on the close relationship between the distances in the 2<sup>nd</sup> peak column. However, the 2<sup>nd</sup> peak heights as related to the 1<sup>st</sup> peak heights in all of the experimental samples suggest that more of the Ni is incorporated into the superconductor than is appearing as an

**FIGURE 4-22.** This is the Fourier transform of a reference NiO sample from a standard EXAFS experiment.

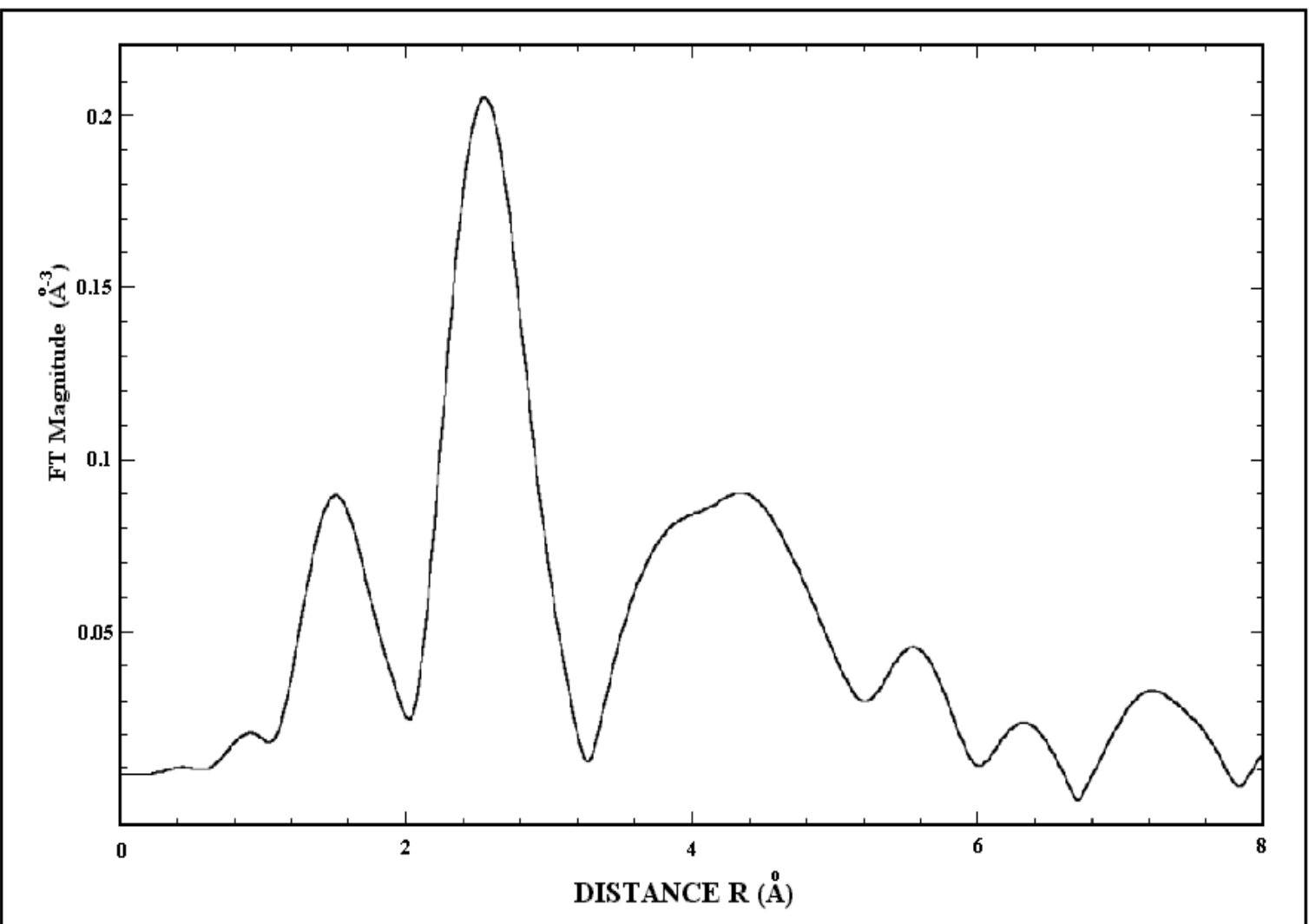


**FIGURE 4-23.** These are the Fourier transforms for the three low Ni-doped samples measured by EXAFS.

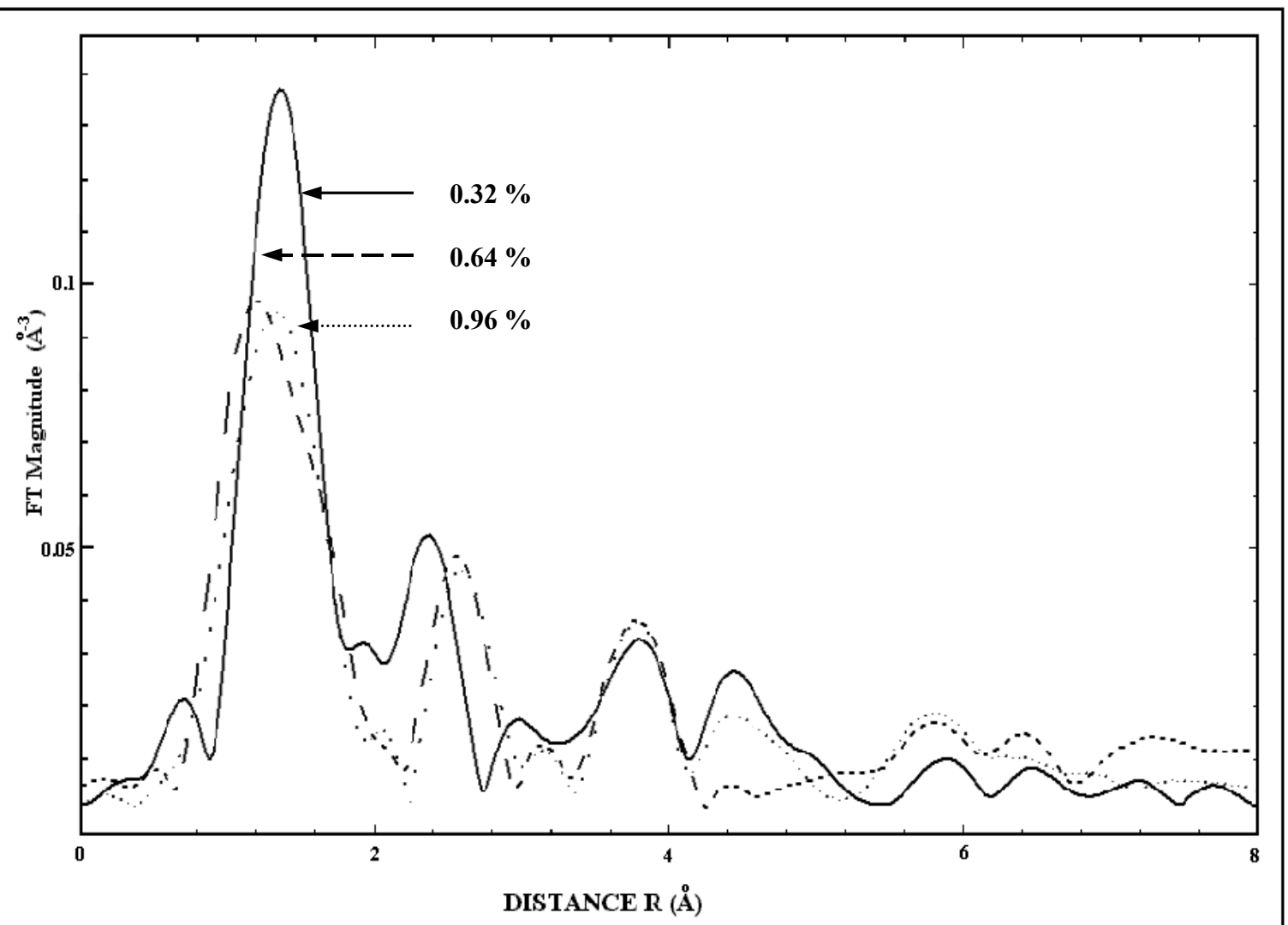


**TABLE 6.** These are the dominant peak distances from the Fourier transforms of the Ni-doped  $\text{YBa}_2\text{Cu}_3\text{O}_{7-\delta}$  samples and the NiO reference sample.

	1 <sup>st</sup> peak	2 <sup>nd</sup> peak	3 <sup>rd</sup> peak	4 <sup>th</sup> peak	5 <sup>th</sup> peak
	distance (Å)	distance (Å)	distance (Å)	distance (Å)	distance (Å)
	(height)	(height)	(height)	(height)	(height)
0.1% Ni	1.36 (0.137)	2.36 (0.052)	2.97 (0.017)	3.80 (0.033)	4.44 (0.027)
0.2% Ni	1.20 (0.097)	2.56 (0.048)	3.14 (0.012)	3.78 (0.036)	4.42 (0.005)
0.3% Ni	1.33 (0.095)	2.60 (0.046)	3.14 (0.011)	3.78 (0.036)	4.43 (0.018)
NiO reference	1.55 (0.088)	2.57 (0.208)	---	---	4.42 (0.090)



impurity. The Fourier transforms for the three experimental samples have been superimposed on the same plot in order to see how they relate to one another as shown in Fig. 4-23. Even though the table only shows three peaks for the reference sample, it should be noted that the third peak at 4.42 Å is a very broad peak, which suggests that there is likely another peak very close to this distance at approximately 4 Å.

An analysis of the transforms is unfortunately somewhat inconclusive. The broad peak at around 4 Å in the NiO reference transform would suggest that NiO is present in the Ni-doped  $\text{YBa}_2\text{Cu}_3\text{O}_{7-\delta}$  samples at approximately 4.42 Å. This is also backed up by the results in Table 6, due to the close relationship between the distances in the fifth column. However, this is still somewhat uncertain, since it is very difficult to make accurate judgments on nearest-neighborhood atomic shells past the third shell. The first atomic shell in all three samples is at a distance from 1.2 to 1.6 Å. Due to the non-order or lack of any trend in the graphs of our three samples, it is somewhat apparent that once Ni is substituted into the  $\text{YBa}_2\text{Cu}_3\text{O}_{7-\delta}$ , adding even more Ni will not change the structure of the  $\text{YBa}_2\text{Cu}_3\text{O}_{7-\delta}$  in any real way. The 1.95 Å value falls outside of the FWHM standard deviation from the distance peaks. To better match this value, several different  $\mu_0(E)$ -fits were attempted using varying parameters, but with little success. Even though the EXAFS results do allow us to conclude that some Ni is incorporated into the crystal structure of the superconductor, the amount of Ni occupying lattice sites is apparently too low for us to determine any site preferences utilizing only the EXAFS results with these noise levels.

## 5. Conclusions

We have reported the observation of the optically active phonon modes in a pure YBCO and in low Ni-doped YBCO. The Cu-O chain vibrations in pure Y-123 cannot be observed by Raman scattering techniques due to odd parity. A chain mode does appear, however, in our doped samples, with a few Ni atoms replacing Cu atoms on the chains and destroying the symmetry that normally precludes their observation in pure YBCO. It can be concluded from our results that at very low-level concentrations of Ni-doping, the Ni is substituting into the Cu(1) chain sites. This substitution is most likely responsible for the enhancement in the in-field  $J_c$ , due to ferromagnetic ordering in the Cu-O chains with the Ni doping. Therefore, the relatively enhanced chain mode peak for  $x = 0.0032$  is caused by nickel substitution, and the optimal enhancement of the in-field  $J_c$  for  $x = 0.0032$  comes from this nickel substitution as well. However, as the amount of doped Ni increases, the nickel starts appearing at the grain boundaries as unreacted NiO, and the deteriorating effect of the NiO impurities on the critical current density overcomes the enhancing effect of the Ni in the Cu chain sites. This conclusion also sufficiently explains the degradation of the superconductivity for values of  $x$  greater than 0.0032, especially for  $x = 0.033$ . This conclusion is borne out by our observation of the Raman vibrational mode attributed to NiO at  $177 \text{ cm}^{-1}$ , as well as its growth in intensity with increasing dopant level.

The results of the EXAFS data collected from our samples were shown alongside a Fourier transform of raw data from an EXAFS experiment on NiO by Jose A. Rodriguez,<sup>59</sup> who was using the same method of analysis as used for our Ni-doped samples. From Fig. 4-23, it was clear that the Ni appeared as an unreacted impurity in the

form of NiO in the  $\text{YBa}_2(\text{Cu}_{1-x}\text{Ni}_x)_3\text{O}_{7-\delta}$  samples. The Ni-doped samples all share a peak at about 2.5 Å on their EXAFS Fourier transform graph, which is, by comparison, clearly a NiO peak. This peak corresponds to the peak at 2.6 Å in the Fourier transform graph of the NiO sample. The non-order of the graphs indicates that once Ni is doped into the YBCO, adding more Ni will not change the local atomic structure of the  $\text{YBa}_2(\text{Cu}_{1-x}\text{Ni}_x)_3\text{O}_{7-\delta}$ , but will only result in the formation of more impurity phases, which agrees with the results by Bridges et al.<sup>60</sup> Although it proved impossible to corroborate peak distances with Bridges et al., it should be noted in this connection that there was a large amount of noise in our EXAFS experimental results due to the extremely low-level Ni concentrations. The Ni-edge is at 8.333 keV, while the Cu-edge is at 8.979 keV, which made it impossible to fully measure the EXAFS normal spectral range, since oscillations from the Cu atoms would dominate over the Ni in the more extended energy range usually scanned in such experiments.

Thus, the results from both EXAFS and Raman spectroscopies are in agreement in terms of their explanation of low-level in-field  $J_c$  enhancement in YBCO due to Ni doping. However, further studies in these areas will have to be done to determine the extent to which other ferromagnetic elements would produce similar enhancement effect in the in-field  $J_c$ . Additionally, more theoretical calculations will be necessary to determine the extent of the role that ferromagnetic ordering can play in such an enhancement of  $J_c$  in the presence of both weak and strong externally applied magnetic fields.

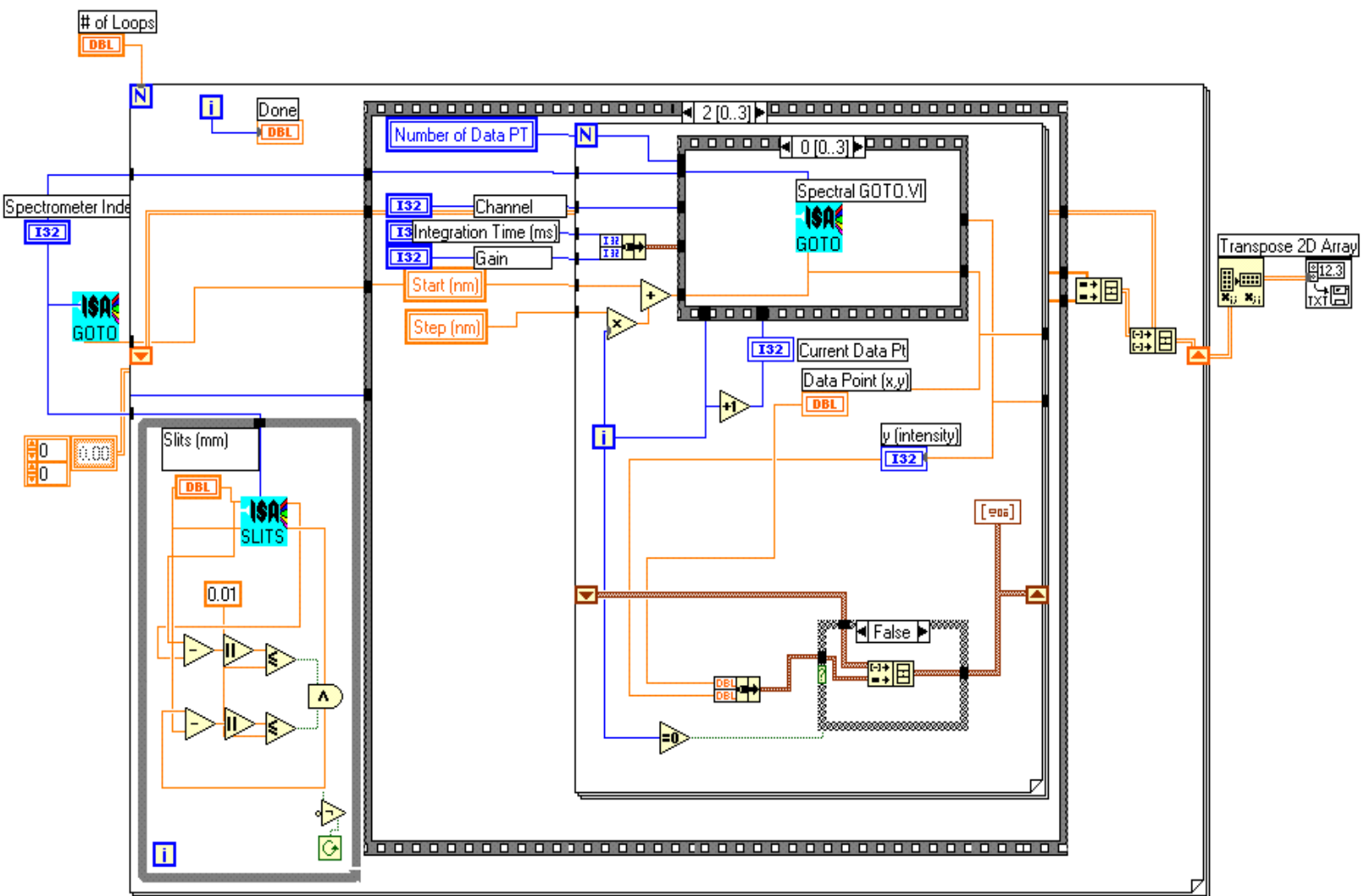
## References

1. S. L. Cooper, D. Reznik, A. Kotz, M. A. Karlow, R. Liu, M. V. Klein, W. C. Lee, J. Giapintkis, D. M. Ginsberg, B. W. Veal, and A. P. Paulikas, Phys. Rev. B **47**, 8233 (1993).
2. H. Kamerlingh Onnes, Leiden Comm. **120b. 122b. 124c** (1911).
3. "High Temperature Superconductivity", edited by Jeffrey W. Lynn, pp 4-6.
4. H. Frohlich, Proc. Royal. Soc. A **223**, 296 (1954).
5. E. Maxwell and C. E. Chase, Physica **24**, 5139 (1958).
6. M. K. Wu, J. R. Ashburn, C. J. Torng, P. H. Hor, R. L. Meng, L. Gao, Z. J. Huang, Y. Q. Wang, and C. W. Chu, Phys. Rev. Lett. **58**, 908–910 (1987).
7. "Introduction to Superconductivity"- 2<sup>nd</sup> Edition, Edited by Michale Tinkham, McGraw-Hill, Inc, pp. 44-46 (1996).
8. "Copper Oxide Superconductors" – Edited by Charles P. Pooles, Jr., Timir Datta, and Horacio A. Farach (A Wiley Interscience Publication), pp. 47.
9. "High Temperature Superconductivity" - Edited by Jeffrey W. Lynn, pp.6-8, (1990).
10. "Raman Spectroscopy for Catalysis", edited by John M. Stencel, pp 6-7 (1990).
11. "Raman Spectroscopy for Catalysis", edited by John M. Stencel, pp. 5-7 (1990).
12. "Quantum Physics of Atoms, Molecules, Solids, Nuclei, and Particles"- 2<sup>nd</sup> Edition, Robert Eisberg, and Robert Resnick, pp.484-487 (1985).
13. "Introduction to Superconductivity" – 2<sup>nd</sup> Edition, Michale Tinkham, McGraw-Hill, Inc., pp. 3-4.
14. "Introduction to Superconductivity" – Vol. **6**, A. C. Rose-Innes and E. H. Rhoderick, pp. 42 (1969).
15. "Introduction to Superconductivity" – Vol. **6**, A. C. Rose-Innes and E. H. Rhoderick, pp. 182-183 (1969).
16. "Copper Oxide Superconductors", Charles P. Poole Jr., Timir Datta, and Horacio A. Farach, (A Wiley Interscience Publication), pp 199-203.

17. Y. Yacoby, E. A. Stern. in “X-ray and inner-shell process: 17th international conference”, ed. R. L. Johnson, H. Schmidt-Böcking, B. F. Sonntag. 535-555 (1996).
18. B. K. Teo, in “Inorganic Chemistry Concepts”, **9**, ed. C. K. Jørgensen, M. F. Lippert, S. J. Lippard, J. L. Margrave, K. Niedenzu, H. Nöth, R. W. Parry, H. Yamatera. (1986).
19. E. A. Stern, in “X-Ray Absorption: Principles, Applications, Techniques of EXAFS, SEXAFS, and XANES”, ed. D. C. Koningsberger and R. Prins, *Chemical Analysis*, **92**, ed. J. D. Winefordner, and I. M. Kolthoff. 3-51 (1988).
20. See Ref. 17.
21. See Ref. 19.
22. See Ref. 18.
23. D. E. Sayers, E. A. Stern, and F. W. Lytle, *Phys. Rev. Lett.* **27**, 1204 (1971).
24. See Ref. 19.
25. See Ref. 19.
26. See Ref. 17.
27. See Ref. 17.
28. C. Thomsen, in “Light Scattering in High-Tc Superconductors”, edited by M. Cardona and G. Guntherodt, Vol. **68** of Topics in Applied Physics (Springer, Berlin, 1991), pp. 285-359.
29. M. Limonov, D. Shantsev, and S. Tajima, *Phys. Rev. B* **65**, 024515 (2001).
30. C. C. Homes, D. A. Bonn, Ruixing Liang, and W. N. Hardy, *Phys. Rev. B* **60**, 9782 (1999).
31. J. Essick, “Advanced LabView Labs”, Prentice-Hall (1999).
32. F. Bridges, J. B. Boyce, T. Claeson, T. H. Geballe, and J. M. Tarascon, *Phys. Rev. B* **42**, 2137 (1990).
33. Lei Wang and Shirshak K Dhali, *Supercond. Sci. Technol.* **6**, 199-202 (1993).

34. "Magnetic Field Dependence of the Transport Critical Current Density in the Superconductor Family  $\text{ReBa}_2\text{Cu}_3\text{O}_{7-x}$ ", a Thesis by Christopher M. Martin, Physics Department, Physical Sciences Library, WIU, pp.113-130 (1997).
35. T. Ressler. WinXASv2 tutorial (1998).
36. See Ref. 18.
37. D. N. Basov, A. V. Puchkov, R. A. Hughes, T. Strach, T. Preston, T. Timusk, D. A. Bonn, R. Liang, and W. N. Hardy, *Phys. Rev. B* **49**, 12165(1994).
38. S. A. Hoffman, M. A. Castro, G. C. Follis, and S. M. Durbin, *Phys. Rev. B* **49**, 12170 (1994).
39. R. S. Howland, T. H. Geballe, S. S. Laderman, A. Fischer-Colbrie, M. Scott, J. M. Tarascon, and P. Barboux, *Phys. Rev. B* **39**, 9017(1989).
40. R. Liu, C. Thomsen, W. Kress, M. Cardona, B. Gegenheimer, F. W. de Wette, J. Parade, A. D. Kulkarni, and U. Schroder, *Phys. Rev. B* **37**, 7971 (1988).
41. Altendorf, J. Chrzanowski, and J. C. Irwin, *Phys. Rev. B* **43**, 2771 (1991).
42. See Ref. 40.
43. See Ref. 40.
44. E. T. Heyen, R. Liu, C. Thomsen, R. Kremer, and M. Cardona, *Phys. Rev. B* **41**, 11058 (1990).
45. J. D. Jorgensen, B. W. Veal, W. K. Kwok, G. W. Crabtree, A. Umezawa, L. J. Nowicki, and A. P. Paulikas. *Phys. Rev. B.* **36**, 5731 (1987).
46. See Ref. 39.
47. See Ref. 39.
48. D. M. Krol, M. Stravola, W. Weber, L. F. Schneemayer, J. V. Waszczak, S. M. Zahurak, and S. G. Konsinski, *Phys. Rev. B* **36**, 8325 (1987).
49. D. Krillov, J. P. Collman, J. T. McDevitt, G. T. Yee, M. J. Holcomb, and J. Bozovic, *Phys. Rev. B* **37**, 3660 (1988).
50. C. C. Homes, D. A. Bonn, R. Liang, W. N. Hardy, D. N. Basov, T. Timusk, and B. P. Clayman, *Phys. Rev. B* **60**, 9782 (1999).
51. See Ref. 49.

52. R. E. Cohen, W. E. Pickett, and H. Krakauer, Phys. Rev. Lett. **64**, 25751 (1990).
53. W. Kress, U. Schroder, J. Prade, A. D. Kulkarni, and F. W. de Wette, Phys. Rev. B **38**, 2906(1988).
54. Couach M. and Khoder A. F, in "Magnetic Susceptibility of Superconductors and other Spin Systems", ed. R. A. Hein, T. L. Francavilla, and D. H. Liebenberg, Plenum, New York pp. 35 (1992).
55. F. Bridges, J. B. Boyce, T. Claeson, T. H. Geballe, and J. M. Tarascon, Phys. Rev. B **42**, 2137 (1990).
56. B. Jayaram, S. K. Agarwal, C. V. Rao, and A. V. Narlikar, Phys. Rev. B **38**, 2903 (1988).
57. "Copper Oxide Superconductors", Charles P. Poole, Jr., Timir Datta, and Horacio A. Farach, pp.197-199.
58. See Ref. 54.
59. Jose A. Rodriguez, Jonathan C. Hanson, Anatoly I. Frenkel, Jae Y. Kim, and Manuel Perez, J. AM. CHEM. SOC. 9 VOL. **124**, NO. 2 (2002).
60. See Ref. 31.



Appendix A. A Diagram of LabView Program for Raman Scattering Measurement.